GENERATION OF

AURORAL KILOMETRIC AND Z-MODE RADIATION

BY THE CYCLOTRON MASER INSTABILITY

by

Nojan Omidi

An Abstract

Of a thesis submitted in partial fulfillment
of the requirements for the Doctor of
Philosophy degree in Physics
in the Graduate College of
The University of Iowa

May 1984

Thesis supervisor: Professor Donald A. Gurnett

ABSTRACT

Generation of auroral kilometric and Z-mode radiation by the cyclotron maser mechanism is studied. This study entails investigation of the relativistic Doppler shifted cyclotron resonance condition and the growth of electromagnetic waves by the cyclotron maser mechanism. It is shown that the cyclotron resonance condition defines an ellipse in velocity space when the product of the index of refraction and cosine of the wave normal angle is less than or equal to one and a partial ellipse when the above product is larger than one. It is also shown that waves with frequencies greater than the gyrofrequency (or its harmonic for higher harmonic resonances) can only resonate with particles moving in the same direction along the magnetic field, while waves with frequencies less than the gyrofrequency (or its harmonic), resonate with particles moving in both directions along the magnetic field.

The relativistic resonance condition and the electron distribution function in velocity space obtained by the S3-3 satellite are used to numerically calculate growth rates for both the auroral kilometric and Z-mode radiation. The results show that this electron distribution is unstable and provides positive growth rates for both the aforementioned emissions. In the case of auroral kilometric radiation (AKR), the upgoing electrons with a loss cone distribution are the primary source

of free energy, while in the case of Z-mode radiation both the upgoing and the downgoing electrons contribute to the growth of these waves. Assuming no refraction for the Z-mode waves, the path lengths required to account for the observed intensities of these emissions are calculated and the results show that this radiation can be sufficiently amplified within reasonable distances. In order to compute path integrated growths of auroral kilometric radiation, Poeverlein's graphical method is used to perform a three-dimensional ray tracing for these waves. By computing path integrated growths of six representaitive rays, it is demonstrated that electron distribution functions like those measured by the S3-3 satellite are not capable of amplifying cosmic noise background to the observed intensities of auroral kilometric radiation, and that much steeper slopes at the edges of the loss cone are required to do so. The presence of such distribution functions in the auroral zone is plausible if one assumes that backscattered electrons in this region have energies less than a few hundred eVs.

Abstract approved: Darell A. Hamlett
Thesis supervisor

Professor, Physics and Astronomy
Title and Department

Jan 27, 1984
Date

GENERATION OF

AURORAL KILOMETRIC AND Z-MODE RADIATION

BY THE CYCLOTRON MASER INSTABILITY

by

Nojan Omidi

A thesis submitted in partial fulfillment
of the requirements for the Doctor of
Philosophy degree in Physics
in the Graduate College of
The University of Iowa

May 1984

Thesis supervisor: Professor Donald A. Gurnett

Graduate College
The University of Iowa
Iowa City, Iowa

CERTIFICATE OF APPROVAL

PH.D. THESIS

This is to certify that the Ph.D. thesis of

Nojan Omidi

has been approved by the Examining Committee for the thesis requirement for the Doctor of Philosophy degree in Physics at the May 1984 graduation.

Thesis committee: D. A. Gurnett
Thesis supervisor

F. A. Frank
Member

J. A. Van Allen
Member

Christopher K. Goertz
Member

Member

ACKNOWLEDGEMENTS

Since my thanks and gratitudes go to so many people that listing their names would not be feasible, I am forced to mention only a few people to whom I am particularly indebted. Among them is Professor D. A. Gurnett for whom I have great respect and admiration. His supervision along with his financial support are the cornerstones of this project. I wish to thank him for his constructive criticisms, many helpful suggestions, and classroom as well as office lectures, all of which have been invaluable learning experiences for me. His encouragement and support for expansion of ideas have been instrumental in my progress and are greatly appreciated. I would also like to thank Professor C. S. Wu for many helpful comments and suggestions on this study and also for inviting me to the University of Maryland. It has indeed been a pleasure as well as a fruitful experience to do collaborative work with him. My special thanks go to Professor C. K. Goertz who has from the beginning shown his interest in this project by encouragement and critical evaluation of my work along with many useful suggestions and comments all of which are greatly appreciated. I am also indebted to him for his numerous and excellent lectures on various topics in the solar terrestrial physics course which have been a joy to attend and extremely beneficial. Throughout the past few years I have enjoyed having many valuable discussions with Dr. W. Calvert. I thank

him for his input in this project and sharing his ideas with me. His constant encouragements are also appreciated. To Dr. R. R. Anderson go my sincerest thanks; his hiring me as a data technician five years ago was instrumental in preparing me for things to come. My deepest gratitudes go to Ms. K. Goodner whom I believe should be named the secretary of the year. Her efficient and unerring typing of this manuscript along with other papers are greatly appreciated. I also wish to thank and admire her patience in view of so many changes and revisions. John Birkbeck and Jeana Wonderlich's professional work on drawing the figures in the manuscript are very much appreciated. I also thank all the people in the computer room who have been a great help in running my programs. Last, but not least, I wish to thank all the faculty, staff and students who have made the past few years instructive and enjoyable ones. I am honored to have been associated with so many top ranked scientists and professionals, and to graduate from a department that is so well known for its pioneering and excellent work. To show my thanks and unending love for my family, I dedicate this work to them.

This research was supported by the National Aeronautics and Space Administration through grant NGL-16-001-043 and by the Office of Naval Research through grant N00014-76-C-0016.

ABSTRACT

Generation of auroral kilometric and Z-mode radiation by the cyclotron maser mechanism is studied. This study entails investigation of the relativistic Doppler shifted cyclotron resonance condition and the growth of electromagnetic waves by the cyclotron maser mechanism. It is shown that the cyclotron resonance condition defines an ellipse in velocity space when the product of the index of refraction and cosine of the wave normal angle is less than or equal to one and a partial ellipse when the above product is larger than one. It is also shown that waves with frequencies greater than the gyrofrequency (or its harmonic for higher harmonic resonances) can only resonate with particles moving in the same direction along the magnetic field, while waves with frequencies less than the gyrofrequency (or its harmonic), resonate with particles moving in both directions along the magnetic field.

The relativistic resonance condition and the electron distribution function in velocity space obtained by the S3-3 satellite are used to numerically calculate growth rates for both the auroral kilometric and Z-mode radiation. The results show that this electron distribution is unstable and provides positive growth rates for both the aforementioned emissions. In the case of auroral kilometric radiation (AKR), the upgoing electrons with a loss cone distribution are the primary source

of free energy, while in the case of Z-mode radiation both the upgoing and the downgoing electrons contribute to the growth of these waves. Assuming no refraction for the Z-mode waves, the path lengths required to account for the observed intensities of these emissions are calculated and the results show that this radiation can be sufficiently amplified within reasonable distances. In order to compute path integrated growths of auroral kilometric radiation, Poeverlein's graphical method is used to perform a three-dimensional ray tracing for these waves. By computing path integrated growths of six representaitive rays, it is demonstrated that electron distribution functions like those measured by the S3-3 satellite are not capable of amplifying cosmic noise background to the observed intensities of auroral kilometric radiation, and that much steeper slopes at the edges of the loss cone are required to do so. The presence of such distribution functions in the auroral zone is plausible if one assumes that backscattered electrons in this region have energies less than a few hundred eVs.

TABLE OF CONTENTS

LIST OF TABLES

LIST OF FIGURES

I. INTRODUCTION

Auroral kilometric and broadband Z-mode radiation are two of the principal types of electromagnetic waves observed in the auroral region (Figure 1). Auroral kilometric radiation or AKR is one of the most intense radio emissions from the Earth's magnetosphere. This radiation has been extensively studied in the past several years. It is now well known that AKR is generated in the high latitude auroral regions at radial distances between 1.5 to 3 R_E in association with discrete auroras and inverted-V electron precipitation regions [Gurnett, 1974; Kaiser and Stone, 1975; Kurth et al., 1975; Green et al., 1979; Benson and Calvert, 1979; Gallagher and Gurnett, 1979]. The most intense and dominant component of this radiation is generated in the right-hand polarized extraordinary (R-X) mode, although left-hand polarized radiation has also been observed [Gurnett and Green, 1978; Kaiser et al., 1978; Benson and Calvert, 1979; Shawhan and Gurnett, 1982]. Observations with the ISIS-1 topside sounder satellite [Benson and Calvert, 1979] and the Hawkeye satellite [Calvert, 1981] have revealed the presence of a large plasma cavity in the auroral region. These observations indicate that the kilometric radiation is generated in a region where the ratio of the plasma frequency (f_p) to the electron gyrofrequency (f_g) is much less than one.

Unlike AKR, which has been extensively studied for several years, little is known about the broadband Z-mode radiation which is found in the low density plasma over the high latitude auroral and polar regions [Calvert, 1981; Gurnett et al., 1983]. Due to lack of adequate direction finding observations the source region has not been exactly located, although it is likely that it is generated in the auroral region. Recent measurements with the DE-1 spacecraft have shown that Z-mode radiation is not observed between f_g and the upper hybrid resonance frequency (f_{UHR}) and that it is most intense right below the gyrofrequency. Observations have also indicated that this radiation propagates nearly perpendicular to the geomagnetic field $\vec{B}$ [Gurnett et al., 1983].

As far as generation mechanisms for these two radiations are concerned, more work has been done on AKR than on Z-mode radiation. Among the many theories proposed for the generation of AKR, the one suggested by Wu and Lee [1979] has been most consistent with the particle and wave observations in the auroral zone. In this theory it is suggested that mildly relativistic electrons with a loss cone distribution can amplify right-hand polarized extraordinary waves via the cyclotron maser mechanism. Recently, in a number of papers [Lee and Wu, 1980; Omidi and Gurnett, 1982; Wu et al., 1982; Melrose et al., 1982; Dusenbery and Lyons, 1982; Hewitt et al., 1982; Hewitt and Melrose, 1982; LeQueau et al., 1983; Omidi et al., 1984; Melrose et al., 1983; LeQueau et al., 1983; Omidi and Gurnett, 1984] the cyclotron maser instability has been extensively studied and its applicability to the generation of

AKR has been tested. The results of these studies have shown that electron distribution functions with loss cones are unstable and give rise to the growth of R-X mode waves with frequencies (f) near the electron cyclotron frequency and at large wave normal angles (θ). In most of these studies, model electron distribution functions were used to calculate growth and damping rates. Omidi and Gurnett [1982] and Omidi et al. [1984] used a representative electron pitch angle distribution measured by the S3-3 satellite in the auroral region to compute growth and damping rates. These calculations demonstrated that auroral electron distribution functions are unstable. However, computations of the path integrated growth of AKR have shown that these distributions are not capable of providing sufficient amplification for the kilometric radiation and that much steeper slopes at the edges of the loss cone are required to allow sufficient growth of these waves [Omidi and Gurnett, 1984].

As was mentioned earlier, compared to AKR, much less work has been done on the generation of Z-mode radiation. Among the theories proposed for the generation of Z-mode emission, all but one suggest that these waves are generated between f_g and f_{UHR}. For example, Taylor and Shawhan [1974] suggested incoherent Cerenkov radiation as a generation mechanism while Kaufman et al. [1978] and Maggs and Lotko [1981] have proposed that coherent plasma instabilities due to auroral electron beams are responsible for the generation of Z-mode radiation. Recently, Omidi et al. [1984] and Hewitt et al. [1983] proposed the cyclotron maser instability as a generation mechanism for Z-mode

emissions. Omidi et al. [1984] suggested that Z-mode waves with frequencies below the gyrofrequency can be amplified via resonance with electrons with free energy moving in both directions along the magnetic field. Hewitt et al. [1983] on the other hand suggested that amplification occurs for waves with frequencies between f_g and f_{UHR} through resonance with the upgoing electrons in the loss cone. One objection to this mechanism, however is that Z-mode emissions are not observed above the electron gyrofrequency.

In the present work an attempt is made to present a detailed study of the cyclotron maser mechanism and its application to the generation of auroral kilometric and Z-mode radiation. In Chapter II, the relativistic Doppler-shifted cyclotron resonance condition is extensively studied, and its general properties are reviewed. It is shown that this resonance condition defines an ellipse in velocity space when the product of the index of refraction (N) and cosine of the wave normal angle is less than or equal to one and a partial ellipse when the product is larger than one. Characteristics of the resonance ellipse in the case of resonance with the free space R-X mode and Z-mode radiation are also presented.

In Chapter III, the growth rates of both the upgoing and downgoing AKR are presented. It is shown that the upgoing waves are more likely to be amplified. Using Poeverlein's graphical method, a three-dimensional ray tracing for the kilometric radiation is performed in Chapter IV. The ray paths obtained in this chapter are used to compute the path integrated growths of AKR in Chapter V. Since the S3-3

electron distribution function is not capable of sufficiently amplifying the waves, model distribution functions are used to find the minimum slopes $(\frac{\partial F}{\partial v_\perp})$ required to account for the observed intensities of AKR. In Chapter IV, generation of the Z-mode radiation by the cyclotron maser instability is considered. It is shown that the S3-3 electron distribution function can sufficiently amplify this radiation. In Chapter VII, summary and conclusions of this study are presented. Finally in the appendix, the expressions used in calculating the imaginary part of the frequency (ω_i) are given, and a simple approximate equation for (ω_i) similar to that given in Wu and Lee [1979] but in a more accurate form is derived.

Before concluding this chapter, a few remarks on the notations used in this manuscript are in order. The first item of notation is that throughout this work both frequency and angular frequency are used. For example, both f_g and $\omega_g = 2\pi f_g$ are used interchangeably throughout the manuscript. The justification for using these two types of frequencies is that frequencies are usually used when dealing with observations and angular frequencies are usually used when dealing with theory. The second item of notation is that in the present study it has been assumed that two separate electron populations exist in the auroral region. The first population consisting of cold electrons with a plasma frequency f_{pc} (or just f_p for simplicity) and the second population consisting of more tenuous hot electrons with a plasma

frequency f_{pH}. The cold electrons are presumed to control the real part of the dispersion relation while the warm electrons are presumed to cause the wave amplification. This assumption seems to be appropriate as long as $f_{pc} \gtrsim f_{pH}$ [Wu et al., 1982].

II. RELATIVISTIC DOPPLER-SHIFTED CYCLOTRON RESONANCE

It is well known [Baldwin et al., 1969] that in order for a wave with angular frequency ω and wave normal angle θ to resonate relativistically with electrons with angular gyrofrequency ω_g and velocity $v_\parallel$ along a magnetic field line, the following condition must be satisfied:

$$\omega - k\, v_\parallel \cos\theta = \frac{n\,\omega_g}{\gamma} \tag{1a}$$

where the integer n indicates various harmonics of ω_g, k is the wave number, $\gamma \equiv (1 - v^2/c^2)^{-1/2}$, v is electron velocity, and c is the speed of light. Substituting $N\omega/c$ for k, where N is the index of refraction and dividing both sides of Equation (1a) by ω one obtains:

$$1 - N \cos\theta \frac{v_\parallel}{c} = Y \sqrt{1 - v^2/c^2} \tag{1b}$$

where $Y \equiv \frac{n\,\omega_g}{\omega}$. Squaring both sides of Equation (1) results in an equation for an ellipse. This ellipse has a center at $V_C = B/A$, semi-minor axis $V_R = D/A$, and semi-major axis $V_S = D/Y$, (Figure 2a) where

$$A = (Y^2 + N^2 \mathrm{Cos}^2\theta)^{1/2} \tag{2a}$$

$$B = \frac{cN \ \mathrm{Cos}\ \theta}{A} \tag{2b}$$

and

$$D^2 = c^2(Y^2 - 1) + B^2 \quad . \tag{2c}$$

Rather than analyzing the resonance condition for each specific mode of propagation, one can study how the parameters Y and $N_\parallel \equiv N \ \mathrm{Cos}\ \theta$ can affect the size and position of the resonance ellipse. Once this is done, it will be a matter of knowing the values of Y and $N_\parallel$ in a specific mode, and an overall view of the resonance condition will be at hand. Note that Y and $N_\parallel$ completely determine the shape and position of the resonance ellipse.

As can be seen in Figure 2, the semi-minor axis of the resonance ellipse lies on the $v_\parallel$ axis. From the definitions of V_C and V_R it is clear that if $B > D$ then the resonance ellipse lies entirely in the region $v_\parallel > 0$, i.e., all parallel resonance velocities will be positive (Figures 2a,d). Note that positive $v_\parallel$ corresponds to a direction along the magnetic field $\vec{B}$ for which $k_\parallel \equiv k \ \mathrm{Cos}\ \theta$ has a positive value, i.e., it is the wave vector $\vec{k}$ that determines which side of the distribution corresponds to positive $v_\parallel$. Similarly, for $B = D$ the ellipse will go

through the origin (Figures 2b,e) and for $B < D$ the resonance ellipse encircles the origin (Figures 2c,f). From Equation (2c) it is evident that $D > B$ if $Y > 1$, and $D < B$ if $Y < 1$, which means that for $Y < 1$ only particles with positive $v_\parallel$ can resonate with waves, whereas for $Y > 1$ particles with both positive and negative parallel velocities resonate with waves [Omidi et al., 1984]. Note that this result can only be obtained if the relativistic resonance condition is used, i.e., if γ is set equal to one for low energy electrons in Equation (1), then depending upon the value of Y, only particles with $v_\parallel > 0$ or $v_\parallel < 0$, but not both can resonate with the waves.

In order to study the role of $N_\parallel$ it should be noted that since the equation of the resonance ellipse is obtained by squaring both sides of Equation (1), it is possible that this equation may have false roots. Since the right-hand side of Equation (1b) is always positive, the left-hand side must also be positive and any $v_\parallel$ for which the left-hand side is negative is a false root. Clearly for $N_\parallel < 1$ all parallel velocities corresponding to the resonance ellipse are acceptable roots because the term $N_\parallel v_\parallel/c$ is always less than one and therefore the left-hand side of Equation (1b) is always positive (Figures 2a,b,c). On the other hand, for $N_\parallel > 1$ the left-hand side of Equation (1b) is negative for all $v_\parallel$ that satisfy the following condition

$$v_\parallel > \frac{c}{N_\parallel} \quad . \tag{3}$$

This can be seen by noting that $v_{\parallel o} = c/N_{\parallel}$ sets the left-hand side of Equation (1b) equal to zero. It can easily be shown that the straight line $v_{\parallel} = c/N_{\parallel}$ always intersects the resonance ellipse at the perpendicular velocities

$$v_{\perp o} = \pm c(1 - \frac{1}{N_{\parallel}^2})^{1/2} \tag{4}$$

which correspond to $v_o = (v_{\parallel o}^2 + v_{\perp o}^2)^{1/2} = c$. From Equation (3) it is evident that the portion of the resonance ellipse that falls to the right of the straight line $v_{\parallel} = c/N_{\parallel}$, corresponds to false roots, i.e., particles laying on this portion of the ellipse are not in resonance with waves. The non-resonance portion of the ellipse is shown in Figures 2d,f by broken lines.

As will be demonstrated in Section A, for small $N_{\parallel}$, the resonance ellipse does not approach the straight line $v_{\parallel} = c(1 - Y)/N_{\parallel}$ given by the nonrelativistic resonance condition

$$\omega - k_{\parallel} v_{\parallel} = n\ \omega_g \quad , \tag{5}$$

even when the resonance velocity is small. In this context, the term nonrelativistic may not be entirely appropriate because it is not just the velocity of the resonating electrons that determines whether Equation (1) or (5) should be used, but also the value of $N_{\parallel}$. By taking

the limit of large $N_\parallel$ it can be shown that the resonance line (resonating portion of the ellipse) given by equation (1) approaches that of Equation (5). This can be seen by noting that as $N_\parallel$ gets larger the ellipse given by Equation (1) becomes more eccentric, $v_{\parallel o}$ gets smaller and $v_{\perp o}$ approaches c. Note also that as $N_\parallel \to \infty$, the center of ellipse V_c and the semi-minor axis V_R both approach zero and the semi-major axis V_s approaches the speed of light.

In summary, it has been shown that when the wave frequency is below the gyrofrequency (or its harmonic), both electrons with positive and negative $v_\parallel$ resonate with waves, and as we shall see in Chapter VI this is of great importance in the generation of the broadband Z-mode radiation. It has also been demonstrated that when $N_\parallel > 1$, particles with $v_\parallel > c/N_\parallel$ are not in resonance with waves, and as $N_\parallel$ gets larger the difference between the relativistic and the nonrelativistic resonance condition becomes less noticeable.

A. Resonance With the Free Space R-X Mode at n = 1

To better understand the characteristics of the resonance ellipse, Figure 3 is provided. This figure shows V_C/c and V_R/c plotted as a function of the normalized parameter $\Delta\omega/\omega_g$ ($\Delta\omega \equiv \omega - \omega_g$) for two ω_p/ω_g ratios and a number of wave normal angles. As can be seen, the allowed resonance conditions are bounded by the "D = 0 boundary" which we shall now discuss. Since the semi-major and semi-minor axes are given by D/Y and D/A, respectively, it is clear that when D, given by Equation 2c, goes to zero the resonance ellipse shrinks to a point and disappears.

Setting D = 0 in Equation 2c and also recalling that $V_C = B/A$, we get two equations, and by eliminating the (N cos θ) term between them we find:

$$\frac{V_C}{c} = \frac{\sqrt{\frac{\Delta\omega}{\omega_g}\left(\frac{\Delta\omega}{\omega_g} + 2\right)}}{\frac{\Delta\omega}{\omega_g} + 1} \tag{6}$$

which is the equation for the D = 0 boundary. Note that the D = 0 boundary is only a function of the ratio $\Delta\omega/\omega_g$ and is completely independent of ω_p.

The low frequency limit to cyclotron resonance occurs near the extraordinary mode cutoff, $\omega_{R=0} = \omega_g/2 + \sqrt{(\omega_g/2)^2 + \omega_p^2}$. As this cutoff is approached from higher frequencies the index of refraction goes to zero, as illustrated in Figure 4. Near the cutoff the resonance ellipse degenerates to a circle, this time with both the radius and center shrinking to zero as ω approaches $\omega_{R=0}$. Note, however, that V_C never reaches zero because the D=0 boundary is encountered before ω reaches $\omega_{R=0}$.

The bottom two panels of Figure 3 demonstrate the behavior of the semi-minor axis, V_R, which is equivalent to the radius of the resonance circle for low velocities. Note that for any given θ, V_R goes to zero for values of $\Delta\omega/\omega_g$ for which the V_C curve intersects the D = 0 boundary. Each V_C curve intersects the D=0 boundary twice. Thus, there are

two values of $\Delta\omega/\omega_g$ for which $V_R = 0$, marking the upper and lower bounds of the cyclotron resonance interaction region.

Panels a and c in Figure 3 indicate that as ω approaches $\omega_{R=0}$, V_C/c and V_R/c both approach zero and the velocity of resonanting electrons becomes very small. Thus, one might think that for ω close to $\omega_{R=0}$ a nonrelativistic resonance condition might suffice. However, this conjecture is not true (as was demonstrated in the last section in a different way) for the following reason. As it is shown in Figure 4, the index of refraction goes to zero at $\omega_{R=0}$, i.e., $N_\parallel$ is zero. Using the nonrelativistic resonance condition,

$$\omega - N_\parallel \omega \frac{v_\parallel}{c} = \omega_g \tag{5}$$

it is evident that the resonance velocity goes to infinity as ω approaches $\omega_{R=0}$, which is in contradiction with the relativistic results. This contradiction can be resolved in the following manner. From Equation 1 with $v_\perp = 0$ and the approximation $\gamma^{-1} \approx (1 - v^2/2c^2)$, the low velocity root for $v_\parallel$ can be written in the relativistic form as

$$\frac{v_\parallel}{c} = \frac{\omega}{\omega_g} N_\parallel - \frac{\omega}{\omega_g} N_\parallel \sqrt{1 - \frac{2(\omega-\omega_g)}{\omega_g}\left(\frac{\omega_g}{\omega}\right)^2 \frac{1}{N_\parallel^2}} \tag{7}$$

If the second term in the square root is assumed to be small, then this equation reduces to the nonrelativistic resonance condition

$$\frac{v_{\parallel}}{c} = \frac{\Delta\omega}{\omega\ N_{\parallel}} \tag{8}$$

whenever

$$\frac{(\omega-\omega_g)}{\omega_g}\ \left(\frac{\omega_g}{\omega}\right)^2 \frac{1}{N_{\parallel}^2} \ll 1 \quad . \tag{9}$$

It is evident, therefore, that the nonrelativistic formula for $v_{\parallel}$ can be obtained from the relativistic formula for $v_{\parallel}$ (Equation 7) if and only if Equation 9 is satisfied. It is clear from Equation 9 that whenever either N or cos θ approach zero, the nonrelativistic formula fails to provide an adequate approximation, even for very low velocities. Recalling that $V_C/c \ll 1$ only when $N_{\parallel} \ll 1$, we conclude that under no limit will the relativistic resonance ellipse approach the nonrelativistic resonance condition, which is a straight line parallel to the $V_{\perp}$ axis.

Another dependence that can be seen from Figure 3 is that as the ω_p/ω_g ratio increases the maximum wave normal angle for which the resonance condition can be satisfied decreases and the minimum V_C increases. Thus, as the ω_p/ω_g ratio decreases the minimum energy of the resonating electrons becomes smaller.

We now illustrate the effect of letting N and Cos θ go to zero on the resonance ellipse. One can see from Equation (2a) that as N Cos θ approaches zero, A approaches Y and D/A goes to D/Y, which means that as either N or Cos θ approach zero the resonance ellipse approaches a circle. Figure 5 summaries all of the results obtained so far. For example, in panels a and c of Figure 5 ω is near $\omega_{R=0}$ and thus $N \ll 1$, which explains why all the resonant curves are close to a circle. In Figure 5 (b and d), however, $N \approx 1$ and thus the resonant curves are circular only for large wave normal angles (Cos $\theta \to 0$) and as θ becomes smaller the resonant curves become more elliptical.

Figure 6 shows the lower left part of CMA diagram in which the free space R-X mode exists. The shaded region shows the values of $X \equiv \omega_p^2/\omega^2$ and $Y \equiv \omega_g/\omega$ for which resonance is possible. This illustration demonstrates how the wave normal angle determines the values of X and Y for which resonance is possible. The dashed boundary is the line on which D = 0 (D = 0 boundary) and its equation in (X, Y) space is obtained from $Y^2 + N^2 \cos^2 \theta = 1$ (see Equation 2c) and substituting for N in terms of X, Y and θ. Figure 6 shows that as the wave normal angle increases a lower plasma frequency is required for resonance to occur and that the wave frequency must be closer to the cutoff frequency $\omega_{R=0}$.

Contours for the minimum energy of the resonating electrons are plotted in the CMA diagram of Figure 7. The line which various contours intersect is the D = 0 boundary. Figure 7 shows that as the wave normal angle increases, only lower energy electrons can resonate with

waves. In other words, in a region with low ω_p and ω near $\omega_{R=0}$, waves only resonate with low energy electrons and as the wave normal angle increases, lower plasma frequencies are required for resonance.

B. Resonance With the Z-Mode Radiation

In contrast with the fast extraordinary mode waves whose index of refraction vary between zero and one, the slow extraordinary (or Z-mode) waves have index of refraction that vary between zero and infinity. According to the cold plasma theory, Z-mode radiation can exist between the L = 0 cutoff ($\omega_{L=0}$) and the upper hybrid resonance (ω_{UHR}) frequencies given by:

$$\omega_{L=0} = \frac{-\omega_g}{2} + \sqrt{\left(\frac{\omega_g}{2}\right)^2 + \omega_p^2} \qquad \text{and}$$

$$\omega_{UHR} = \sqrt{\omega_g^2 + \omega_p^2} \quad . \tag{10}$$

It is obvious that in the case of Z-mode radiation, both Y and $N_\parallel$ can be either smaller or greater than one, depending upon the wave frequency. Hence, it is possible for Z-mode waves to resonate with particles moving in both directions along the magnetic field. It is also possible for certain frequencies and wave normal angles that a portion of the resonance ellipse will not correspond to resonance, and thus care must be taken when growth rates are calculated. Since in the

present work, only generation of Z-mode waves below the electron gyrofrequency is considered, the study of the resonance ellipse is limited to the case when $Y > 1$. In Figure 8, four resonance ellipses for the Z-mode corresponding to $Y = 1.01$, $X = 0.1$, and four different wave normal angles are shown. It can be seen that when $\theta = 80°$ and $N_{\parallel} < 1$, the resonance ellipse is nearly circular (i.e., $A = Y$) and the entire circle corresponds to resonance. For $\theta = 50°$, $N_{\parallel}$ is larger than one. Therefore, a portion of the ellipse (broken line) does not correspond to resonance. As θ gets smaller, $N_{\parallel}$ gets larger, the ellipse becomes more eccentric and a larger portion of it does not correspond to resonance.

In Chapter VI, it is shown that resonance with auroral electrons with free energy will be possible, when $\theta \sim 90°$ and Y is slightly greater than one. In this case the resonance ellipse is nearly circular and its center is near the origin.

III. GROWTH RATES OF AKR

A. An Overview

As was mentioned in the introduction, among the many theories proposed for the generation of AKR, the one suggested by Wu and Lee [1979] has been most consistent with the particle and wave observations in the auroral region. In this theory it is suggested that the free energy of the mirrored inverted-V electrons in the loss cone is used to amplify right-hand extraordinary waves via the cyclotron maser instability. Since the inverted-V electrons have typical energies of about 1-5 keV, from the discussions in Section II.A it is clear that in order for waves to resonate with these electrons the f_p/f_g ratio must be much less than one. Calvert [1981], has reported a low density plasma cavity in the auroral region extending from the geocentric distance of about 1.5 R_E all the way up to 3.5 R_E. In this plasma cavity the f_p/f_g ratio drops to values between 0.03 to 0.2. The presence of the auroral plasma cavity and loss cones in the auroral electron distribution functions combined with the fact that the most intense and dominant component of AKR is in the R-X mode, have made the cyclotron maser instability an attractive mechanism for the generation of AKR. In this chapter the growth and damping rates of both the upgoing and the downgoing AKR are presented.

B. Sources of Free Energy in the Auroral Electron Distribution Functions

Before looking at the growth rates, it is helpful to summarize the separate sources of free energy that are commonly found in the electron distribution functions obtained by the S3-3 satellite in the auroral region. A full discussion of these distributions can be found in Mizera and Fennell [1977], and Croley et al. [1978]. The first of these features is a loss cone region in the upward side of the distribution (Figure 9a) first suggested by Wu and Lee [1979] as the source of free energy in the generation of AKR. The second source of free energy is a "hole-like" feature on the downward side of the distribution. Compared to the loss cone region, the "hole" is limited to smaller pitch angles and also confined to lower energy electrons. This region of the electron distribution has been pointed out by Dusenbery and Lyons [1982] as a possible source of free energy for the generation of the kilometric radiation. Also in a detailed study using model distributions, LeQueau et al. [1983] have suggested that this source of free energy is more favorable to the amplification of AKR than the loss cone region. The third region associated with a source of free energy is a "bump" in the trapped region of the distribution with its peak near perpendicular pitch angles and energy between 0.5 to 1 keV. The presence of this bump causes the distribution function to have positive perpendicular slopes $(\frac{\partial F}{\partial v_\perp})$ at pitch angles near 90° and in a sense acts to bridge all three regions of free energy into almost a single continuous region of positive $(\frac{\partial F}{\partial v_\perp})$ at lower energies. Figure 9b which shows

the region of positive $(\frac{\partial F}{\partial v_\perp})$ in a distribution function measured on day 237 of 1976 (Figure 9a), demonstrates that at low velocities perpendicular gradients are positive for almost all pitch angles, and as one goes to higher energies, positive $(\frac{\partial F}{\partial v_\perp})$ is limited to pitch angles away from 90°.

C. Method of Growth Rate Calculations

In order to calculate growth rates of AKR and Z-mode radiation, we use the electron distribution function measured by the S3-3 satellite in the auroral zone on day 237 of 1976. The growth rate expression is given by Equation (A5) in the Appendix. It is clear from the delta functions in Equations (A4 and A9) that the growth rate is determined by integration along the resonance ellipse in velocity space. In order to carry out this integration, $(\frac{\partial F}{\partial v_\parallel})$ and $(\frac{\partial F}{\partial v_\perp})$ must be known along the resonance ellipse. Using the electron distribution function shown in Figure 9, $(\frac{\partial F}{\partial v_\parallel})$ and $(\frac{\partial F}{\partial v_\perp})$ were numerically calculated and integrated along the ellipse. To verify the accuracy of the integration routine, the growth rate (ω_i) was checked using a test analytic distribution function and the error in ω_i was found in all cases to be less than 20%. The integration errors are a combination of approximation, interpolation and truncation errors which are involved in the numerical procedure.

D. Growth Rate Calculations

Since in the case of AKR (and n = 1) Y is always less than one, it is clear that waves travelling in the upward direction can only resonate with the electrons in the loss cone, and the downgoing waves can only resonate with the electrons in the "hole" region. In Figure 10, the growth rates of both the upgoing and the downgoing AKR are shown for $f_{pc} = 0.05\ f_g$ which corresponds to a cold electron density slightly larger than the warm electron density, and a wave normal angle of 80°. As can be seen in Figure 10a, for waves travelling upward, two regions of growth and one region of damping exist. In order to understand Figure 10a, the three resonance ellipses A, B, and C shown in Figure 11, corresponding to values of Y equal to 0.997, 0.995, and 0.990, respectively, were superimposed on the electron distribution function. Figures 10a and 11 clearly illustrate that when the resonance ellipse lies in the loss cone region, large growth rates are obtained and when the resonance ellipse lies out of the loss cone, negative growth rates are attained. Having seen the effect of the location of the resonance ellipse on ω_I, we can now explain why two regions of growth and one region of damping exist in Figure 10a.

As indicated before, very close to $f = f_{R=0}$ in Figure 10a the resonance ellipse is almost a point and therefore $\omega_I \simeq 0$. As Y decreases ($\Delta\omega/\omega_g$ increases) V_R and V_C get larger (see Figure 3). In other words, the resonance ellipse begins to grow and its center moves away from the origin as $\Delta\omega/\omega_g$ decreases. Resonance ellipses corresponding to the first growth region lie either completely or partially

in the loss cone and the contribution of positive $\partial F/\partial v_\perp$ in the growth rate integral is greater than the contribution of negative $\partial F/\partial v_\parallel$ and therefore ω_i is positive. Values of Y which fall in the damping region have corresponding resonance ellipses that lie partially or completely out of the loss cone region and the contribution from negative $\partial F/\partial v_\perp$ is greater than the positive $\partial F/\partial v_\perp$ contribution, therefore, ω_i is negative. As Y increases beyond the damping region, V_C continues to grow, however, V_R begins to shrink with the effect that resonance ellipses corresponding to the second growth region fall partially or completely in the loss cone region and consequently ω_i is positive again. As the frequency increases further the radius of the resonance circle shrinks to zero at the D=0 boundary and and $\omega_i = 0$ above this frequency. Note that although typically three regions of growth and damping exist in the growth rate plots, there are special cases where this is not true. For example, in Figure 12a we see that there is only one region of growth in the whole frequency range for which resonance is possible. This is due to the fact that the resonance ellipses corresponding to this frequency range all lie in the loss-cone region. In fact, if the wave normal angle and plasma parameters are such that the resonance ellipses lie entirely within the loss-cone region, then the damping region will not exist and the growth rate plot will consist of only one growth region. It is clear from Figure 3 that in order for the resonance ellipses to stay in the loss cone, the wave normal angle must be at or near the maximum wave normal angle allowed by the

resonance condition. Thus, for growths like that of Figure 12a, it is necessary but not sufficient to have large wave normal angles.

In Figure 10b, ω_i for the downgoing AKR is shown. In contrast to waves travelling upward, only two bands occur, a narrow growth band and a much wider damping region. This can be explained by noting that for the downgoing AKR, only the resonance ellipses corresponding to frequencies near $f_{R=0}$ fall in the "hole" region, and therefore only a narrow band of frequencies above $f_{R=0}$ can be amplified (see Figure 11). As was mentioned earlier, Dusenbery and Lyons [1982] pointed out the possibility that the "hole" region in the downgoing side of the distribution may be a source of free energy for AKR. LeQueau et al. [1983] in a detailed analytical study and by using model electron distribution functions have argued that this region of the distribution function is the main source of free energy and that AKR is mostly amplified when it is propagating towards the Earth. The growth and damping rates shown in Figures 10b and 12b, however, seem to indicate that since the free energy region associated with the downgoing electrons is confined to smaller pitch angles and velocities, it is unlikely that this region alone can be responsible for the generation of AKR, especially since the growth rates for the downward waves are comparable to or smaller than those for the upward waves. Another argument which tends to show that it is unlikely for the "hole" region to be the primary source of free energy in the generation of AKR is that since the growth band is very narrow and just above the cutoff frequency, downgoing waves remain in the amplification region for only

a very short time before they go through a reflection, even though the group velocity in this regime is very small. In addition, waves will not be able to maintain a large wave normal angle (which is necessary to insure resonance with electrons in the "hole") throughout their propagation in the growth region. Therefore, in the cyclotron maser theory of AKR, the loss cone region of the electron distribution seems to play a more crucial role.

In Figure 13, the growth and damping rates of the upgoing AKR as a function of frequency and four different wave normal angles are shown. It is clear that substantial growth rates can only be obtained when $\theta \sim 80°$, and that when $\theta \lesssim 70°$ all waves are damped. The reason is that that as θ gets smaller most of the electrons resonating with the waves lie outside the loss cone region where $(\frac{\partial F}{\partial v_\perp})$ is mostly negative (see Section II.B). Thus, it is evident that with such growth rates, the only way that waves can be substantially amplified is if the ray paths are such that θ remains close to 80° for a considerable length of time. To see if this is indeed the case or not, it is necessary to perform a ray tracing study and calculate the path integrated growth of AKR.

IV. RAY TRACING

In this chapter Poeverlein's graphic method of ray tracing is briefly discussed, and the results of the three-dimensional ray tracings for the auroral kilometric radiation are presented.

In Poeverlein's graphic method of ray tracing it is assumed that waves propagate in a plane stratified medium. This method utilizes the fact that although the wave vector $\vec{k}$ changes along the ray path, the components of $\vec{k}$ in the stratified plane remain constant throughout the propagation.

In this study, it is assumed that the stratified plane $(\hat{x}, \hat{y})$ shown in Figure 14a, is perpendicular to the gradient of the magnetic field $(\vec{\nabla}B)$. This assumption can be justified by noting that since in the auroral region the f_p/f_g ratio is very small $(f_p/f_g \lesssim .1)$, any small variation of the electron density can be ignored and it is mainly the geomagnetic field (determined by a dipole model) that controls the refraction of the waves. In Figure 14a, $(\hat{i}, \hat{j}, \hat{k})$ forms a Cartesian coordinate system in which $\hat{k}$ is along the magnetic pole and $(\hat{i}, \hat{j})$ lie in the magnetic equator. The origin of the $(\hat{x}, \hat{y}, \hat{z})$ system is the launching point for all the rays and in this study it is located at radial distance of R = 13940 km, a magnetic latitude of $\lambda = 70°$ and a magnetic longitude of $L = 0°$. Note that the $(\hat{y}, \hat{z})$ plane lies on the $(\hat{k}, \hat{\ell})$ plane which defines a magnetic meridian.

Since the refraction of waves is assumed to be controlled by the Earth's dipolar magnetic field, the model for the electron density used in the present study is a simple one. The f_p/f_g ratio is kept constant at 0.05 throughout the region where the ray tracing is performed. This model is consistent with the fact that the gradients in the electron density have a negligible effect on the ray path when f_p/f_g ratio is small. It should, however, be mentioned that this simple model ignores the density enhancements within the auroral plasma cavity reported by Benson and Calvert [1979]. Consideration of these density enhancements which may result in partial reflection of the waves has led Calvert [1982] to a feedback model for the source of AKR.

As mentioned earlier, the origin of the $(\hat{x}, \hat{y}, \hat{z})$ system is the launching point for all rays. Once the wave frequency and the direction of $\vec{k}$ are chosen, the components of $\vec{N} = \frac{c\vec{k}}{\omega}$ along the $\hat{x}$ axis (N_{xo}) and the $\hat{y}$ axis (N_{yo}) are computed. These two components of $\vec{N}$ remain unchanged along the ray path. As the ray is stepped forward along the group velocity direction $\vec{v}_g$ (which is perpendicular to the index of refraction surface) a new value for the index of refraction is computed. By constructing a new coordinate system $(\hat{x}', \hat{y}', \hat{z}')$ parallel to $(\hat{x}, \hat{y}, \hat{z})$ and its origin located at the new position of the ray, the values of the wave normal angle θ and the azimuthal angle ϕ (see Figure 14b) are determined such that the components of $\vec{N}$ in the $\hat{x}'$ and $\hat{y}'$ direction are N_{xo} and N_{yo}, respectively. Note that although at the launching point, $\vec{B}$ is in the $(\hat{y}, \hat{z})$ plane, at subsequent points

along the ray path the local $\vec{B}$ will not lie in the $(\hat{y}', \hat{z}')$ plane unless initial $\phi = 0$, and ray propagates in the meridian plane.

Before looking at the specific ray paths that were computed in this study, it is helpful to review the general results of these ray tracings which are summarized in Figure 15. This figure shows the ray paths for four waves with different frequencies and initial $\vec{k}$ direction, all starting from the same point. Rays (a) and (b) lie in the front meridian plane (i.e., initially $\phi = 0$ and $\vec{k}$ has no longitudinal component). Ray (a) which has a frequency near the cutoff frequency is considerably refracted, whereas ray (b) which has a frequency much above the cutoff frequency suffers much less refraction. This is easily explained by noting that initially, the index of refraction N for ray (a) is very small (due to the fact that f is near $f_{R=0}$) and therefore the components of N in the stratified plane are very small. As ray (a) propagates, N gets larger and in order for the components of N in the stratified plane to remain constant, the wave normal angle θ has to decrease (note that $\vec{B}$ is nearly perpendicular to the stratified plane, i.e., β in Figure 14b is small). Ray (b) on the other hand has $N \sim 1$ and its index of refraction does not change appreciably as it propagates, and therefore does not suffer as much refraction. Rays (c) and (d) whose initial $\vec{k}$ does not lie in the front meridian plane (initial $\phi = 90°$) propagate in three dimensions from the front towards the back meridian plane. Again ray (c) with a frequency near the R-X cutoff frequency refracts substantially, whereas ray (d) with its frequency much above the cutoff frequency travels longitudinally without

too much refraction. As can be seen in Figure 15, rays (a) and (b) which initially have $\phi = 0$ propagate only in the radial and latitudinal directions, whereas rays (c) and (d) propagate mostly in the longitudinal and radial directions. Thus, as the initial ϕ increases, the rays travel more in the longitudinal direction and less in the latitudinal direction.

Having seen the general behavior of the R-X mode waves in the AKR source region, we now focus on six specific waves whose frequency and initial $\vec{k}$ direction are shown in Table 1. The ray paths of these waves are representative of the different types of ray paths that are observed. In Figure 16 the variations of the wave normal angle θ as a function of path length are shown. The total path length for each ray shown in this figure is 100 km. From Figure 16 one can draw the following conclusions. Rays #1 and #2 whose frequencies are near the cutoff frequency $f_{R=0}$, suffer substantial refraction, whereas rays #3 through #6 whose frequencies are well above $f_{R=0}$, do not suffer as much refraction. It is also evident that much of the refraction occurs in the first twenty kilometers of the ray path. As will be seen later, this effect plays a crucial role in preventing waves from getting amplified. Another point to notice in Figure 16 is that two rays with the same frequency but different initial azimuthal directions ϕ are refracted differently, with the wave propagating in the meridian plane suffering more refraction. The reason is that for a ray travelling in the meridian plane the magnitude of $\vec{B}$ changes more rapidly than for a ray propagating in the longitudinal direction. However, this

difference in refraction is not substantial, and as will be shown latter it does not lead to markedly different path integrated growths.

In Figure 17 the variations of the magnetic longitude and latitude of each of the six rays for a path length of 400 km are shown. The starting point for all the rays has a latitude of 70° and a longitude of 0°. The fact that rays #2 and #4 are propagating in the meridian plane is obvious. Note that since ray #2 undergoes more refraction than ray #4, it does not extend to as low a latitude as ray #4. In other words, ray #2 refracts upward much more than ray #4. It is evident in Figure 17, that rays #5, #3, and #1 with their initial $\phi = 90°$, travel mostly in the longitudinal direction with ray #1 propagating a bit more in the latitudinal direction due to more refraction. Finally, ray #6 whose initial azimuthal angle is $\phi = 20°$, travels both in the longitudinal as well as the latitudinal directions.

Having seen the general behavior of the waves in the auroral region, we now proceed to evaluate the growth of these waves by the cyclotron maser mechanism.

V. PATH INTEGRATED GROWTH OF AKR

A. The Path Integrated Growths Obtained From the S3-3 Distribution Function

As was mentioned earlier, although the electron distribution functions measured in the auroral region are unstable, with positive growth rates for waves in certain frequency ranges, this is not sufficient to insure that these waves will grow to sufficiently large amplitudes along the ray paths. In order to see whether refraction of waves can hamper their growth, we calculate the growth factor of the waves (G) defined as:

$$G \equiv \exp[g] = \exp\left[\int_0^L \frac{\omega_i(\ell')}{v_g(\ell')}\, d\ell'\right] \tag{11}$$

where $\omega_i(\ell')$ and $v_g(\ell')$ are the imaginary part of the frequency and the group velocity as a function of distance, respectively, and L is the path length. The group velocity v_g is given by:

$$v_g = \left[\left(\frac{\partial\omega}{\partial k}\right)^2 + \frac{1}{k^2}\left(\frac{\partial\omega}{\partial\theta}\right)^2\right]^{1/2} \tag{12}$$

where $(\frac{\partial\omega}{\partial k})$ and $(\frac{\partial\omega}{\partial\theta})$ are found by using the dispersion relation obtained in the cold plasma approximation. The value of v_g is zero when $f = f_{R=0}$ and rapidly approaches the speed of light as $\Delta f \equiv (f - f_{R=0})$ increases (see Dusenbery and Lyons [1982]).

Intensity measurements of AKR indicate that the growth of the cosmic noise background electric field by a factor of $G = e^{10}$ is sufficient to account for the observed intensities of the kilometric radiation, i.e., $g \sim 10$ gives the required amplification [Brown, 1973]. In Figure 18, a plot of g vs. L for the six different rays discussed in the last chapter are shown. In order to calculate g, it has been assumed that electron distribution functions similar to that shown in Figure 9, exist along the ray path. Figure 18 clearly illustrates that rays #1 and #2 with f near the cutoff, suffer heavy damping due to the rapid refraction that they undergo. In other words, although these rays start with θ sufficiently near 90° for large growth rates they cannot maintain these wave normal angles long enough to be amplified. Note also that, although ray #1 propagates in the longitudinal direction, its damping is similar to that of ray #2 which propagates in the meridian plane.

As can be seen in Figure 18, rays #3 and #4 which suffer much less refraction are initially amplified but are later absorbed. The maximum g for these rays is less than 0.5 and, therefore, the initial growths are not anywhere close to that required to account for the intensities of AKR. Similarly, rays #5 and #6 are initially amplified and suffer

subsequent damping. These rays, however, are amplified less and propagate a larger distance before getting damped. A comparison of g between rays #3 and #4 or #5 and #6 demonstrates that rays propagating in the longitudinal direction travel larger distances before getting absorbed. This is the result of the fact that for a given frequency, waves propagating in the longitudinal direction suffer less refraction.

Judging from the results shown in Figure 18, it seems certain that with electron distribution functions like those measured by the S3-3 satellite, the cyclotron maser mechanism cannot account for the generation of AKR. Thus, if the cyclotron maser instability is to remain a viable mechanism for the generation of AKR it is necessary for the electron distribution in the loss cone to have steeper slopes $(\frac{\partial F}{\partial v_\perp})$ than those measured by S3-3 satellite. Since wave particle interactions tend to fill in the loss cone via pitch angle scattering, thus reducing the velocity space gradients, it is possible that electron distribution functions with steeper slopes do in fact exist. However, due to the limitations imposed by the angular (fields of view are 7° × 10° FWHM) and temporal (20 sec for a complete angular distribution) resolution of the S3-3 particle instrumentation, it is not possible that the existence of such distributions can be experimentally confirmed with existing data. In the remainder of this chapter, an attempt is made to find the minimum velocity space gradients in the loss cone that are required to amplify the cosmic noise background to the observed intensities of AKR.

B. Modeling of the Electron Distribution Functions With Steeper Slopes In The Loss Cone

To construct electron distribution functions with steeper slopes $(\frac{\partial F}{\partial v_\perp})$ in the loss cone than those measured by the S3-3 satellite, we consider the following physical arguments. Generally speaking, the electrons in the loss cone can be broken into three separate populations, one population consisting of the electrons that were pitch angle scattered into the loss cone via the wave particle interactions; the second population being composed of the backscattered electrons; and finally, the third population consisting of the electrons of ionospheric origin. The electron distribution function shown in Figure 9 was measured in the auroral region and at the radial distance of about 2.2 R_E where an electrostatic potential drop of about 1 kV with respect to the top of the ionosphere is believed to exist [Croley et al., 1978]. Since most of the ionospheric electrons have energies less than 1 keV, then one can assume that these electrons will not be able to reach the S3-3 satellite. As for the backscattered electrons, a detailed study of the collisions of the downgoing electrons with the particles in the ionosphere is required to determine their energy spectrum. Since such a study is beyond the scope of this paper, we simply assume that the backscattered electrons at the height of the S3-3 satellite have energies of a few hundred eVs and less so that they do not resonate with waves. Based on this assumption all the high energy electrons in the loss cone are due to pitch angle scattering, and therefore the electron distribution function prior to wave particle

interactions must have had an empty loss cone. Note, however, that even if the loss cone is empty, some limitations on the steepness of the slopes at the edges of the loss cone still exist. These limitations may be understood in the following way. At high altitudes the electrons are collisionless, however, as they approach the ionosphere they reach a point on the field line (M_1) where collisions become important. This point can be taken to be the mirroring point for the electrons and defines the loss cone angle α_1. It is obvious, however, that not all the electrons passing this point will immediately suffer a collision, and therefore some of these electrons will mirror back before suffering a collision. We now define a second point M_2 on the same field line and below M_1 such that all the electrons passing M_1 will either be mirrored back or scattered and lost before reaching M_2, i.e., the distance between M_1 and M_2 is on the order of an electron mean free path. We denote this distance by ΔM. Point M_2 defines a loss cone angle α_2 below which no particles exist in the loss cone. Since some electrons passing the point M_1 are scattered while others are mirrored before reaching M_2, one can see that the electron distribution in the loss cone drops gradually as one goes from α_1 to α_2. This scattering process can be used to put a limitation on the steepness of the slopes at the edge of the loss cone. Clearly as M_1 and M_2 approach each other then $(\frac{\partial F}{\partial v_\perp})$ becomes infinite and as the distance between M_1 and M_2 increases the gradients become less steep.

Chiu and Schultz [1978] used conservation of energy and the first adiabatic invariant to show that in the presence of parallel electric

fields, the loss cone boundary is defined by a hyperbola (see Figure 19) given by:

$$v_{\parallel}^2 - \left(\frac{B_\ell}{B} - 1\right)v_{\perp}^2 + \frac{2\,e}{m}(V_\ell - V) = 0 \qquad (13)$$

where B_ℓ and B are the magnetic field at mirror point and the observation point; V_ℓ and V are the electric potential at the mirror and the observation points, respectively; m is the electron mass, and e is its charge. Since B is measured by the S3-3 satellite, one need only know B_ℓ and $\Delta V \equiv (v_\ell - V)$ to determine the loss cone boundary given by Equation 13. As was mentioned earlier, typically $\Delta V = 1$ kV. Location of M_1 on the other hand is not exactly known and it can vary between 100 to 300 km above the Earth's surface. Note, however, that since B_ℓ does not change appreciably within this height interval, the loss cone boundary corresponding to M_1 can be adequately determined by assuming M_1 to be at an altitude of 300 km. This boundary is shown in Figure 19.

In order to construct an electron distribution function $F(v,\alpha)$ (where v is electron velocity) with steeper slopes in the loss cone than those in the S3-3 distribution function, point M_2 is chosen and the loss cone boundary corresponding to this point is determined. It is then assumed that $F(v,\alpha)$ is zero on and below the loss cone boundary of M_2 and that it rises linearly with v and α to the values of the S3-3 distribution on the loss cone boundary of M_1. $F(v,\alpha)$ outside the loss

cone is the same as the S3-3 distribution function. The assumption that $F(v,\alpha)$ rises linearly with v and α between the two loss cone boundaries can be justified by noting that these two boundaries are extremely close to each other and, thus, in an expansion of $F(v,\alpha)$ between these two boundaries the second and higher order terms can be ignored.

C. The Path Integrated Growths Obtained From the Modified Distribution Functions

The main objective of this section is to find the minimum slopes in the loss cone that are necessary to allow sufficient amplification of the kilometric radiation. To do this ΔM has been varied between 3 and 100 kilometers. As will be demonstrated shortly, the minimum required slopes are obtained when $\Delta M \sim 70$ km, which based on the following argument may be a reasonable value. As was mentioned earlier, ΔM is on the order of an electron mean free path (ℓ). Note that since ΔM denotes distance along the field line, setting $\Delta M \sim \ell$ means that in order for electrons with nonzero pitch angle to reach M_2, they must travel distances that are larger than a mean free path. Since ℓ varies with altitude, then ΔM also varies with height. In Figure 20, two plots of ℓ vs. altitude are shown. The electron mean free path was computed by using ionization cross sections of O_2, N_2 and O given by Equation 5 in Banks et al. [1974] at an electron energy of 5 keV. The atmospheric neutral densities were obtained from COSPAR International Reference Atmosphere, 1972. In panel (a) of Figure 20,

the "maximal" model of the atmosphere was used to determine the neutral densities as a function height, whereas in panel (b) the "minimal" model was utilized. It is clear from Figure 20 that depending upon the position of M_1, the value of ΔM can vary from a few meters up to hundreds of kilometers.

Having obtained rough estimates of ΔM, we now proceed with the growth rate calculations. In Figure 21, the growth rates of AKR resulting from a distribution function with $\Delta M = 3$ km are shown (run #2). The difference between these growth rates and those shown in Figure 13 is striking. As can be seen, large growth rates are obtained even when $\theta < 70°$. The reason is that, although for $\theta \lesssim 70°$, most of the resonating electrons are outside the loss cone region where $(\frac{\partial F}{\partial v_\perp})$ is negative, the large and positive $(\frac{\partial F}{\partial v_\perp})$ at the edge of the loss cone can easily overcome these negative contributions, and result in an overall growth for the waves. Note that $\omega_i = 0$ when the resonance ellipse falls below the loss cone boundary corresponding to point M_2, because there are no electrons below this boundary. Note also that the two loss cone boundaries corresponding to M_1 and M_2 are so close that they could not be resolved in Figure 19, and that at a given velocity the difference in the loss cone angles $\Delta\alpha = \alpha_1 - \alpha_2$ is on the order of 10^{-2} degrees.

The path integrated growths of rays #1 through #6 for the case of $\Delta M = 3$ km (run #2) are shown in Figure 22. It can be seen that rays #1 and #2 whose group velocity is much less than the speed of light are

greatly amplified within a very short distance (L ~ 5 km). On the other hand, rays #3 through #6 with v_g closer to the speed of light take a longer distance for a similar amplification. At any rate, it is obvious that all six rays are sufficiently amplified (g ~ 10) within 2 - 20 km, and thus the electron distribution function modeled by taking ΔM = 3 km is easily capable of generating AKR.

Similar calculations with M_2 at different altitudes have shown that the distribution function with the minimum required slopes is obtained when ΔM = 70 km (run #3). The growth rates for this case are shown in Figures 23 and 24 for θ varying from 80° down to 35°. Note that in this case both growth and damping can occur, depending upon the wave frequency. In Section (III.D) a qualitative picture was given as to why two regions of growth and one region of damping are obtained (see Figure 13a), when the S3-3 distribution function is used to calculate ω_I. In the case of the growth rates shown in Figures 23 and 24, however, a similar argument does not apply because of the absence of any electrons below the loss cone boundary of M_2. While in this case a qualitative picture for the behavior of the growth rates does not exist, close examination of the growth rate calculations indicate that the presence of trapped electrons in the distribution function plays an important role in the overall growth rates of the waves. In other words, while $(\frac{\partial F}{\partial v_\perp})$ is large and positive at the edge of the loss cone, it is not large enough to always overcome the negative $(\frac{\partial F}{\partial v_\perp})$ outside the loss cone, and thus whether the resonance ellipse for a particular frequency falls in the regions of positive or negative $(\frac{\partial F}{\partial v_\perp})$

in the trapped part of the distribution function, can affect the outcome of the growth rate calculations for that frequency.

Note that again the loss cone boundary corresponding to M_2 lies very close to that of M_1 and that at a given velocity $\Delta\alpha \sim 10^{-1}$ degrees. The path integrated growths of rays #1 through #6 corresponding to run #3 are shown in Figure 25. In this case rays #1 and #2 can be sufficiently amplified ($g \sim 10$) within 70 km, but on the other hand rays #3 and #4 are initially amplified and suffer subsequent damping. The reason for this difference can be seen by noting that for large Y ($Y > .99$) growth can only be obtained when $\theta \sim 80°$ or $\theta \lesssim 60°$. Since rays #1 and #2 suffer extensive refraction their wave normal angles soon become less than 60° and can therefore be amplified. The fact that these rays have group velocities much less than c also helps to reduce the path lengths required to obtain sufficient amplification. Rays #3 and #4 on the other hand do not suffer much refraction and therefore their wave normal angle will not go below 60°. These rays are therefore initially amplified (when $\theta \sim 80°$) but as they propagate they begin to damp. Rays #5 and #6 suffer even less refraction than rays #3 and #4. Therefore, it takes a longer distance before they begin to damp. It is clear from Figures 23 and 24 that rays with $Y < .99$ and initial $\theta_0 \sim 75°$ (not traced in this study) may also be amplified, however, since the group velocities of these waves would be close to the speed of light, the path lengths required for sufficient amplification would be on the order of 1000 km which is much too long.

VI. GENERATION OF Z-MODE RADIATION

A. Observations of the Z-Mode in the Auroral Zone

Broadband Z-mode emissions have been observed by the DE-1 spacecraft in the low density region over the auroral zone and polar cap [Gurnett et al., 1983]. The DE-1 measurements indicate that Z-mode radiation is usually most intense right below the gyrofrequency and the intensity falls at lower frequencies. In Figure 26 from Omidi et al. [1984] an electric field intensity spectrum is shown where the gyrofrequency is obtained from the magnetic field measured at the spacecraft [data provided by M. Sigura, 1983]. It is clear that the upper cutoff of the Z-mode radiation is below the electron gyrofrequency and no emission is observed between the gyrofrequency and the upper hybrid frequency. Although the Z-mode radiation in a cold plasma has a cutoff at $f_{L=0} = -f_g/2 + ((f_g/2)^2 + f_p{}^2)^{1/2}$, the DE-1 observations have shown that very rarely does the Z-mode radiation extend from f_g all the way down to $f_{L=0}$. Furthermore, spin modulation investigations have indicated that the radiation propagates nearly perpendicular to the magnetic field. Assuming a horizontally stratified medium and a vertical magnetic field, Gurnett et al. [1983] have shown that these observed characteristics of the Z-mode radiation can be due to propagation effects if the wave frequency in the source region is below the electron gyrofrequency. For example, an upward propagating wave generated

between f_p and f_g will travel with relatively little refraction until it approaches altitudes where $f \sim f_g$ and then it will start to bend horizontally and begin to propagate nearly perpendicular to the magnetic field and asymptotically approaching an altitude where $f = f_g$.

As far as the possible source of the Z-mode radiation is concerned, there has been no direct evidence from DE-1 observations indicating an exact source region [Gurnett et al., 1983]. However, sometimes as the spacecraft approaches the auroral zone, the intensity of the radiation increases. In addition, observations of the auroral hiss and Z-mode radiation have shown that the intensity variations of these emissions are very similar. This has led Gurnett et al. [1983] to conclude that the Z-mode radiation is most likely generated in the same general region as the auroral hiss, however, there is no hard evidence to confirm this hypothesis.

B. Generation Theories

As was pointed out in the introduction, until recently all theories of the Z-mode radiation have suggested that this radiation is produced by auroral electron beams at frequencies between f_g and f_{UHR}. Recently Omidi et al. [1984] and Hewitt et al. [1983] have proposed the cyclotron maser instability as a generation mechanism for the Z-mode radiation. In Omidi et al. [1984], it is suggested that Z-mode waves are generated at frequencies near and below the electron gyrofrequency by resonance with electrons moving in both directions along the magnetic field. Hewitt et al. [1983] on the other hand have suggested

that Z-mode is generated at frequencies between f_g and f_{UHR}, by resonance with the upgoing electrons in the loss cone.

This, however, is inconsistent with the DE-1 observations which indicate that no Z-mode emissions are present at frequencies between f_g and f_{UHR}. Moreover, if waves are generated at frequencies near f_{UHR}, the presence of horizontal density gradients are necessary to insure the propagation of these waves into regions where $f < f_g$. In the remainder of this chapter the generation mechanism proposed by Omidi et al. [1984] will be reviewed, and it will be demonstrated that this mechanism is in better agreement with the DE-1 observations.

As was mentioned earlier, the source region of the Z-mode radiation has not been exactly located, however, observations seem to indicate that this emission is most likely generated in the same general region as the auroral hiss. In this study, it is hypothesized that the Z-mode emissions are produced by the inverted-V electrons in the auroral zone. Since this radiation is usually observed by DE-1 at frequencies around and below 60 kHz, cyclotron resonance instability would indicate source regions at the radial distances of about 3 R_E and higher. It has been shown by Croley et al. [1978] that the parallel electric fields in the auroral regions extend to altitudes which are considerably higher than the S3-3 altitudes ($R \sim 2.2\ R_E$). Since features like the "bump" (trapped electrons) and the "hole" in the electron distribution used in the present calculations ($R \sim 2.2\ R_E$) are attributed to the existence of parallel electric fields, it is expected that the electron distributions at higher altitudes where the

Z-mode observed by DE-1 is believed to be generated also display these features.

C. Growth Rates of Z-Mode Radiation

From Equations (2a,b,c) it is evident that when $\theta = 90°$ the resonance ellipse becomes a circle with its center at the origin, and Equation (2c) shows that as Y increases the radius of this circle increases (Figure 27). In general, for θ near 90° the center of the ellipse is near the origin and its eccentricity is nearly zero. Therefore, when the wave frequency f is slightly below the gyrofrequency (i.e., Y is slightly greater than one) and θ is near 90°, the relativistic resonance condition allows waves to resonate with electrons in all three sources of free energy (in the auroral zone) mentioned in Section (III.B), and one would expect these waves to be amplified. Results of the growth rate calculations shown in Figure 28 clearly agree with the aforementioned hypothesis and indicate that for a band of frequencies just below the gyrofrequency, relatively large growth rates are obtained. Figure 27 shows three resonance circles superimposed on the electron distribution that clearly demonstrate wave amplification when the circle simultaneously passes through the loss cone, the "hole" and the "bump" region. Waves that resonate with electrons outside of these regions are damped. Specifically circle "C" which lies outside of the "bump" and "hole" region gives rise to damping even though part of the circle is still within the loss cone region. In Figure 28 the growth rates corresponding to two different values of X are shown which

indicate that as X increases the growth rates decrease. Note that at a given frequency this decrease is not due to a change in the resonance circle (for $\theta = 90°$ the radius is only a function of Y) but instead it is caused by the fact that as X increases the denominator in Equation (A5), $\omega\frac{\partial}{\partial\omega}\mathrm{Re}(\Lambda)$, increases and thus ω_i decreases. Therefore, the generation of the Z-mode radiation requires a very low density region.

In Figure 29 the growth rates of both the upgoing and downgoing Z-mode waves with $\theta = 85°$ are shown. This figure demonstrates that except for small growths at frequencies just below the gyrofrequency all waves are damped. The reason for this damping can be explained by noting that the resonance ellipses shown in Figure 30 are mostly in the regions where $\frac{\partial F}{\partial v_\perp} < 0$. Note that these ellipses correspond to waves travelling downward. Thus, we see that as θ decreases the center of the resonance ellipse moves away from the origin and its radius increases. Therefore, waves are not able to resonate with enough electrons with free energy to get amplified. As was mentioned earlier, it is possible that electron distribution functions with steeper slopes $(\frac{\partial F}{\partial v_\perp})$ than those used in the present calculations exist. If this is true, the actual growth rates can be larger, and it is possible that waves with $\theta = 85°$ and less can also be amplified.

We now wish to calculate the distances that waves have to travel in the source region before they reach the observed intensity levels. To do this it is necessary to know the group velocity v_g for $\theta = 90°$. The index of refraction for both the fast and the slow extraordinary mode is given by

$$N^2 = 1 - \frac{X}{Z} \tag{14}$$

where

$$Z \equiv 1 - \frac{Y_T^2}{2(1 - X)} - \left[\frac{Y_T^4}{4(1 - X)^2} + Y_L^2\right]^{1/2} ,$$

$$Y_T \equiv Y \text{ Sin } \theta \quad , \quad \text{and } Y_L = Y \text{ Cos } \theta \tag{15}$$

[Ratcliffe, 1959]. Setting $N^2 = \frac{c^2 k^2}{\omega^2}$ in Equation (14) and taking the derivative with $\theta = 90°$ yields the following expression for the group velocity

$$v_g \Big|_{\theta = 90°} = \frac{\partial \omega}{\partial k} = \frac{N\ c}{1 + \frac{X\ Y^2}{(1 - X - Y^2)^2}} \quad . \tag{16}$$

Equation (16) indicates that for $Y \sim 1$ and small X the group velocity is much less than the speed of light c, for example, $v_g \sim .03$ c, when $Y \sim 1$ and $X \sim .02$. As X increases v_g also increases so that in order to minimize the required path lengths it is necessary to limit X to small values, especially since ω_i increases as X decreases. Note that $v_g = c$ when $X = 0$, as one would expect.

It has been shown by Gurnett et al. [1983] that for upgoing waves with frequencies near and slightly below the gyrofrequency the waves undergo little or no refraction. Thus, the waves can travel large distances in the horizontal direction. To calculate path lengths corresponding to the growth rates in Figure 28 we assume that $\theta = 90°$ throughout the source region. Rough estimates indicate that amplification of the background noise electric field by e^{10} is large enough to account for the maximum intensities of the Z-mode radiation observed by DE-1. For these estimates the background noise has been taken to be black body radiation at a temperature of 3000°K, which is a typical ionospheric temperature. Using the growth rates in Figure 28 and the group velocities obtained from Equation (16) we have calculated the path lengths that correspond to growth of electric fields by e^{10}. These path lengths (L) are shown in Figure 31. The minimum distance is $L \sim 240$ km, which is not unreasonable, since this distance is comparable to the north-south extent of the auroral zone. Note that path lengths larger than 2000 km are not shown. It is clear from Figure 31 that as X increases so does L. This is because at higher densities growth rates are smaller and the group velocity is larger.

The above calculations show that waves within a narrow frequency band below the gyrofrequency grow to large amplitudes within reasonable distances. Clearly, if electron distributions with larger $(\frac{\partial F}{\partial v_\perp})$ do in fact exist, then this band can be wider, and even for larger values of X (e.g., X = .05), reasonable path lengths could be obtained. Thus, it is evident that the cyclotron maser instability is capable of

explaining why the Z-mode radiation is observed below the gyrofrequency and not between f_g and f_{UHR}. The assumption that waves with $\theta \sim 90°$ and $f \lesssim f_g$ propagate horizontally with little or no refraction is consistent with observations and allows this mechanism to amplify waves effectively. The presence of Z-mode radiation at frequencies well below the gyrofrequency could also be explained by the fact that the downgoing waves with wave normal angles near 90° can continue to travel both horizontally and downward for relatively large distances before going through reflection. Therefore, at any spacecraft location it is possible to observe waves that are generated at higher altitudes. A more rigorous study using ray tracing techniques should be performed to improve our knowledge of the ray paths and conceivably locate the source region.

Before concluding this chapter, it should be mentioned that occasionally Z-mode radiation is observed near $f_{L=0}$. Gurnett et al. [1983] have called this trapped Z-mode radiation because it may be trapped in a cavity formed by a local minimum in $f_{L=0}$. In this paper we have not considered the generation of these waves for which a different generation mechanism may be needed. This can be seen by noting that in order for waves to resonate with electrons in the free energy regions of the distribution, the wave frequency must be near the local electron gyrofrequency, which means $f_{L=0} \sim f_g$. From the definition of $f_{L=0}$ it is clear that $f_{L=0} \sim f_g$ when $f_p \sim \sqrt{2}\, f_g$, therefore in the low density regions where $f_p \ll f_g$ waves with $f \sim f_{L=0}$ can not resonate with the low energy electrons in the free energy regions of the distribution.

It is, however, conceivable that these waves are generated in some high density regions through the cyclotron maser instability.

VII. SUMMARY AND CONCLUSIONS

A. Summary

By studying the relativistic cyclotron resonance condition, it was shown that the essential features of this resonance condition are determined by two parameters, Y and $N_{\parallel}$. When $N_{\parallel} < 1$ the resonance condition defines an ellipse in velocity space and when $N_{\parallel} > 1$ only the portion of the ellipse to the left of the line $v_{\parallel} = c/N_{\parallel}$ is acceptable. It was also demonstrated that when $Y > 1$ the resonance ellipse encircles the origin, for $Y = 1$ it goes through the origin and when $Y < 1$, it lies entirely in the region of positive parallel velocities.

In the case of resonance with the free space R-X mode at $n = 1$, the dependence of the size and position of the resonance ellipse on the wave frequency, gyrofrequency, plasma frequency and wave normal angle has been explored. It was shown that for a given θ and ω_p/ω_g ratio there exists a certain frequency range for which resonance is possible and outside of which resonance does not occur. This frequency range is constrained by the D=0 boundary, whose equation in $(V_c/c, \Delta\omega/\omega_g)$ space is independent of ω_p. The plasma frequency to gyrofrequency ratio determines the maximum wave normal angle allowed by the resonance condition and it also determines the minimum energy of the resonating electrons. As the ω_p/ω_g ratio gets smaller, the maximum wave normal angle allowed gets larger and the minimum energy of the resonating

electrons becomes smaller. We have also demonstrated that for either N or Cosθ approaching zero the nonrelativistic cyclotron resonance cannot be approximated by the relativistic cyclotron resonance condition. Because the relativistic cyclotron resonance predicts small velocities for the resonating electrons only when $N_{\parallel}$ approaches 0, we conclude that the nonrelativistic cyclotron resonance should not be used for the right-handed extraordinary mode waves.

Using the electron pitch angle distribution obtained by the S3-3 satellite and including only the effects of cold electrons on the real part of the dispersion relation we have calculated growth rates for both the auroral kilometric and Z-mode radiation. In the case of AKR the resonance ellipse does not encircle the origin. Results of growth rate calculations show that for upgoing waves and $\theta \sim 80°$, two regions of growth and one region of damping exist. One growth region occurs very close to the extraordinary mode cutoff and the second one occurs at higher frequencies. It is also demonstrated that when $\theta < 70°$ no growth is obtained. Contrary to the upgoing waves, the downgoing waves can only be amplified in a narrow frequency band just above $f_{R=0}$, even when $\theta \sim 80°$. This study seems to indicate that in the cyclotron maser theory of AKR the dominant source of free energy is most likely to be the loss cone region of the electron distribution.

A three dimensional ray tracing study for AKR indicated that waves with frequencies near $f_{R=0}$ suffer substantial refraction whereas waves with frequencies much above $f_{R=0}$ undergo less refraction. It was also shown that for a given frequency waves propagating in the meridian

plane suffer more refraction than waves propagating in three dimensions.

Using the results of the ray tracings and the S3-3 electron distribution, the path integrated growths of six representative rays were computed. It was demonstrated that none of these waves could be substantially ($g \sim 10$) amplified. In order to find the minimum slopes $(\frac{\partial F}{\partial v_\perp})$ at the edges of loss cone that are required to sufficiently amplify waves, model electron distributions with larger $(\frac{\partial F}{\partial v_\perp})$ were constructed and path integrated growths were computed. These electron distribution functions were constructed under the assumptions that, one, the ionospheric electrons are not capable of reaching the S3-3 altitudes, and two, that the backscattered electrons have energies less than a few hundred eVs so that they do not resonate with waves. The results of growth rate calculations with the model electron distribution functions, showed that waves can be sufficiently amplified in short distance and that the cyclotron maser mechanism could be viable if electron distribution functions with steeper slopes exist in the auroral region.

Since the resonance ellipses corresponding to the Z-mode radiation encircle the origin, it is possible for these waves to simultaneously resonate with electrons in all three sources of free energy that are commonly found in the measured distribution functions in the auroral zone. Results of growth rate calculations for the Z-mode indicate that substantial growth rates are obtained when f is slightly below f_g and $\theta \sim 90°$. Assuming horizontal propagation and no refraction, the path

lengths required to account for the observed intensities of the Z-mode radiation were calculated and it was shown that for a narrow frequency band near f_g path lengths less than 400 km are obtained. These calculations suggest that the Z-mode radiation may be accounted for by the cyclotron maser theory.

B. Conclusions

We have seen that the cyclotron maser mechanism can be responsible for the generation of both auroral kilometric and Z-mode radiation. In the case of the latter one, the study presented here is both encouraging and preliminary. Clearly lack of detailed electron distribution functions at altitudes higher than the S3-3 altitudes makes it unclear as to what extent the electron distributions at say 3 to 4 R_E resemble those at lower altitudes (2.2 R_E). The answer to this question can be decisive as to whether the proposed mechanism can be a viable one at higher altitudes or not. In the case of AKR, it has been demonstrated that steep slopes at the edges of loss cone are required to make the cyclotron maser mechanism a viable one. Although the assumptions made about the backscattered and the ionospheric electrons may not be unreasonable, one cannot be sure that electron distribution functions such as those used in runs #2 and #3 do in fact exist in the auroral region. However, future observations and a more detailed theoretical study of the collisions of the downgoing electrons with the ionospheric particles, and the determination of the energy spectrum of the backscattered electrons at high altitudes, can clearly shed more light on this problem.

Finally, a few comments on the laser feedback model proposed for the generation of AKR by Calvert [1982] are in order. In this model density irregularities are employed to partially reflect the waves and thereby allow an oscillator type mechanism to operate. It has been pointed out by Calvert [1982] that in this model, a total wave growth of about 40 dB per loop is required. It is clear from Figure 18 that such gains cannot be achieved by the S3-3 electron distribution function. In addition, since a wave propagating along a loop will at some portions of the loop (downgoing side) resonate with the downgoing electrons and most probably be damped the amplification along the upgoing portion of the loop will have to compensate for this damping. This again demonstrates the need for steeper slopes in the loss cone, if the cyclotron maser mechanism is to remain a viable one.

TABLE 1. The Initial Conditions of the Six Rays Traced In This Study

Ray Number	$Y_o \equiv f_{go}/f$	θ_o in degrees	ϕ_o in degrees
1	0.997	85°	90°
2	0.997	80°	0.0°
3	0.992	85°	90°
4	0.992	85°	0.0°
5	0.990	85°	90°
6	0.990	85°	20°

f_{go} = 160 kHz

$f_p = 0.05\ f_g$

$$Y_{R=0} = \frac{f_{go}}{f_{R=0}} = 0.9975$$

Figure 1 A spectrogram of the electric field intensities for a nightside crossing of the auroral region by the DE-1 spacecraft.

A-G82-926-3

ELECTRIC FIELD, DE-I, NOVEMBER 5, DAY 309, 1981

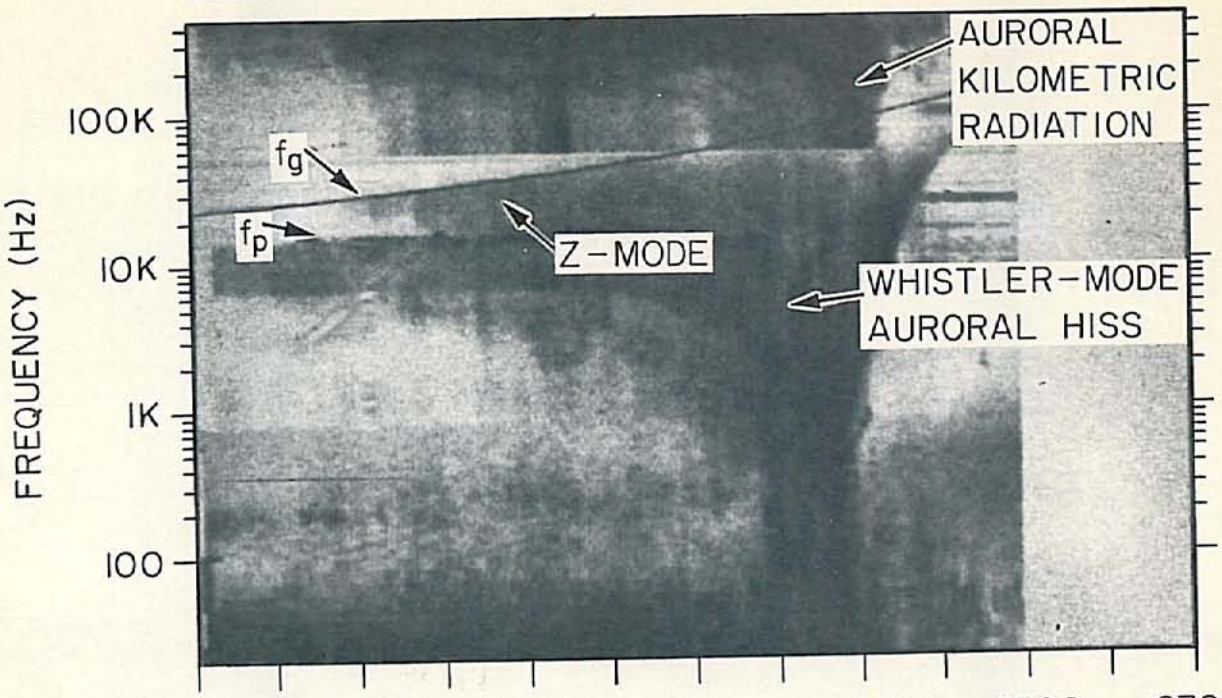

UT	0520	0540	0600	0620	0640	0700	0720
R (R_E)	4.21	3.92	3.56	3.10	2.55	1.90	1.24
L		93.56	35.72	13.56	5.38	2.19	1.53
MLT	13.70	16.16	17.80	18.74	19.37	19.88	20.59
λ_m (DEG)	79.07	77.25	71.04	61.33	47.09	23.67	-25.18

Figure 2 Six resonance ellipses corresponding to different values of Y and $N_{\parallel}$ are shown. The portion of the ellipse shown by broken line does not correspond to resonance. The resonance ellipse goes through $v_{\parallel} = c$ whenever $N_{\parallel} = 1$.

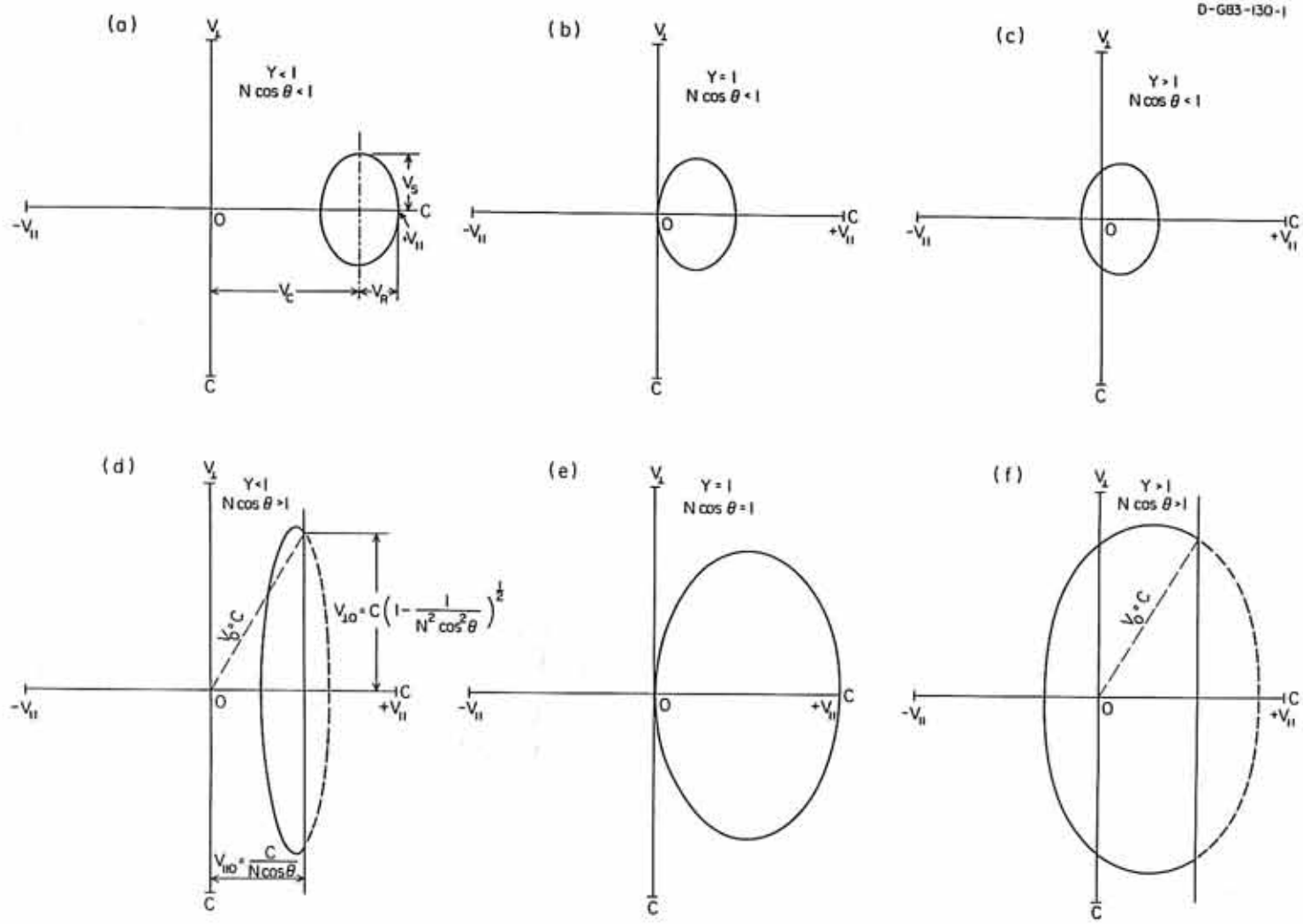

UNIT: C = SPEED OF LIGHT

Figure 3 V_c/c, V_R/c (in the case of resonance with AKR) as functions of $(\omega-\omega_g)/\omega_g$ for two f_p/f_g ratios and a number of wave normal angles.

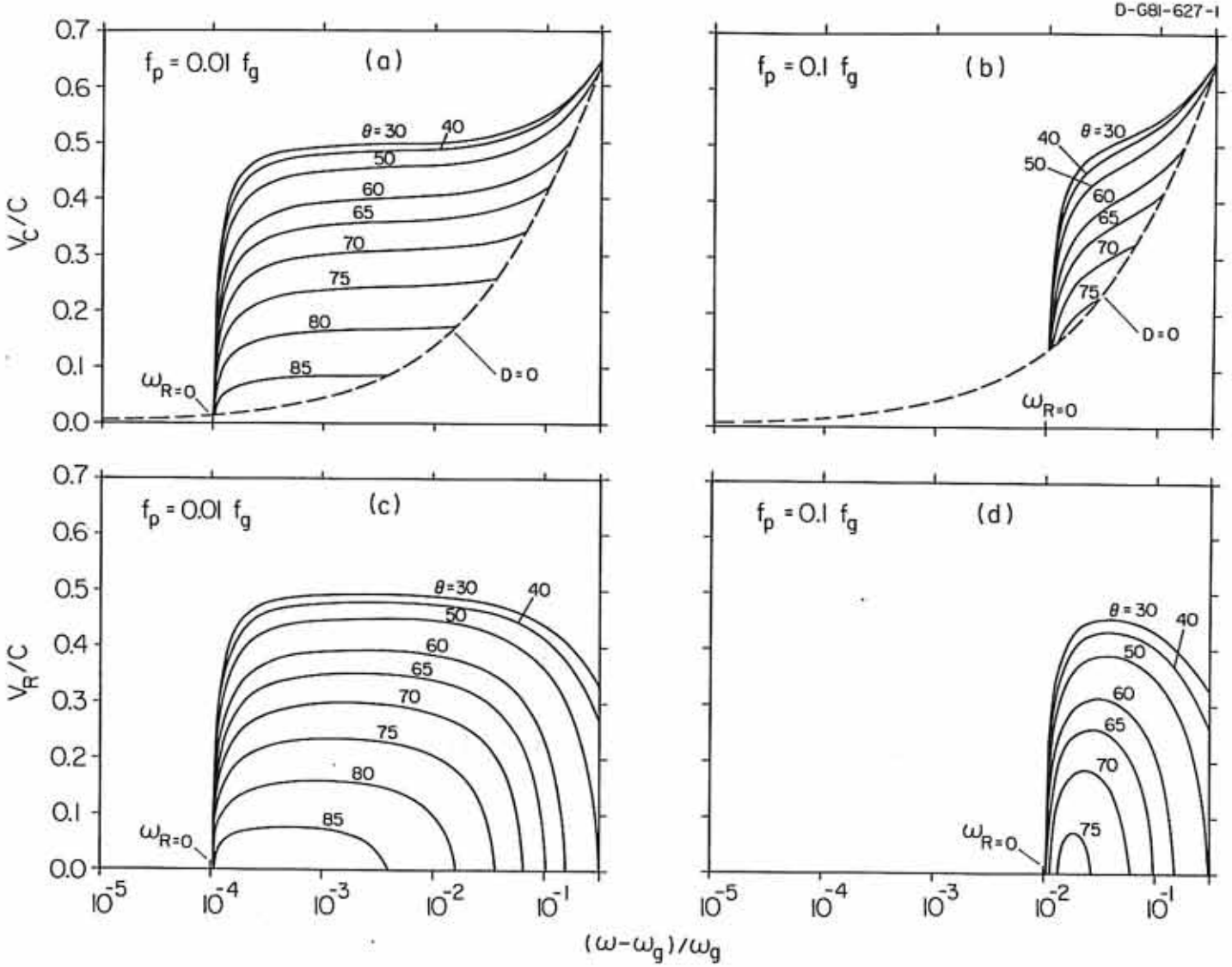
D-G81-627-1
$f_p = 0.01\ f_g$
(a)
$f_p = 0.1\ f_g$
(b)
$f_p = 0.01\ f_g$
(c)
$f_p = 0.1\ f_g$
(d)
V_C/C
V_R/C
$\theta = 30$
40
50
60
65
70
75
80
85
D = 0
$\omega_{R=0}$
0.0
0.1
0.2
0.3
0.4
0.5
0.6
0.7
10^{-5}
10^{-4}
10^{-3}
10^{-2}
10^{-1}
$(\omega-\omega_g)/\omega_g$

Figure 4 Index of refraction for the free space R-X mode as a function of $(\omega-\omega_g)/\omega_g$ for two f_p/f_g ratios. The index of refraction goes to zero at the extraordinary mode cutoff, $\omega_{R=0}$, for all wave normal angles.

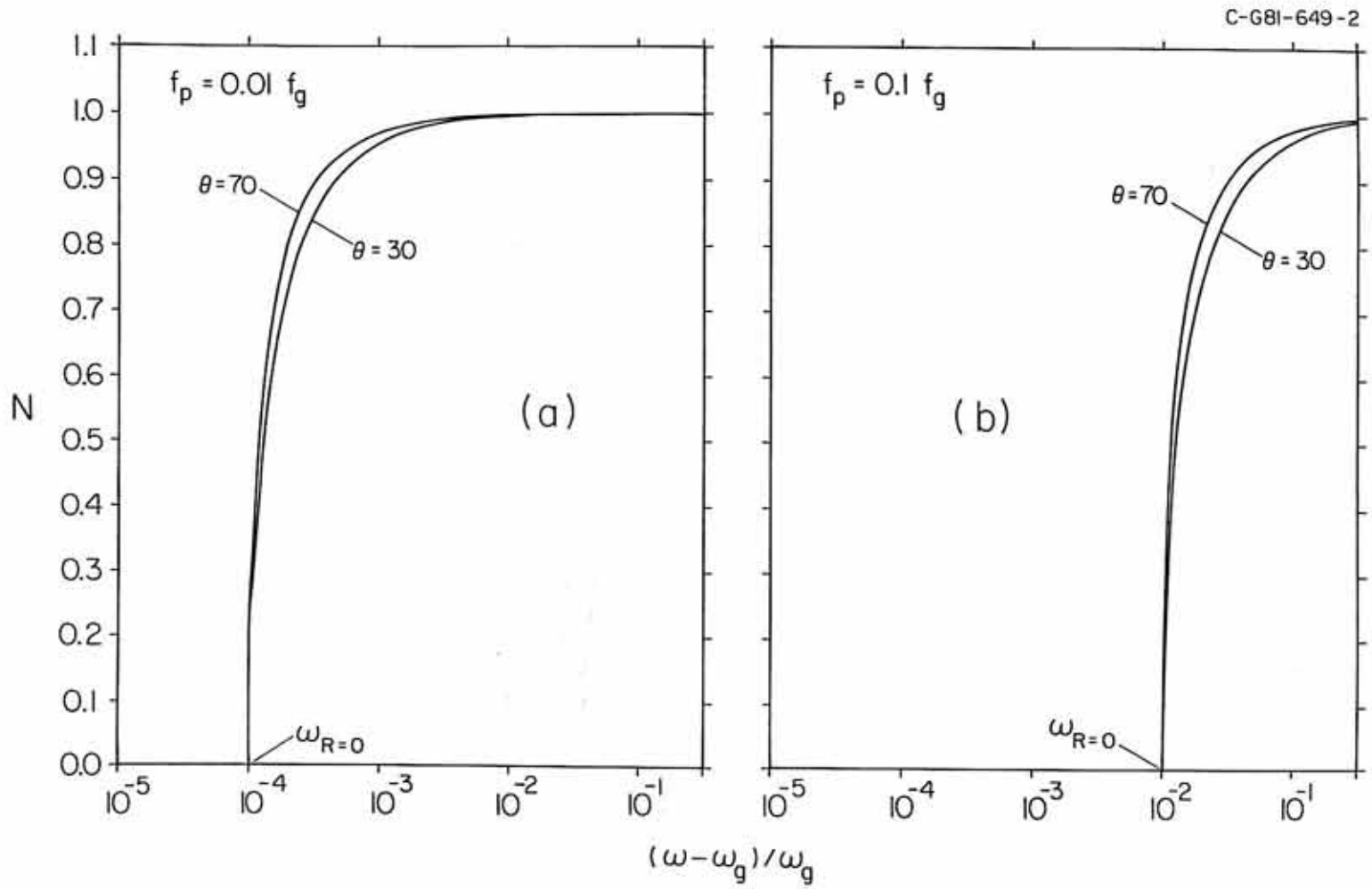
C-G81-649-2
$f_p = 0.01\ f_g$
$f_p = 0.1\ f_g$
$\theta = 70$
$\theta = 30$
$\omega_{R=0}$
(a)
(b)
N
1.1
1.0
0.9
0.8
0.7
0.6
0.5
0.4
0.3
0.2
0.1
0.0
10^{-5}
10^{-4}
10^{-3}
10^{-2}
10^{-1}
$(\omega-\omega_g)/\omega_g$

Figure 5 Relativistic resonance ellipses (for AKR) in velocity space for a number of wave normal angles and two f_p/f_g ratios. ω is near $\omega_{R=0}$ in (a, c) but is not so close in (b, d).

D-681-637-1

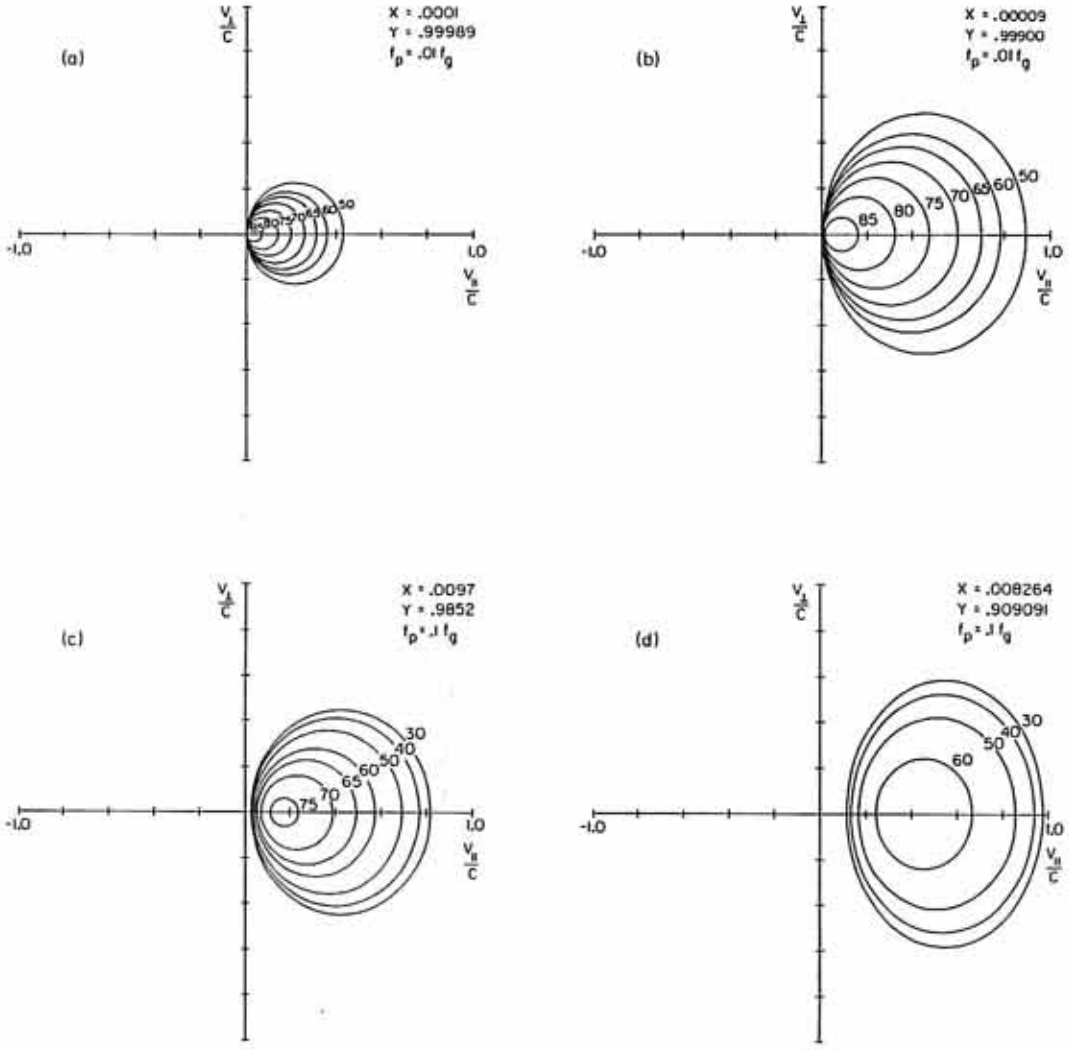
(a)
X = .0001
Y = .99989
f_p = .01 f_g
(b)
X = .00009
Y = .99900
f_p = .01 f_g
(c)
X = .0097
Y = .9852
f_p = .1 f_g
(d)
X = .008264
Y = .909091
f_p = .1 f_g
$\frac{V_\perp}{c}$
$\frac{V_\parallel}{c}$
-1.0
1.0
85
80
75
70
65
60
50
40
30

Figure 6 Shaded areas determine values of X and Y for which resonance with free space R-X mode is possible. The shaded region is bounded by the "D=0 boundary".

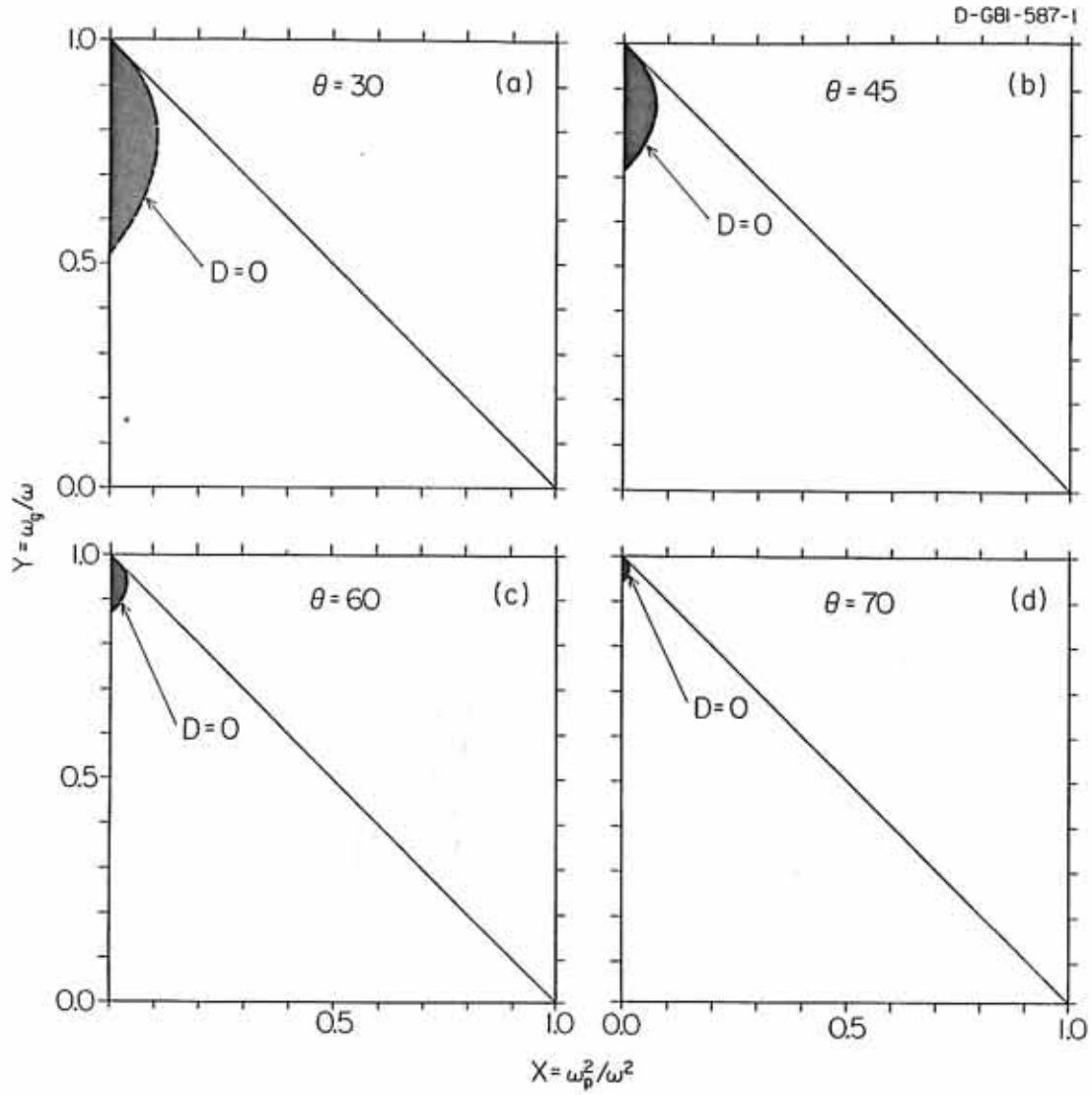
D-G81-587-1
θ = 30
(a)
D = 0
θ = 45
(b)
D = 0
θ = 60
(c)
D = 0
θ = 70
(d)
D = 0
1.0
0.5
0.0
0.0
0.5
1.0
Y = ω_q/ω
X = ω_p²/ω²

Figure 7 Contours of minimum energy of resonating electrons (with AKR) in keV. All contours are bounded by the D = 0 boundary.

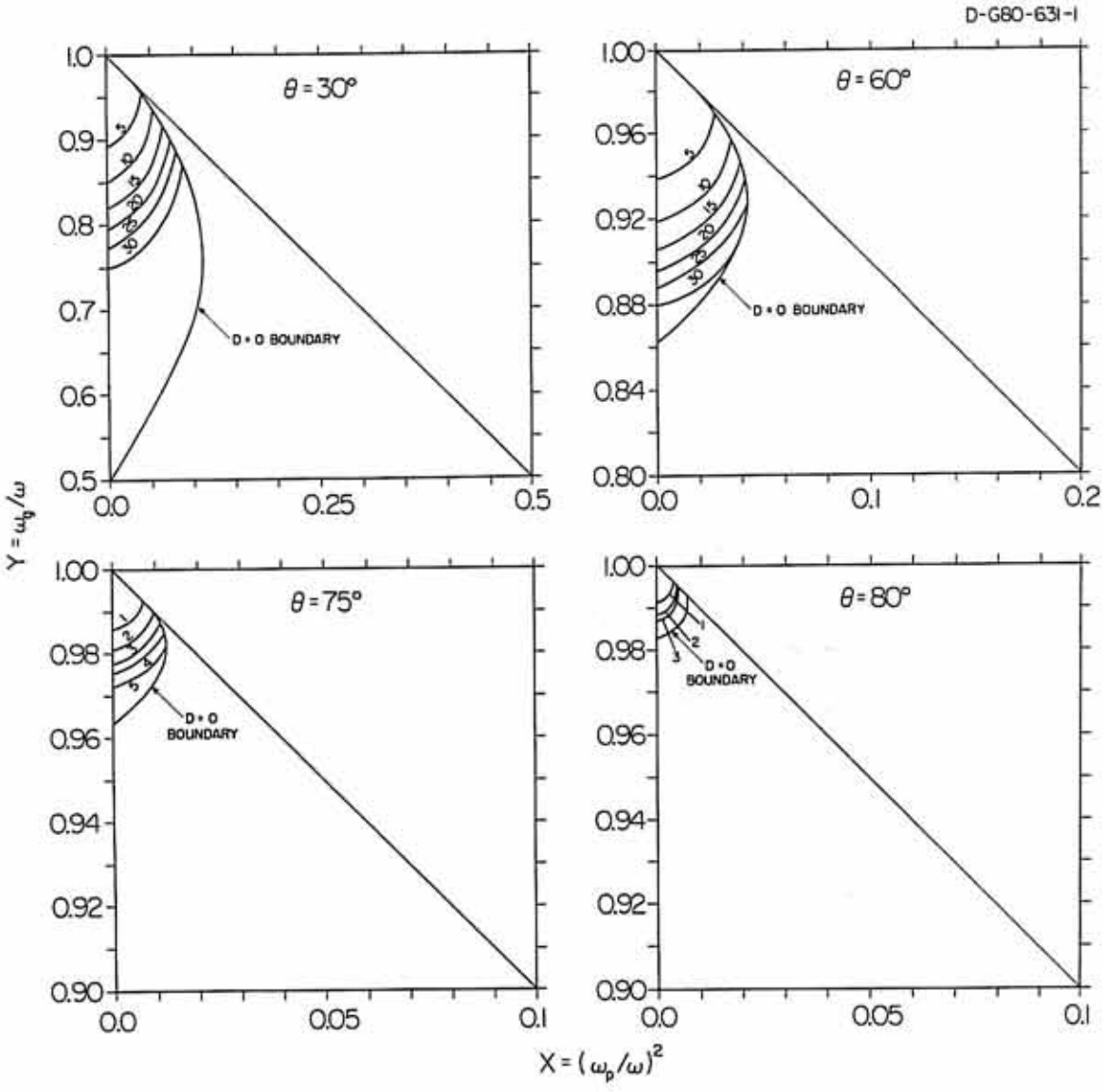
D-G80-631-1
θ = 30°
θ = 60°
θ = 75°
θ = 80°
D = 0 BOUNDARY
Y = ω_b/ω
X = (ω_p/ω)²

Figure 8 Four resonance ellipses for the Z-mode. As θ increases the eccentricity decreases and a larger portion of the ellipse corresponds to resonance.

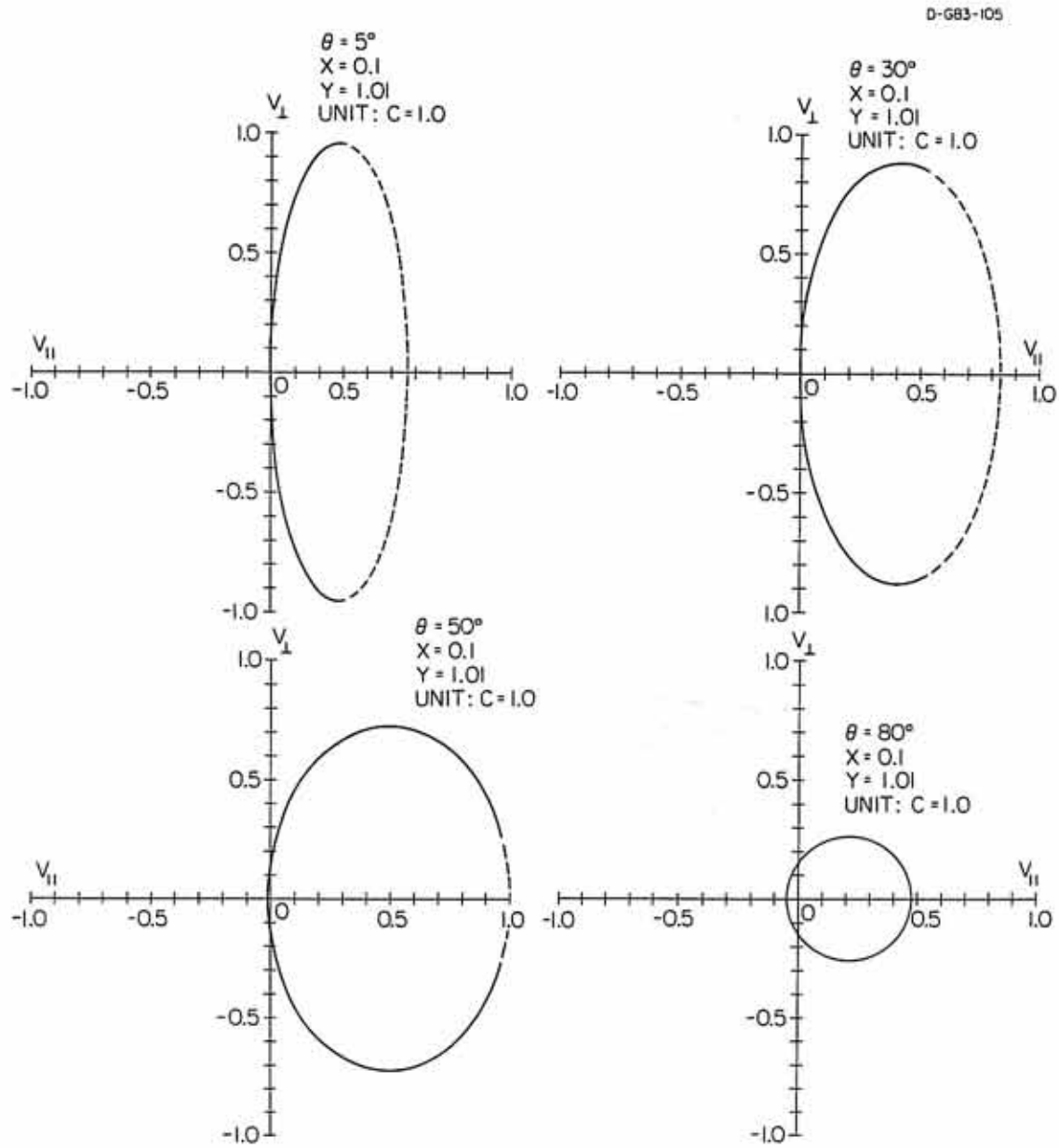
D-GB3-105
θ = 5°
X = 0.1
Y = 1.01
UNIT: C = 1.0
θ = 30°
X = 0.1
Y = 1.01
UNIT: C = 1.0
θ = 50°
X = 0.1
Y = 1.01
UNIT: C = 1.0
θ = 80°
X = 0.1
Y = 1.01
UNIT: C = 1.0
V⊥
V∥
1.0
0.5
0
-0.5
-1.0

Figure 9 The electron distribution used in calculating growth rates for AKR and Z-mode radiation is shown in 9a. The shaded area in 9b corresponds to the region of positive $\frac{\partial F}{\partial v_\perp}$ in the distribution shown in 9a. Note the different scalings in 9a and 9b.

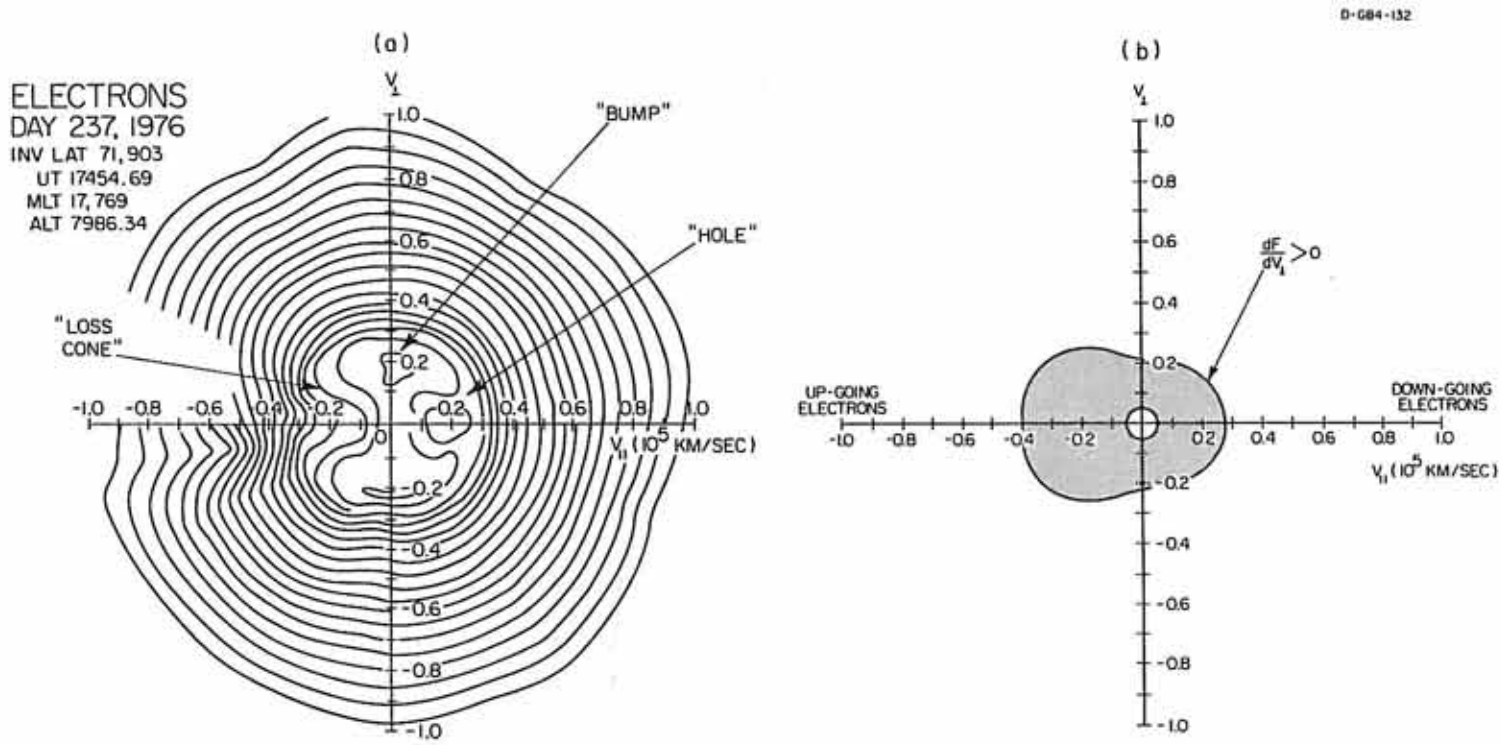
D-G84-132
(a)
ELECTRONS
DAY 237, 1976
INV LAT 71,903
UT 17454.69
MLT 17,769
ALT 7986.34
"BUMP"
"HOLE"
"LOSS CONE"
$V_\perp$
$V_\parallel$ (10^5 KM/SEC)
(b)
$\frac{dF}{dV_\perp} > 0$
UP-GOING ELECTRONS
DOWN-GOING ELECTRONS
$V_\perp$
$V_\parallel$ (10^5 KM/SEC)

Figure 10 Growth rates of auroral kilometric radiation for $f_{pc} = 0.05\ f_g$. In 10a waves are travelling upward and in 10b they are travelling downward.

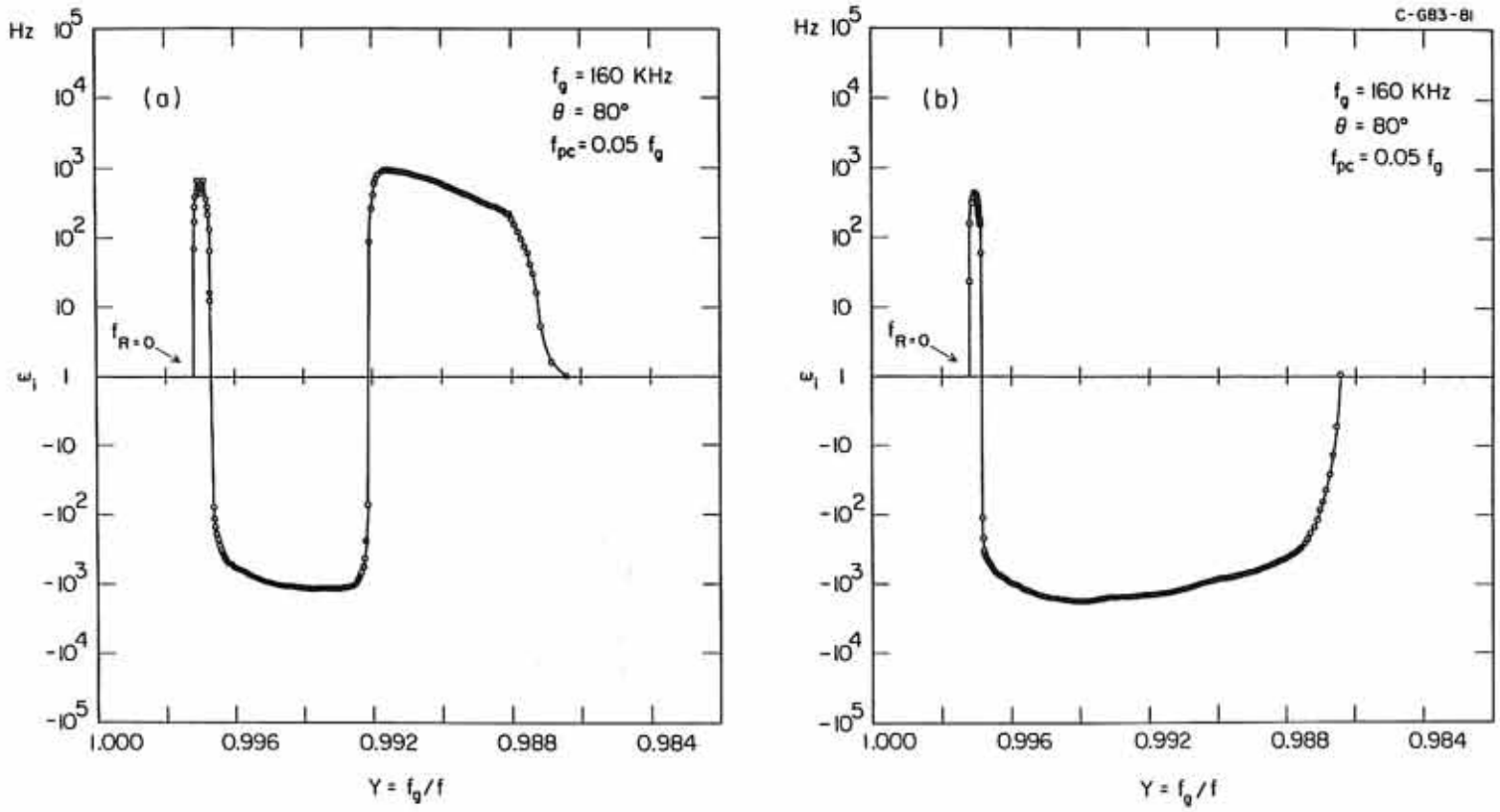
C-683-81
(a)
(b)
f_g = 160 KHz
θ = 80°
f_{pc} = 0.05 f_g
$f_{R=0}$
Hz
ω_i
10^5
10^4
10^3
10^2
10
1
-10
-10^2
-10^3
-10^4
-10^5
1.000
0.996
0.992
0.988
0.984
$Y = f_g/f$

Figure 11 Three resonance ellipses corresponding to $Y = .997$ (A), $Y = .995$ (B), and $Y = .990$ (C) are superimposed on both sides of the distribution. Ellipse (C) corresponds to growth for upgoing waves and damping for the downgoing waves.

C-G83-108

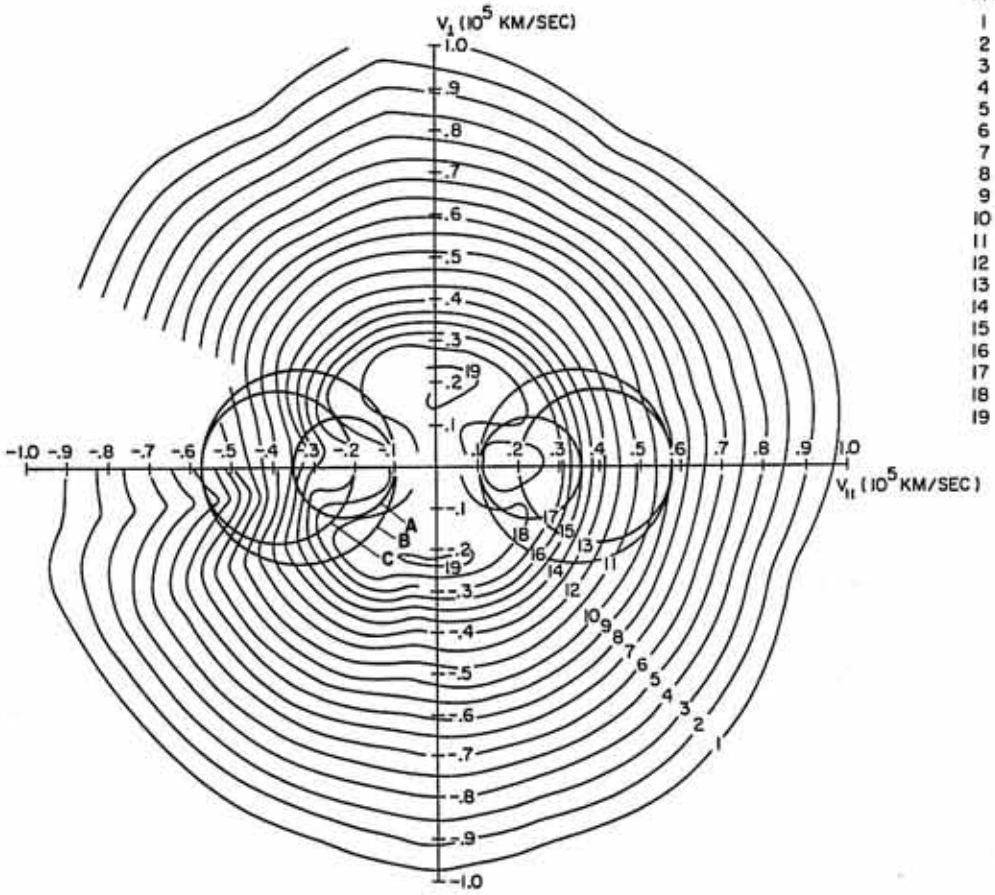

	f(v) [SEC^3/KM^6]
1	.100E-04
2	.215E-04
3	.464E-04
4	.100E-03
5	.215E-03
6	.464E-03
7	.100E-02
8	.215E-02
9	.464E-02
10	.100E-01
11	.215E-01
12	.464E-01
13	.100E+00
14	.215E+00
15	.464E+00
16	.100E+01
17	.215E+01
18	.464E+01
19	.100E+02

Figure 12 Growth rates of auroral kilometric radiation for $f_{pc} = 0.06\ f_g$. For upgoing waves no damping region exists but in the case of downgoing waves a wide band corresponds to damping.

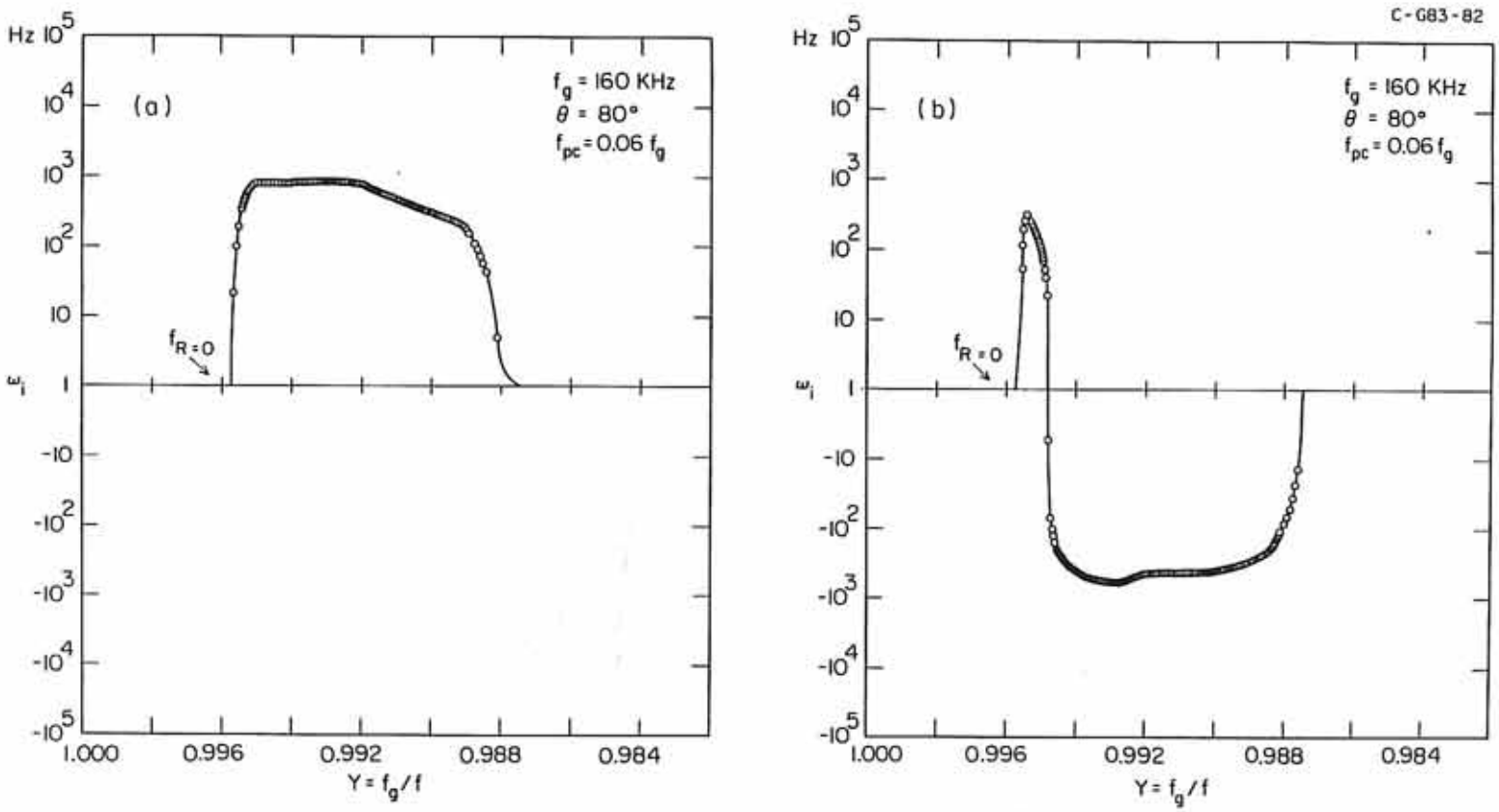
C-G83-82
(a)
(b)
f_g = 160 KHz
θ = 80°
f_{pc} = 0.06 f_g
$f_{R=0}$
Hz 10^5
10^4
10^3
10^2
10
1
-10
-10^2
-10^3
-10^4
-10^5
ω_i
1.000
0.996
0.992
0.988
0.984
$Y = f_g/f$

Figure 13 Growth and damping rates of upgoing AKR as a function of frequency for four wave normal angles are shown. ω_i was computed by using the exact distribution function measured by the S3-3 satellite, run #1.

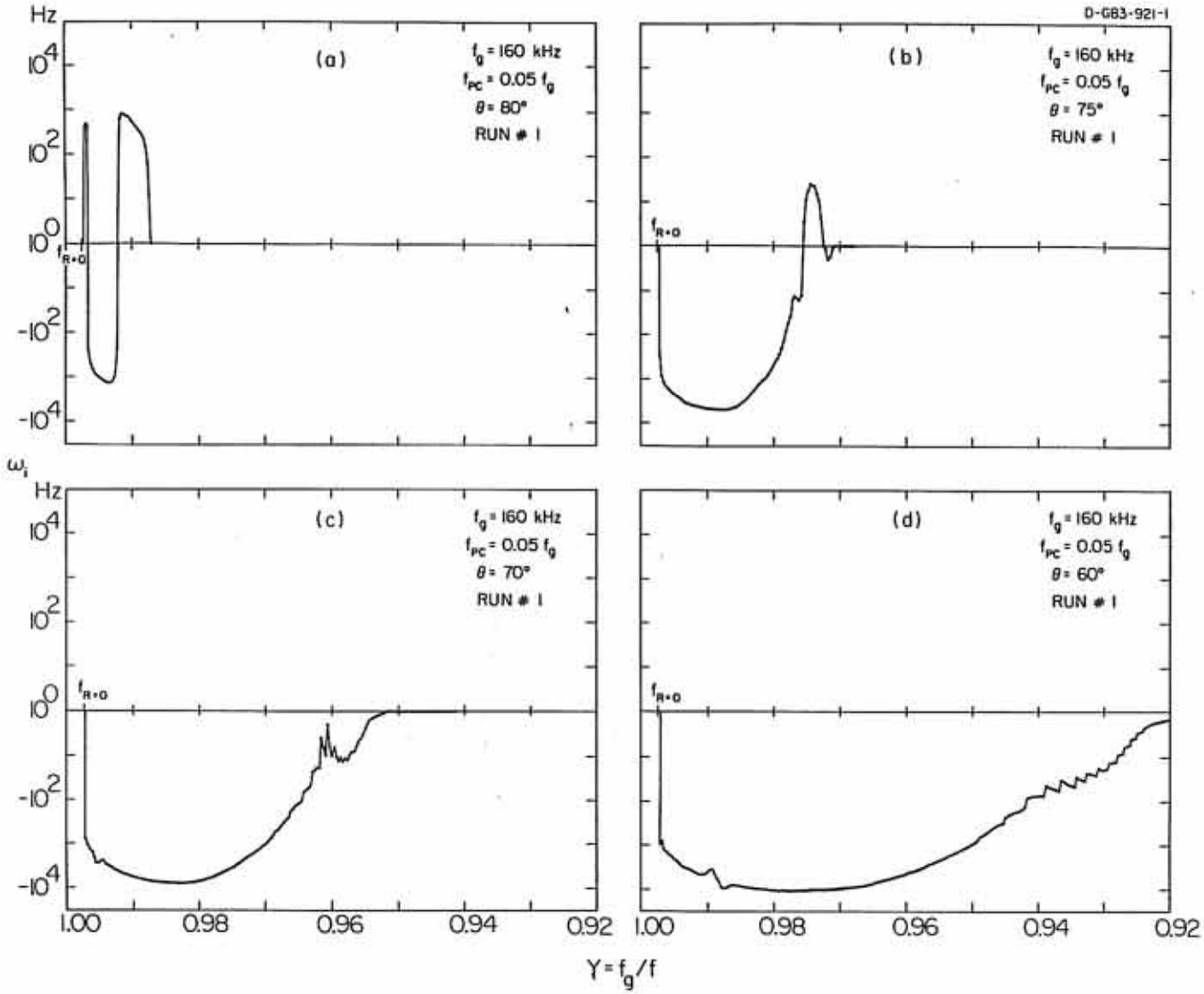
D-GB3-921-1
Hz
10^4
10^2
10^0
-10^2
-10^4
ω_i
(a)
f_g = 160 kHz
f_{PC} = 0.05 f_g
θ = 80°
RUN # 1
$f_{R=0}$
(b)
f_g = 160 kHz
f_{PC} = 0.05 f_g
θ = 75°
RUN # 1
$f_{R=0}$
(c)
f_g = 160 kHz
f_{PC} = 0.05 f_g
θ = 70°
RUN # 1
$f_{R=0}$
(d)
f_g = 160 kHz
f_{PC} = 0.05 f_g
θ = 60°
RUN # 1
$f_{R=0}$
1.00
0.98
0.96
0.94
0.92
$Y = f_g/f$

D-683-929

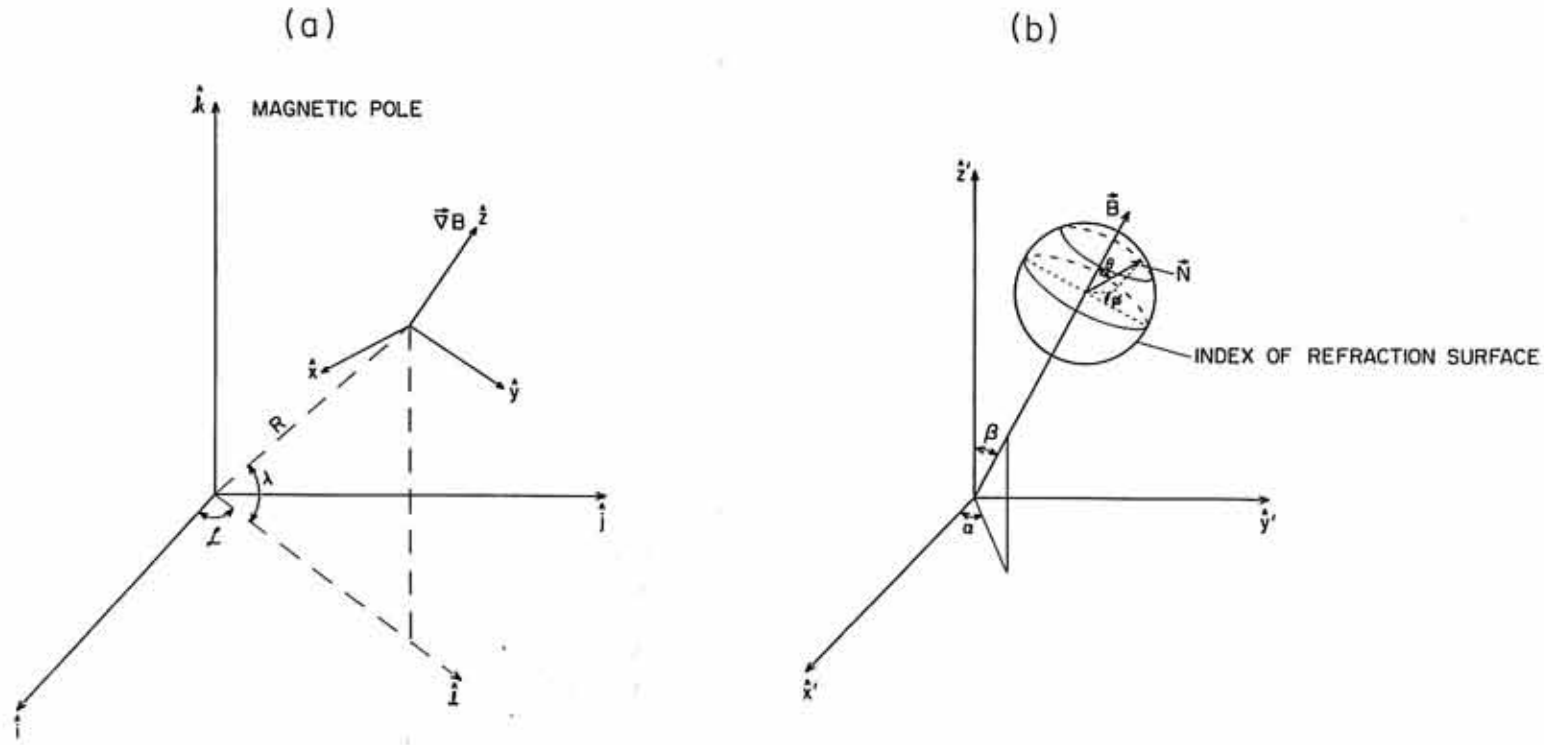
(a)
MAGNETIC POLE
$\vec{\nabla}B$
$\hat{z}$
$\hat{x}$
$\hat{y}$
R
λ
$\mathcal{L}$
$\hat{k}$
$\hat{j}$
$\hat{i}$
$\hat{I}$
(b)
$\hat{z}'$
$\vec{B}$
$\vec{N}$
β
α
INDEX OF REFRACTION SURFACE
$\hat{y}'$
$\hat{x}'$

Figure 15 Typical ray paths for four waves are shown. Rays (a) and (b) propagate in the front meridian plane, whereas rays (c) and (d) travel in the longitudinal as well as radial and latitudinal directions. Rays (a) and (c) have frequencies near the cutoff where as rays (b) and (d) have frequencies much above the cutoff.

C-G83-917

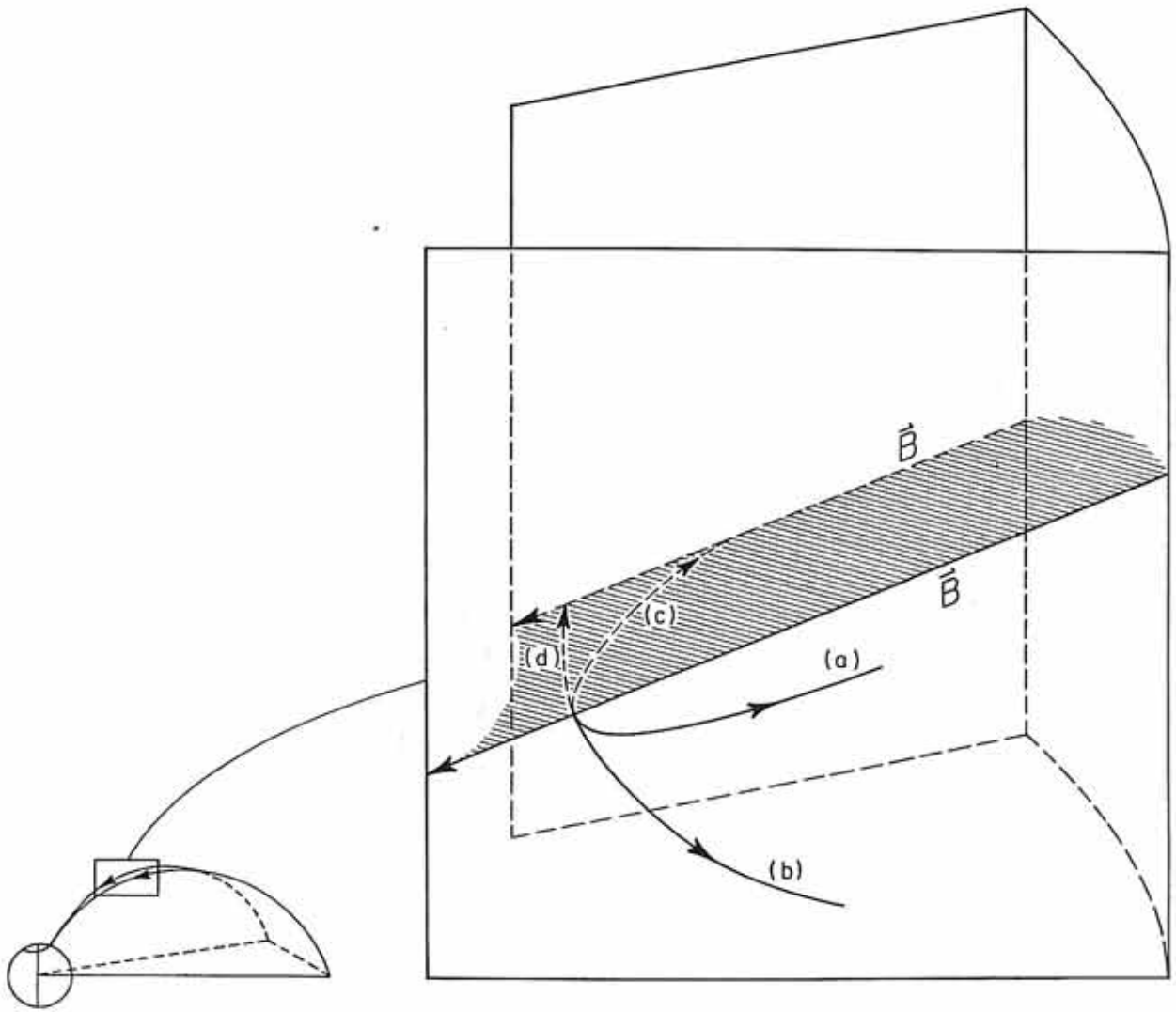

Figure 16 Variations of θ as a function of path length are shown for rays #1 through #6. The total path length for each ray is 100 km. Note that rays #1 and #2 with f near $f_{R=0}$ suffer more refraction than rays #3 through #6.

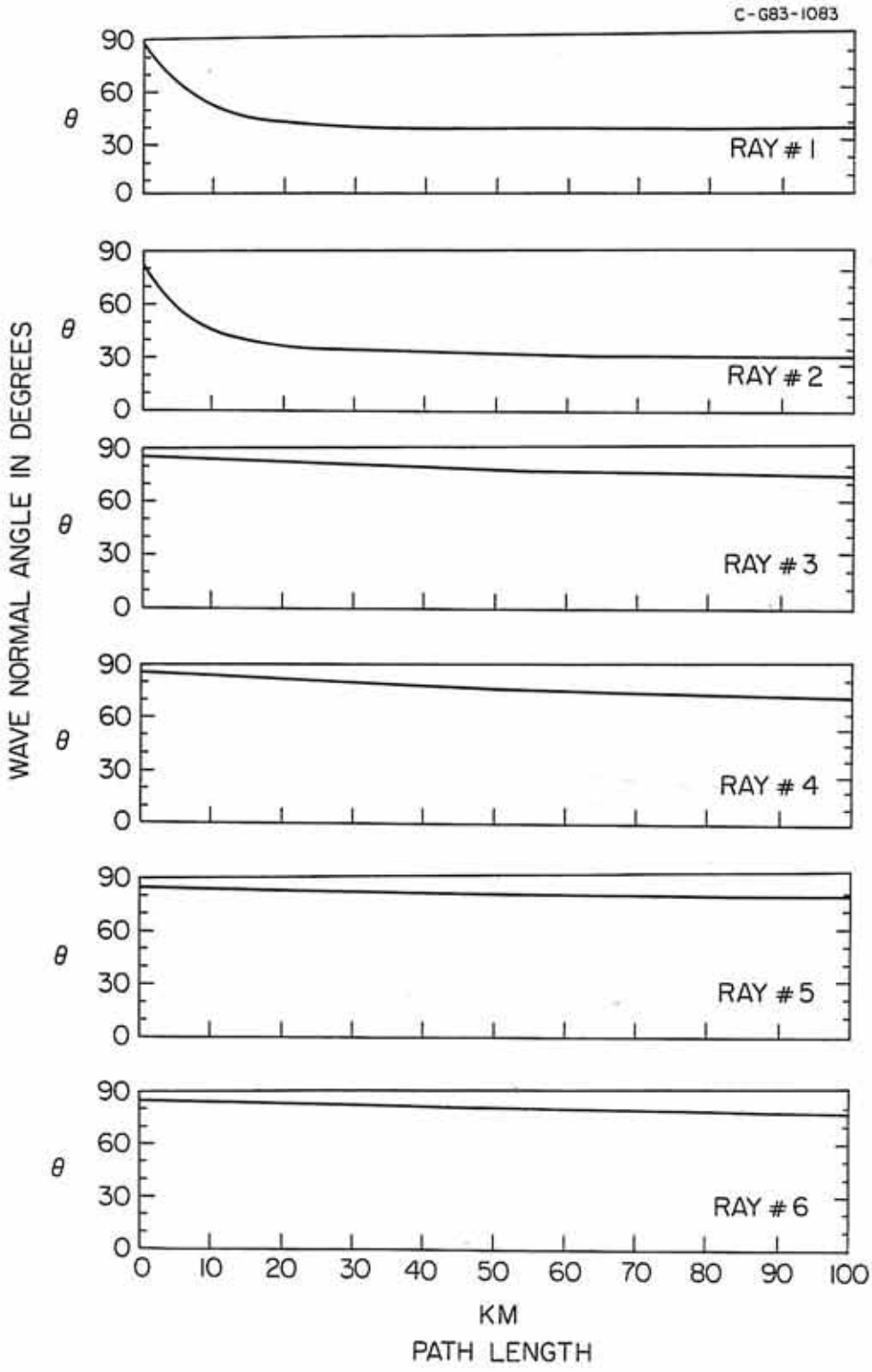
C-G83-1083
WAVE NORMAL ANGLE IN DEGREES
θ
90
60
30
0
RAY # 1
RAY # 2
RAY # 3
RAY # 4
RAY # 5
RAY # 6
0
10
20
30
40
50
60
70
80
90
100
KM
PATH LENGTH

Figure 17 Variations of magnetic latitude and longitude of rays #1 through #6 are shown. The total path length for each ray is 400 km. All rays are started at the magnetic latitude of 70° and longitude of 0°.

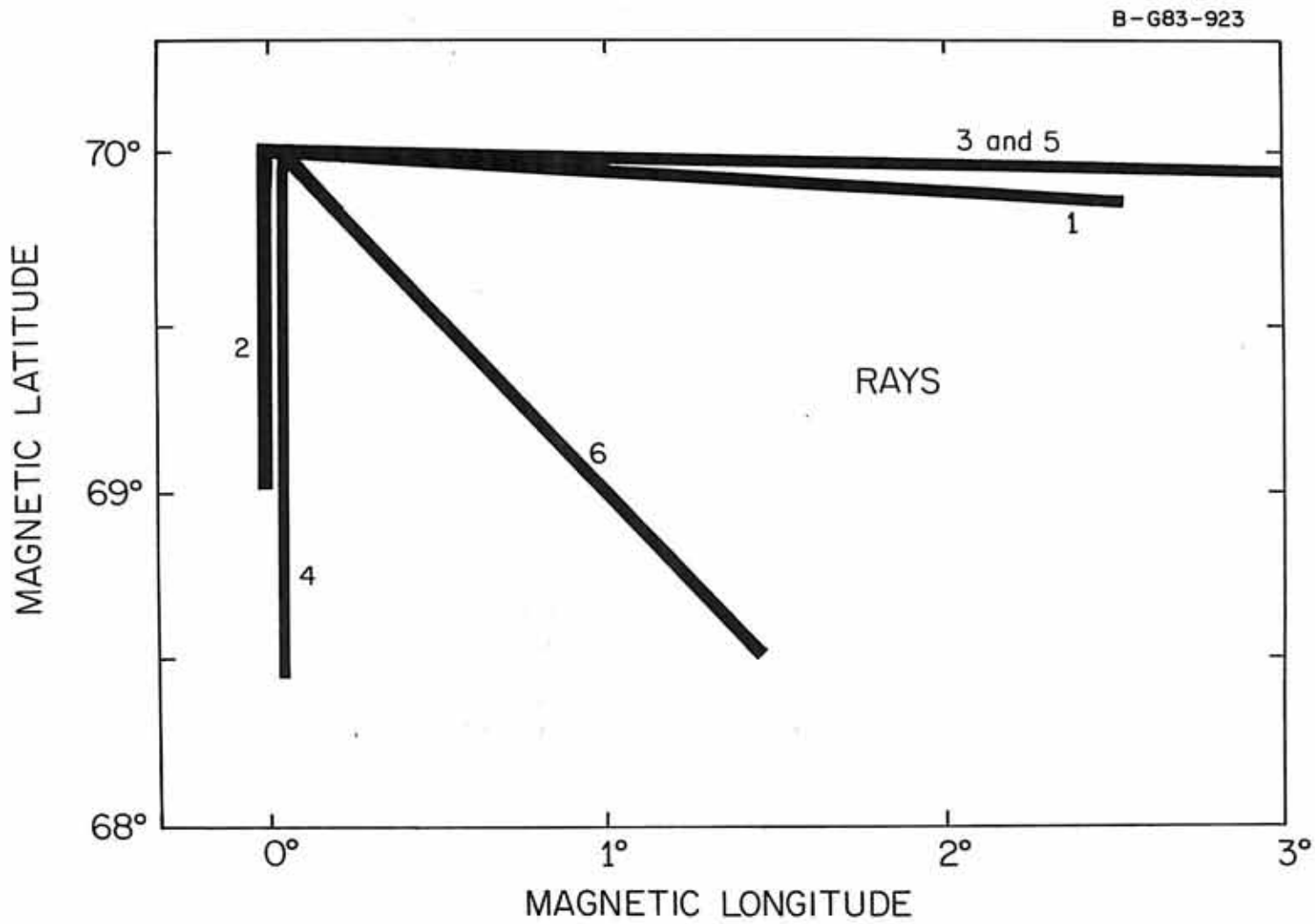
B-G83-923
70°
69°
68°
MAGNETIC LATITUDE
0°
1°
2°
3°
MAGNETIC LONGITUDE
3 and 5
1
2
4
6
RAYS

Figure 18 The number of e-foldings that the wave electric field grows or damps by (g), as a function of path length (L) for run #1.

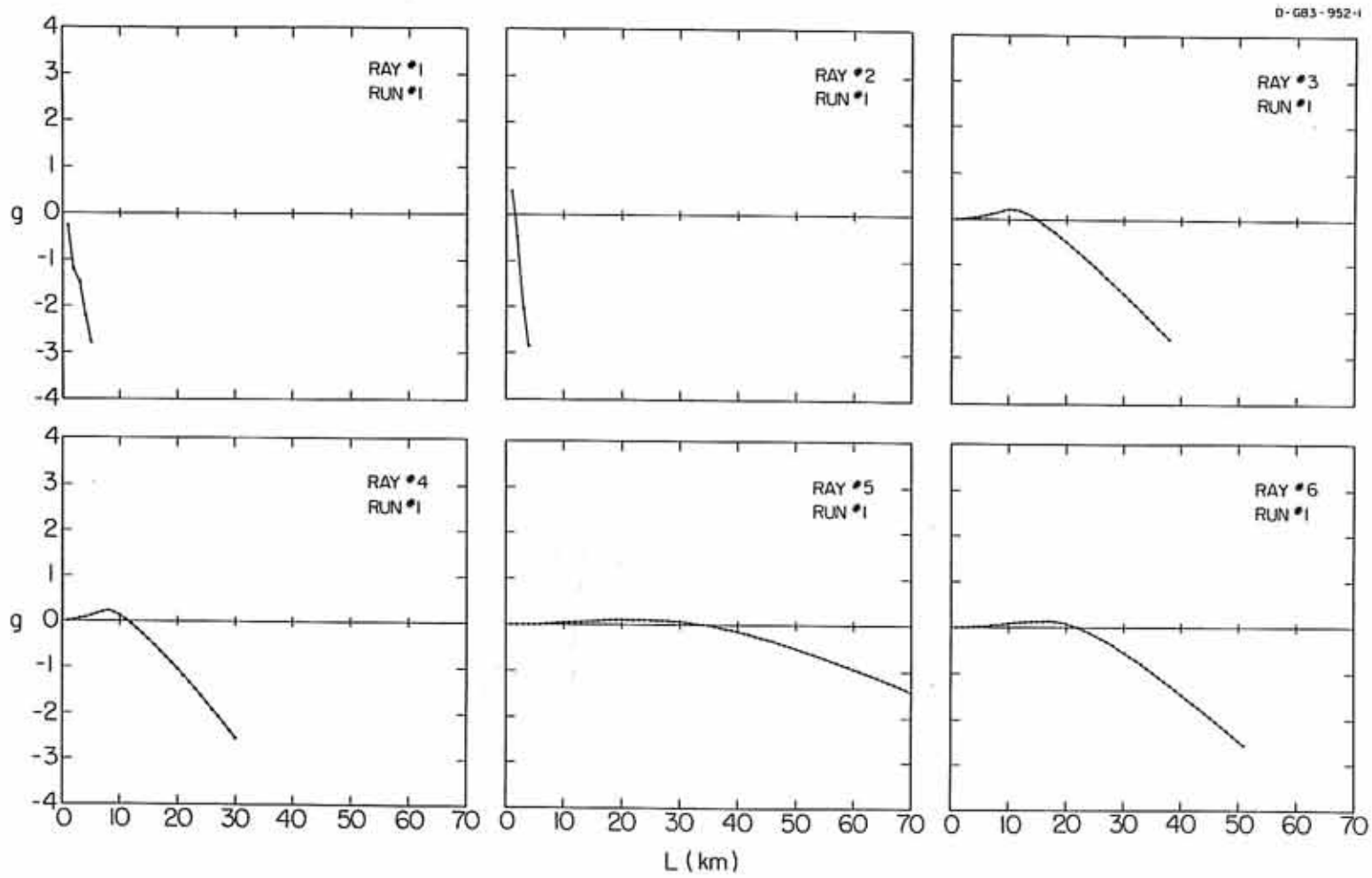
D-G83-952-1
RAY #1
RUN #1
RAY #2
RUN #1
RAY #3
RUN #1
RAY #4
RUN #1
RAY #5
RUN #1
RAY #6
RUN #1
g
4
3
2
1
0
-1
-2
-3
-4
0
10
20
30
40
50
60
70
L (km)

Figure 19 The electron distribution function measured by the S3-3 satellite and the loss cone boundary are shown. This distribution was used in run #1. In runs #2 and #3, the region below the loss cone boundary was assumed to be empty.

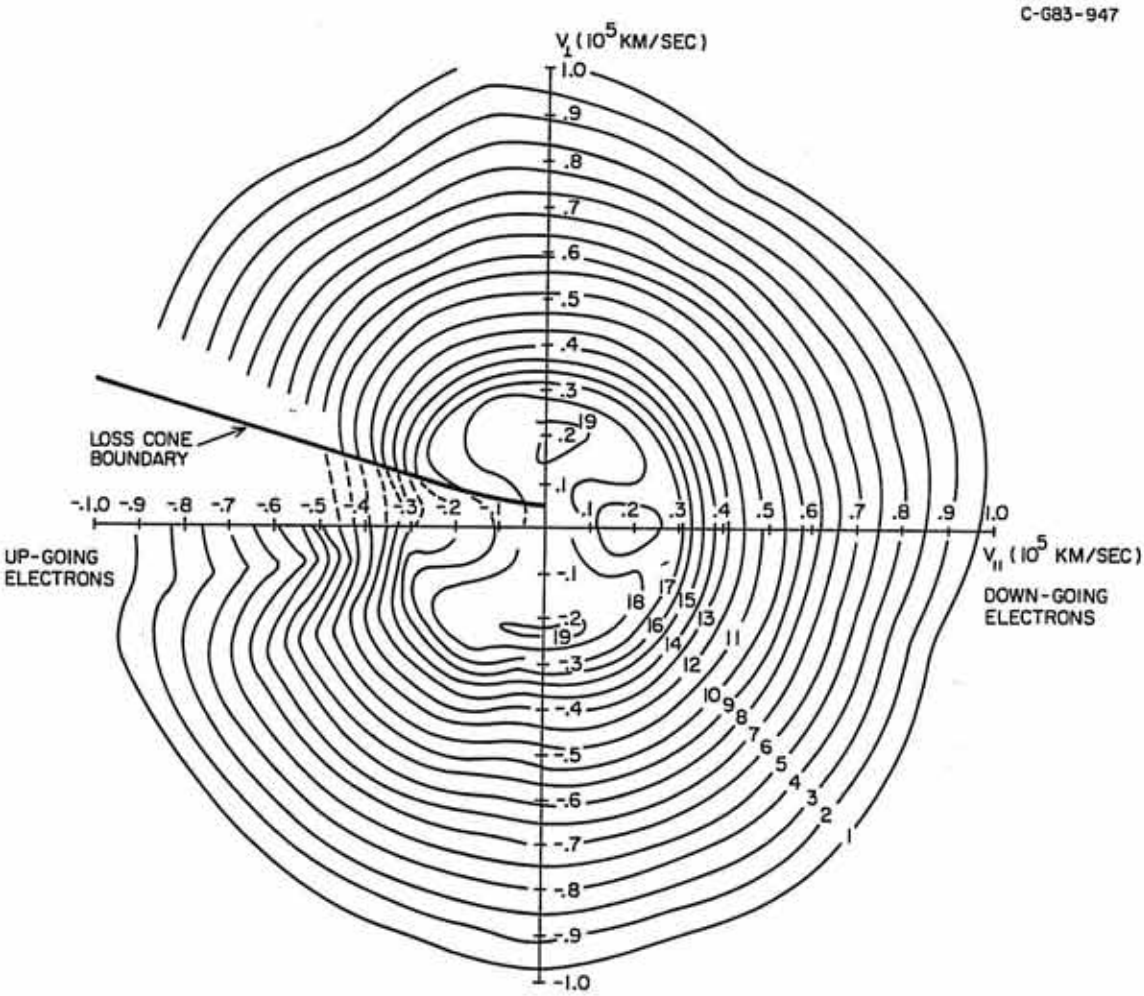
C-G83-947
$V_\perp$ (10^5 KM/SEC)
1.0
.9
.8
.7
.6
.5
.4
.3
.2
.1
-.1
-.2
-.3
-.4
-.5
-.6
-.7
-.8
-.9
-1.0
LOSS CONE BOUNDARY
-1.0 -.9 -.8 -.7 -.6 -.5 -.4 -.3 -.2 -.1 .1 .2 .3 .4 .5 .6 .7 .8 .9 1.0
$V_\parallel$ (10^5 KM/SEC)
UP-GOING ELECTRONS
DOWN-GOING ELECTRONS
19
18
17
16
15
14
13
12
11
10
9
8
7
6
5
4
3
2
1

Figure 20 Electron mean free path plotted as a function of altitude. In 20a "maximal" model for the atmospheric densities are used, whereas in 20b "minimal" model is utilized. . . . . .

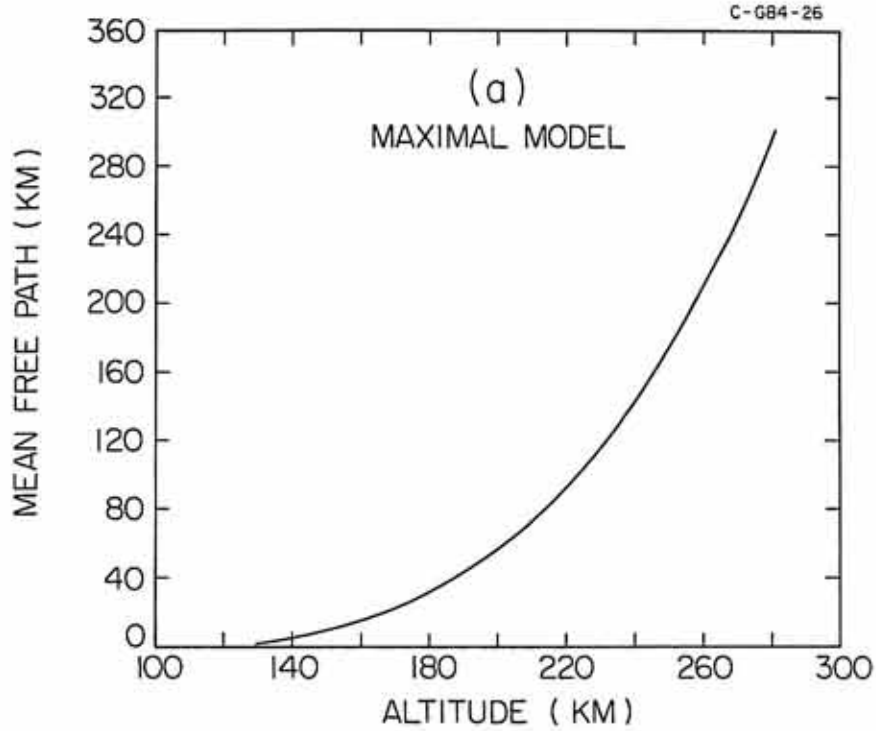
C-G84-26
(a)
MAXIMAL MODEL
MEAN FREE PATH (KM)
360
320
280
240
200
160
120
80
40
0
100
140
180
220
260
300
ALTITUDE (KM)

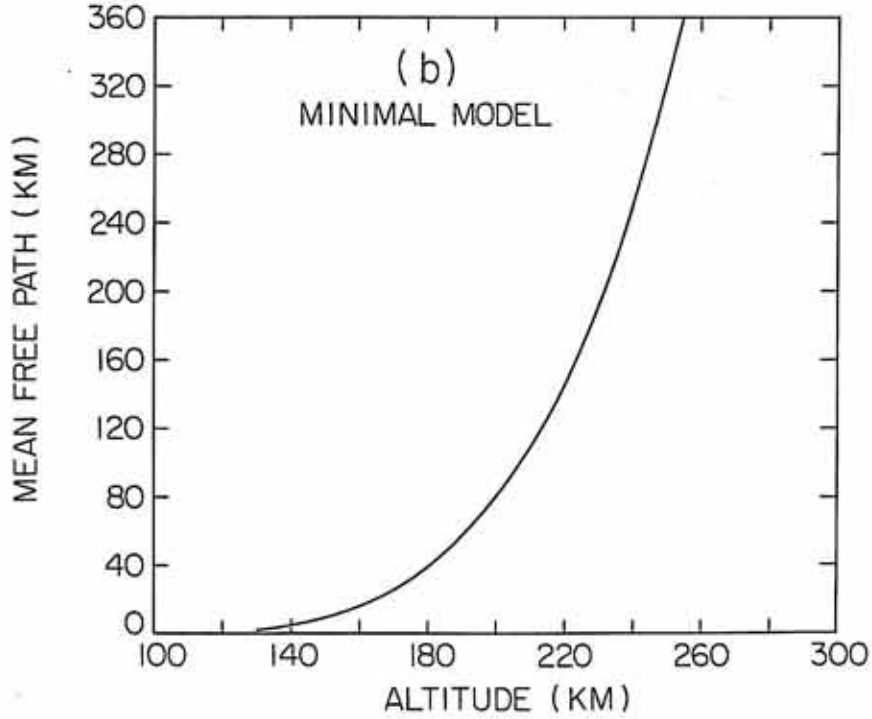
(b)
MINIMAL MODEL
MEAN FREE PATH (KM)
360
320
280
240
200
160
120
80
40
0
100
140
180
220
260
300
ALTITUDE (KM)

Figure 21 Growth rates of AKR with M_2 at 3 km below the mirroring point M_1 (run #2).

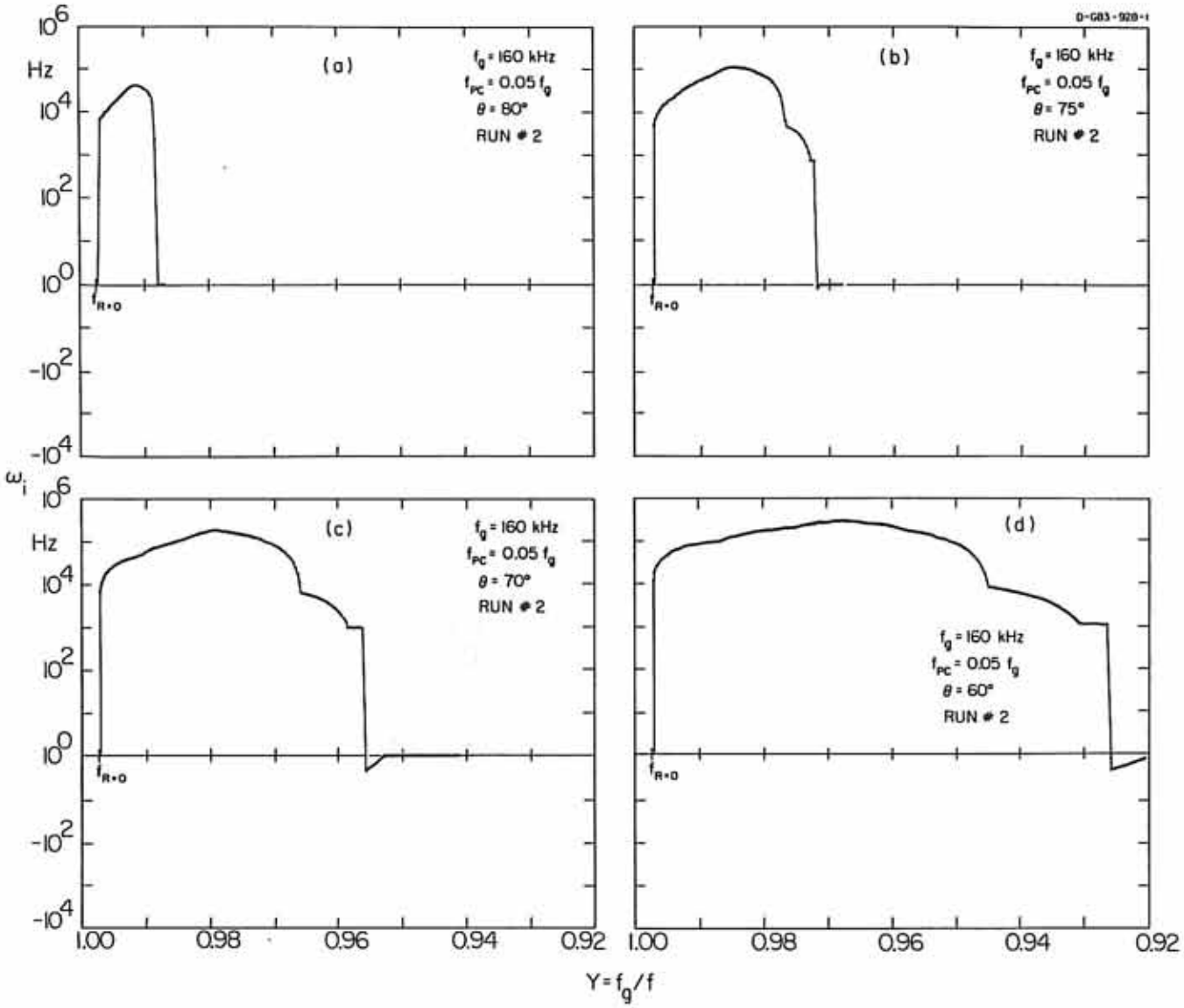
D-G83-928-1
(a)
f_g = 160 kHz
f_{PC} = 0.05 f_g
θ = 80°
RUN # 2
(b)
f_g = 160 kHz
f_{PC} = 0.05 f_g
θ = 75°
RUN # 2
(c)
f_g = 160 kHz
f_{PC} = 0.05 f_g
θ = 70°
RUN # 2
(d)
f_g = 160 kHz
f_{PC} = 0.05 f_g
θ = 60°
RUN # 2
ω_i
Hz
10^6
10^4
10^2
10^0
-10^2
-10^4
$f_{R=0}$
1.00
0.98
0.96
0.94
0.92
$Y = f_g/f$

Figure 22 The number of e-foldings that the wave electric field grows by (g), as a function of path length (L) for run #2.

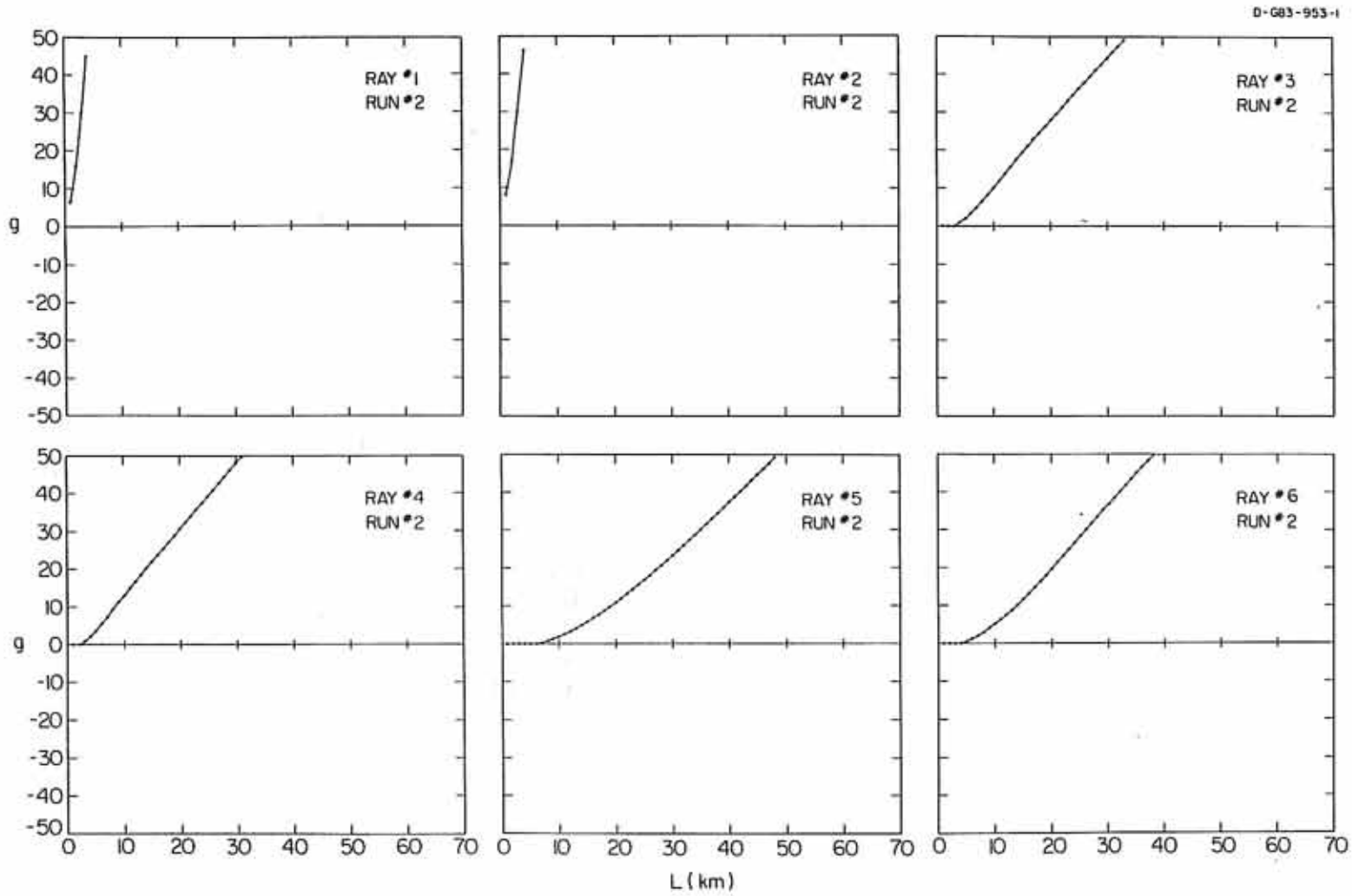
D-G83-953-1
RAY #1
RUN #2
RAY #2
RUN #2
RAY #3
RUN #2
RAY #4
RUN #2
RAY #5
RUN #2
RAY #6
RUN #2
g
50
40
30
20
10
0
-10
-20
-30
-40
-50
0
10
20
30
40
50
60
70
L (km)

Figure 23 Growth rates of AKR with M_2 at 70 km below M_1 (run #3) for θ between 80° and 60°.

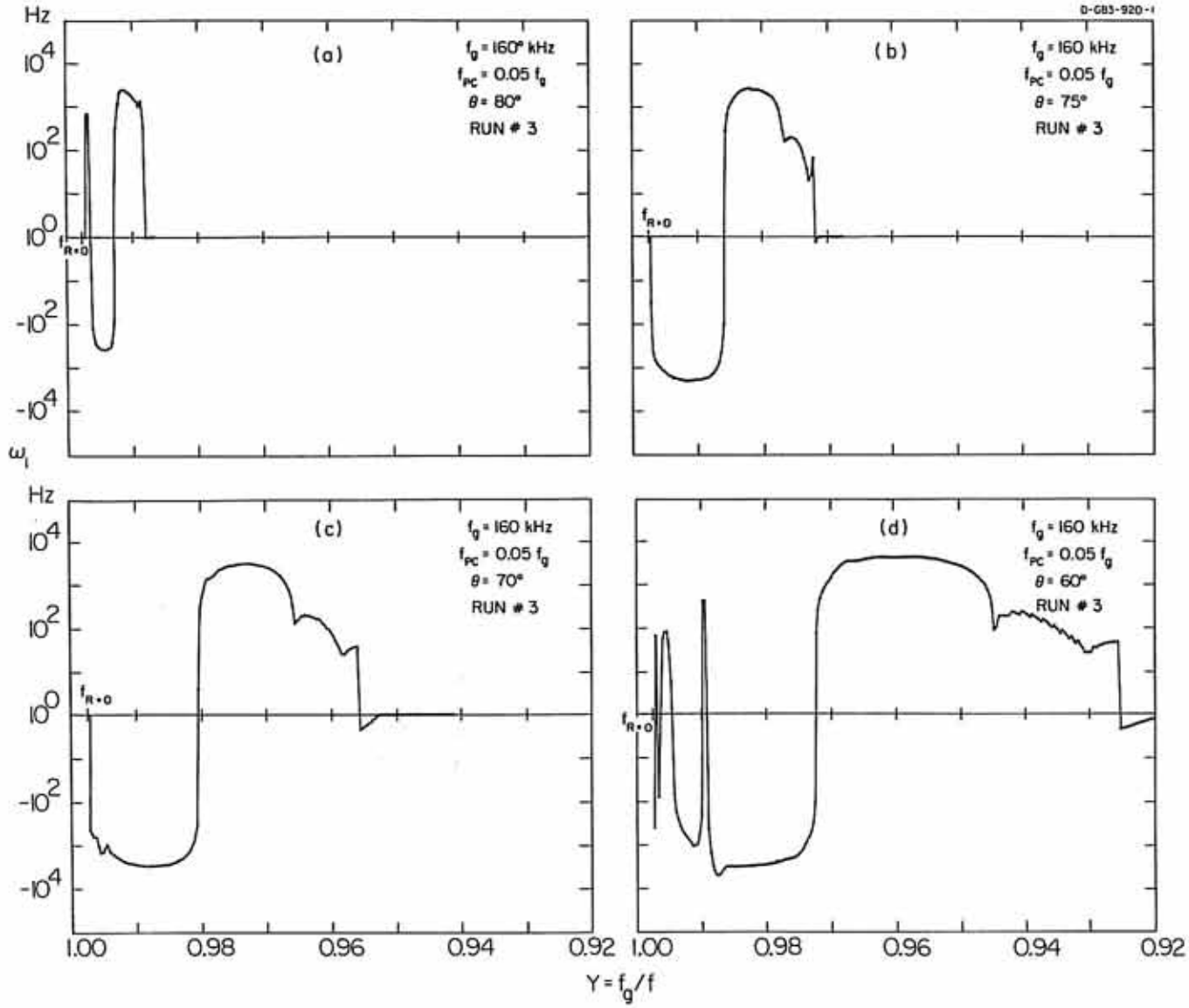
Hz
10^4
10^2
10^0
-10^2
-10^4
ω_i
(a)
f_g = 160* kHz
f_{PC} = 0.05 f_g
θ = 80°
RUN # 3
$f_{R\cdot O}$
(b)
f_g = 160 kHz
f_{PC} = 0.05 f_g
θ = 75°
RUN # 3
(c)
f_g = 160 kHz
f_{PC} = 0.05 f_g
θ = 70°
RUN # 3
(d)
f_g = 160 kHz
f_{PC} = 0.05 f_g
θ = 60°
RUN # 3
1.00
0.98
0.96
0.94
0.92
$Y = f_g/f$

Figure 24 Growth rates of AKR with M_2 at 70 km below M_1 (run #3) for θ between 55° and 35°.

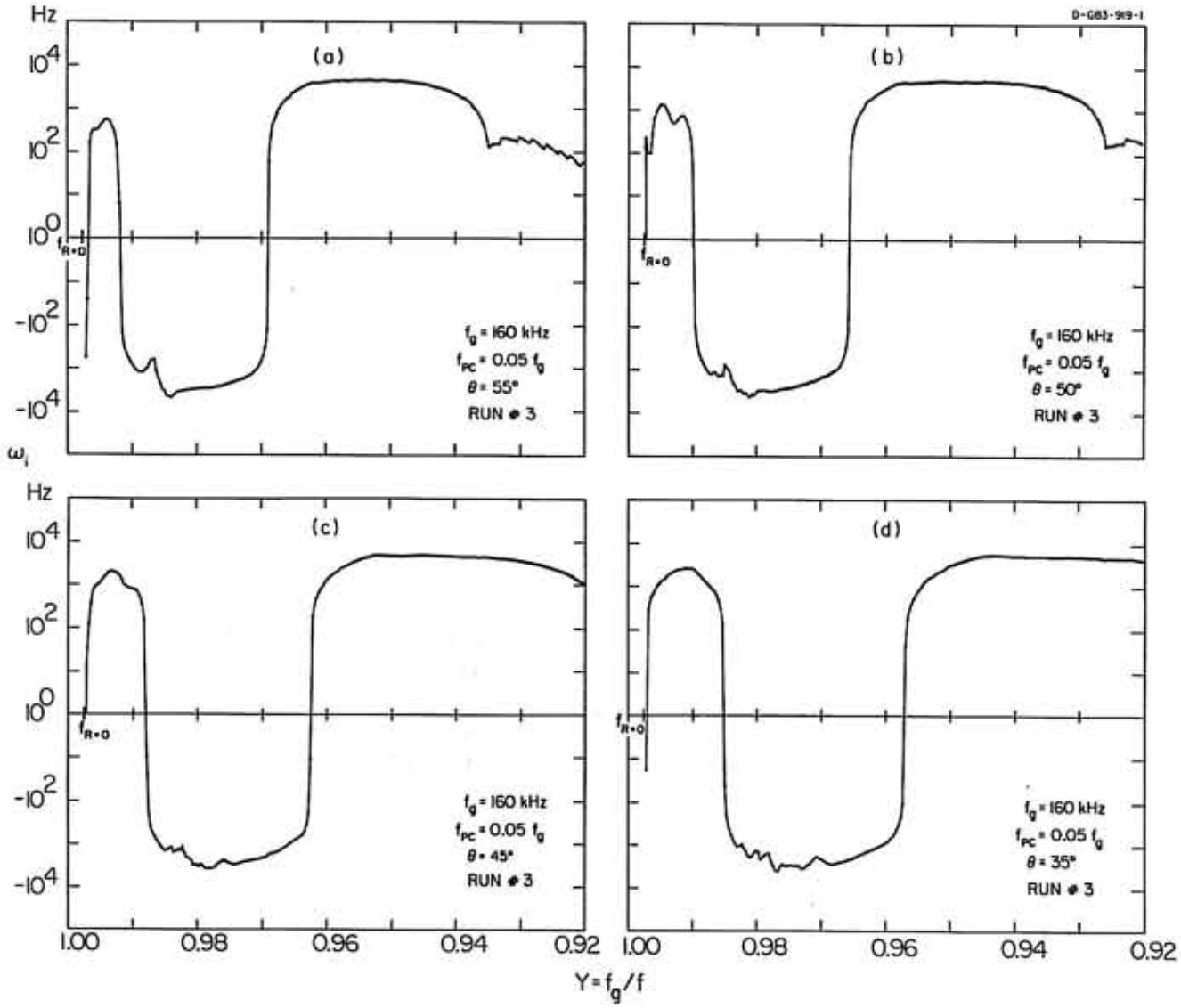
D-G83-919-1
Hz
10^4
10^2
10^0
-10^2
-10^4
ω_i
(a)
$f_{R=0}$
f_g = 160 kHz
f_{PC} = 0.05 f_g
θ = 55°
RUN # 3
(b)
$f_{R=0}$
f_g = 160 kHz
f_{PC} = 0.05 f_g
θ = 50°
RUN # 3
(c)
$f_{R=0}$
f_g = 160 kHz
f_{PC} = 0.05 f_g
θ = 45°
RUN # 3
(d)
$f_{R=0}$
f_g = 160 kHz
f_{PC} = 0.05 f_g
θ = 35°
RUN # 3
1.00
0.98
0.96
0.94
0.92
$Y = f_g/f$

Figure 25 The number of e-foldings that the wave electric field grows or damps by (g), as a function of path length (L) for run #3.

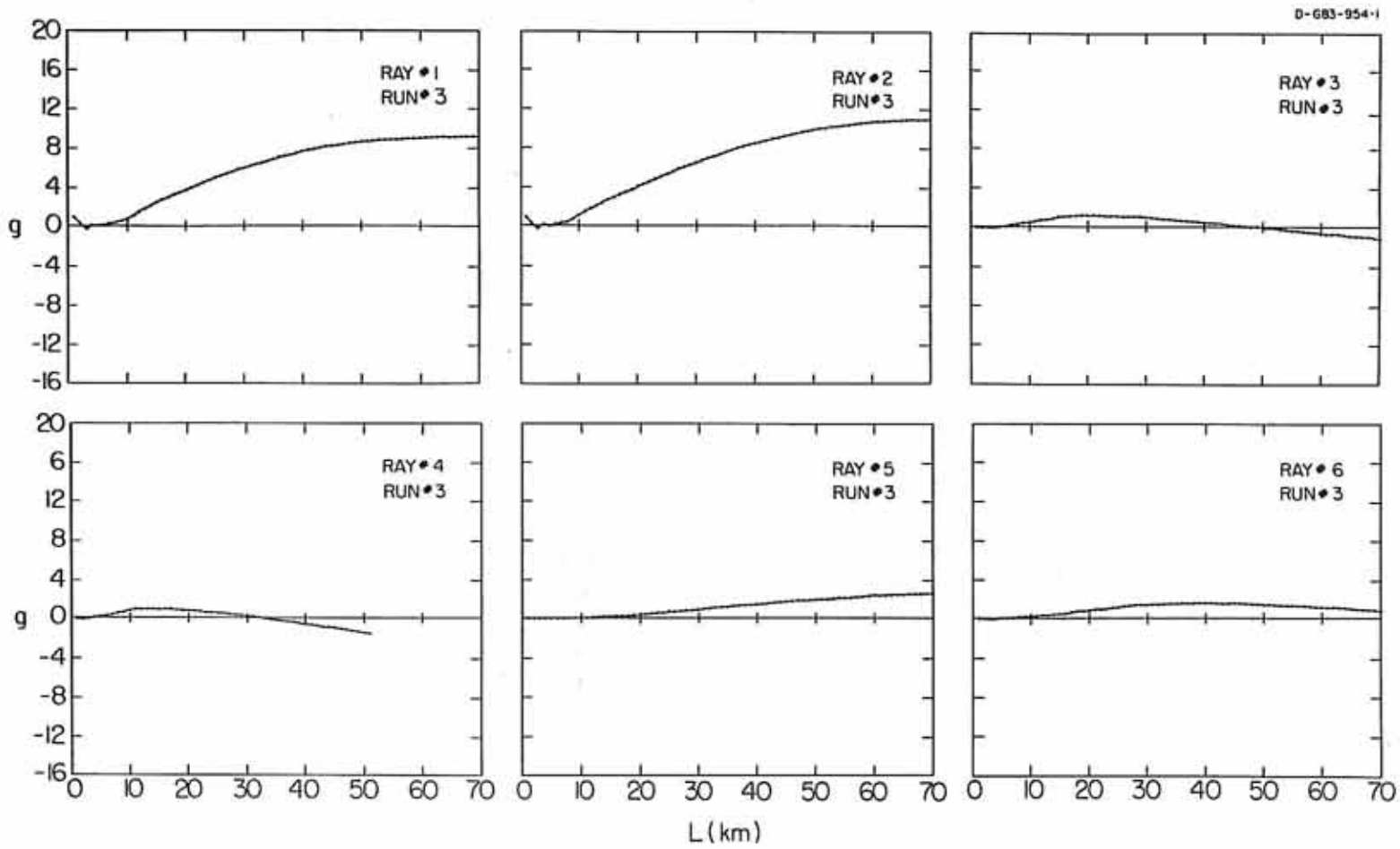
D-683-954-1
RAY # 1
RUN # 3
RAY # 2
RUN # 3
RAY # 3
RUN # 3
RAY # 4
RUN # 3
RAY # 5
RUN # 3
RAY # 6
RUN # 3
g
L (km)

Figure 26 An electric field spectral density corresponding to UT 5:44 on day 309 of 1981. The plasma frequency is determined from the upper cutoff of the auroral hiss which propagates in the whistler mode. Note that the upper cutoff of the Z-mode radiation is just below the electron gyrofrequency.

C-G83-371

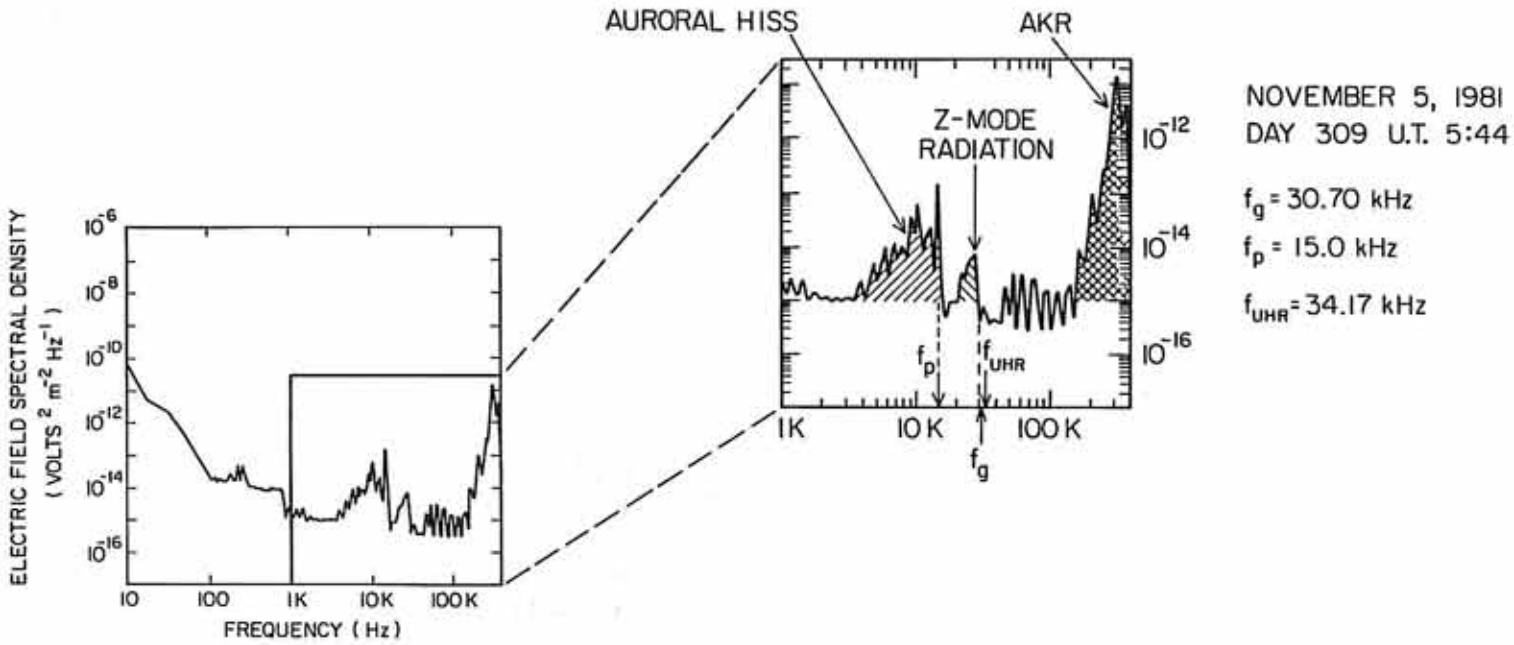

NOVEMBER 5, 1981
DAY 309 U.T. 5:44

f_g = 30.70 kHz

f_p = 15.0 kHz

f_{UHR} = 34.17 kHz

Figure 27 Three resonance circles for Z-mode corresponding to $\theta = 90°$; $Y = 1.001$ (A), $Y = 1.0023$ (B), and $Y = 1.0035$ (C) are superimposed on the electron distribution function.

C-G83-107

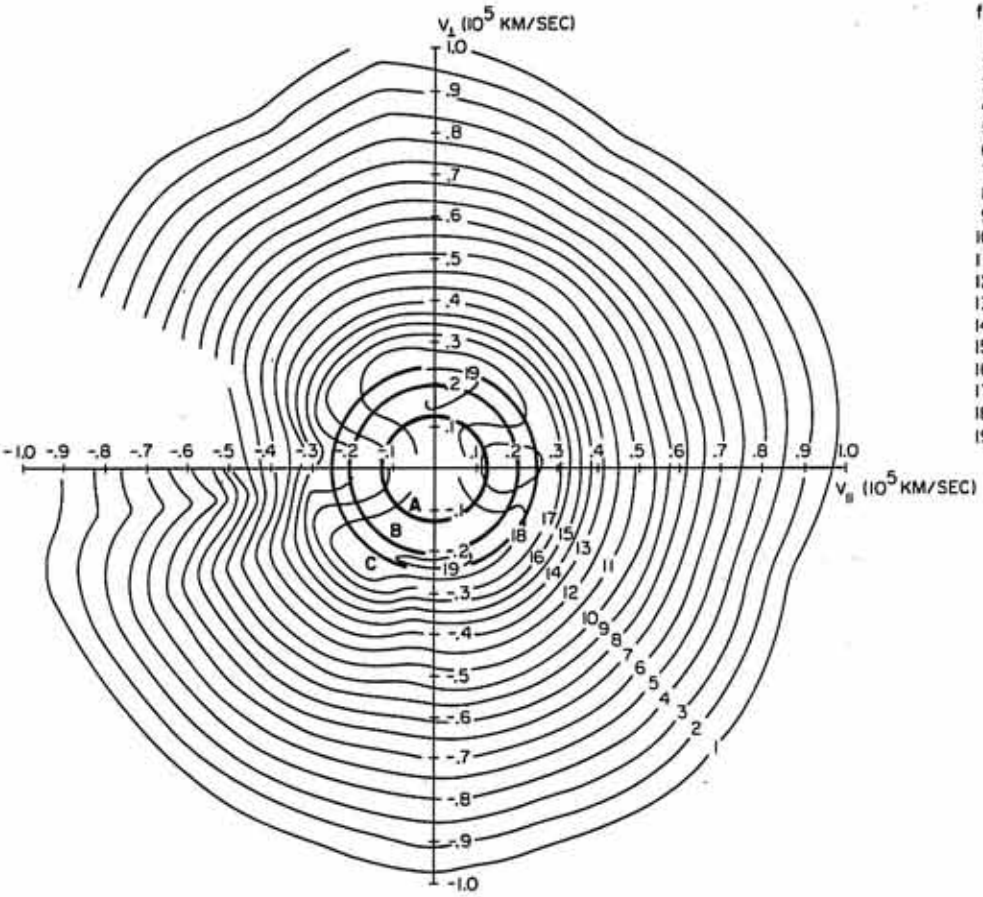

	f(v) [SEC^3/KM^6]
1	.100E-04
2	.215E-04
3	.464E-04
4	.100E-03
5	.215E-03
6	.464E-03
7	.100E-02
8	.215E-02
9	.464E-02
10	.100E-01
11	.215E-01
12	.464E-01
13	.100E+00
14	.215E+00
15	.464E+00
16	.100E+01
17	.215E+01
18	.464E+01
19	.100E+02

Figure 28 Growth rates of Z-mode radiation for perpendicular propagation of waves with frequencies just below the gyrofrequency. As the cold plasma density increases ω_i decreases.

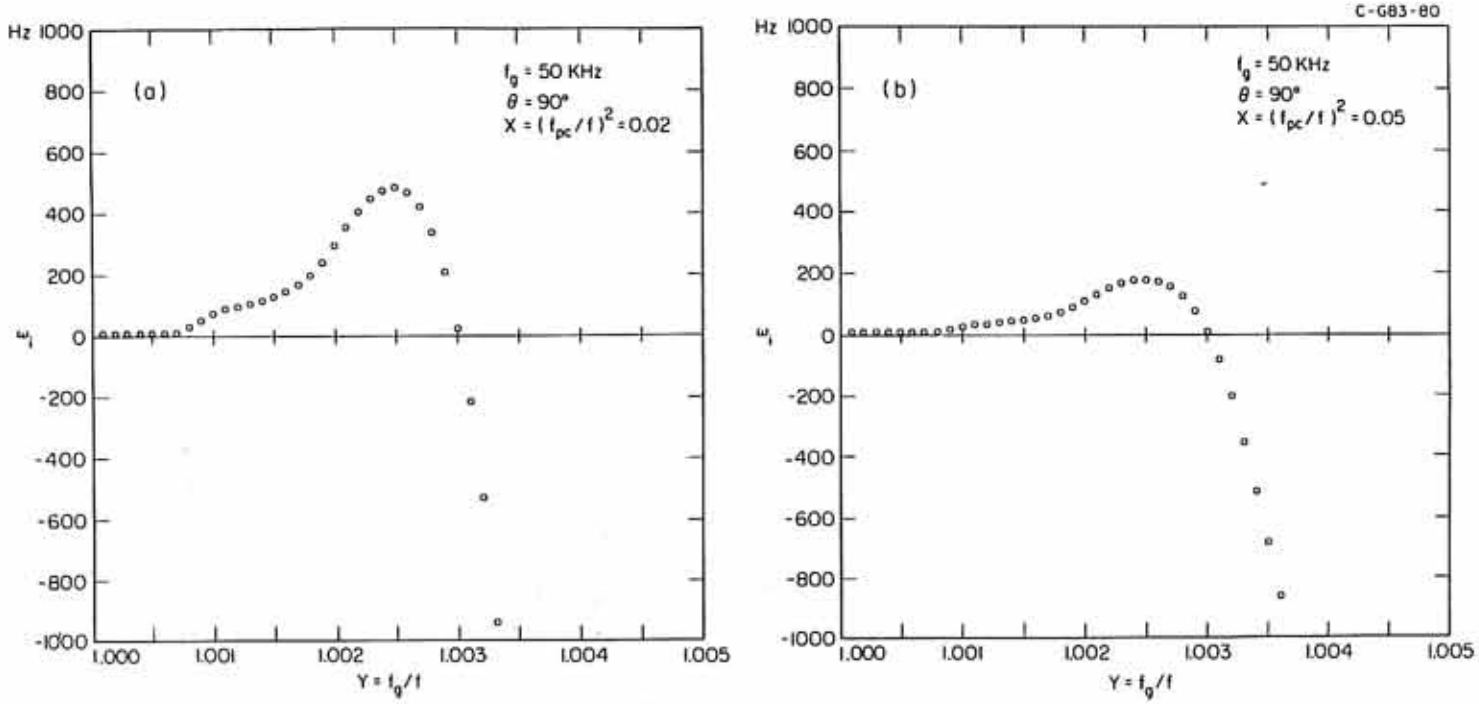
C-683-80
Hz 1000
800
600
400
200
0
-200
-400
-600
-800
-1000
ω_i
(a)
f_g = 50 KHz
θ = 90°
$X = (f_{pc}/f)^2 = 0.02$
1.000
1.001
1.002
1.003
1.004
1.005
$Y = f_g/f$
(b)
f_g = 50 KHz
θ = 90°
$X = (f_{pc}/f)^2 = 0.05$

Figure 29 Growth rates of Z-mode radiation for $\theta = 85°$. Clearly there is no significant difference between waves propagating upward (a) and those travelling downwards (b). Except for a small growth for $Y < 1.005$ all waves are damped.

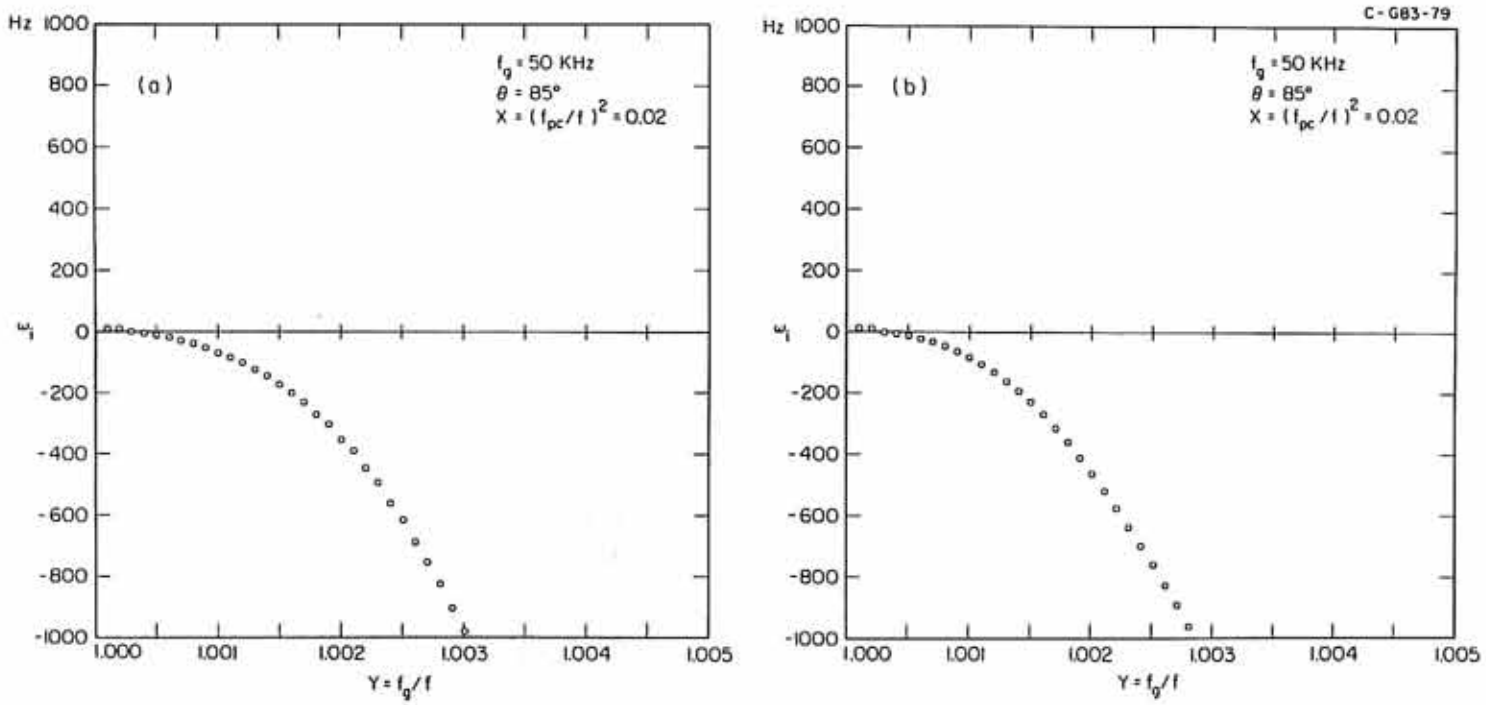
C-G83-79
Hz
1000
800
600
400
200
0
-200
-400
-600
-800
-1000
ω_i
(a)
(b)
f_g = 50 KHz
θ = 85°
$X = (f_{pc}/f)^2 = 0.02$
1.000
1.001
1.002
1.003
1.004
1.005
$Y = f_g/f$

Figure 30 Three resonance ellipses corresponding to downgoing Z-mode with $\theta = 85°$, $Y = 1.0005$ (A), $Y = 1.001$ (B) and $Y = 1.003$ (C) are superimposed on the electron distribution function.

C-G83-106

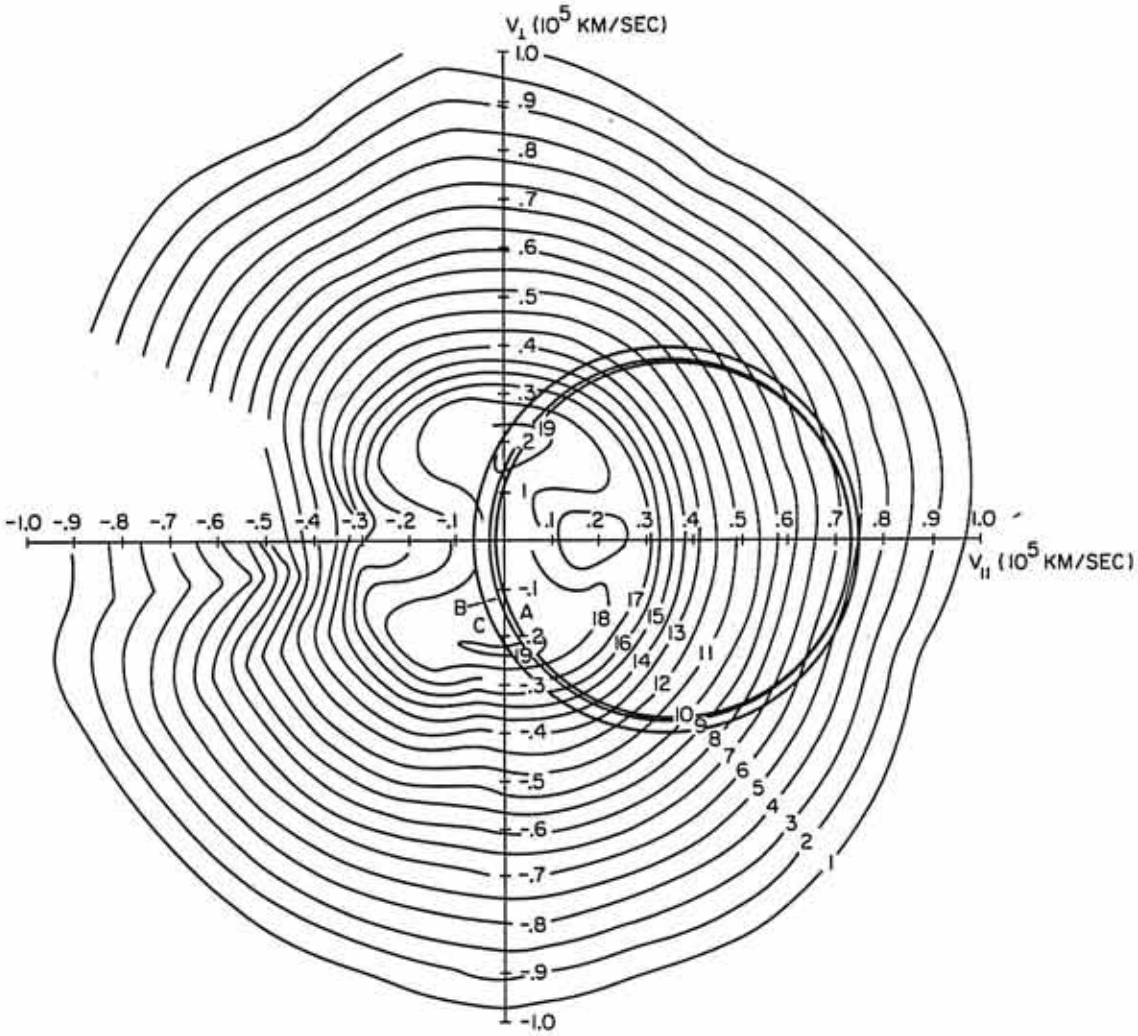

Figure 31 The path lengths required to amplify the background blackbody radiation up to the maximum observed intensities of the Z-mode radiation using the growth rates in Figure 28.

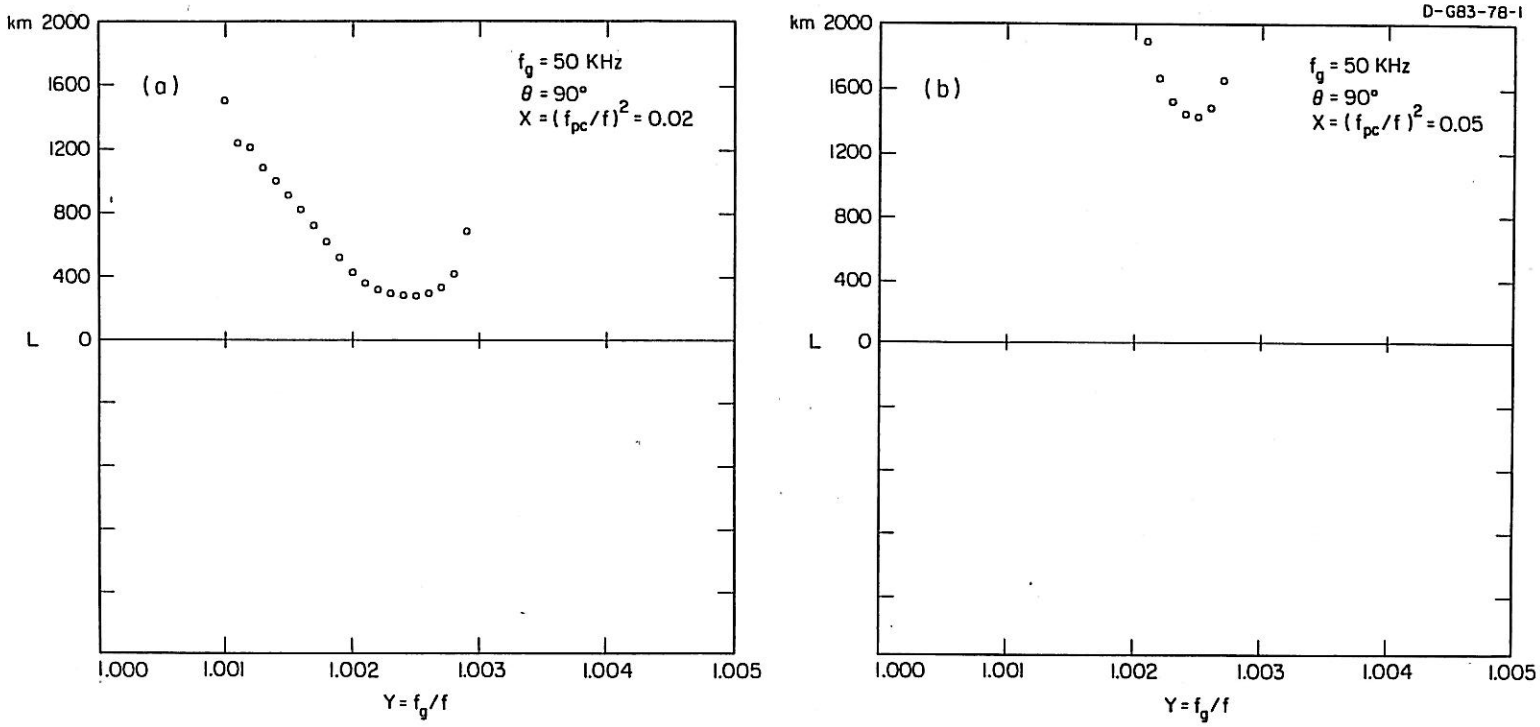
D-G83-78-1
km 2000
1600
1200
800
400
L 0
(a)
f_g = 50 KHz
θ = 90°
$X = (f_{pc}/f)^2 = 0.02$
1.000
1.001
1.002
1.003
1.004
1.005
$Y = f_g/f$
(b)
f_g = 50 KHz
θ = 90°
$X = (f_{pc}/f)^2 = 0.05$

APPENDIX

EXPRESSION FOR THE GROWTH RATE

In this section, an expression for calculating the growth rates of AKR and Z-mode radiation is given, and an approximate equation for ω_i, similar to that given by Wu and Lee [1979] but in a more accurate form is derived. The general form of the dispersion equation is:

$$\Lambda = \text{determinant of } \underset{\sim}{\Lambda} = 0 \tag{A1}$$

where

$$\underset{\sim}{\Lambda}_{ij} = N^2\left(\frac{k_i k_j}{k^2} - \delta_{ij}\right) + \varepsilon_{ij}(\vec{k},\omega) \tag{A2}$$

with the dielectric tensor defined as $\varepsilon_{ij}(\vec{k},\omega) \equiv \delta_{ij} + Q_{ij}(\vec{k},\omega)$. The general form of $Q_{ij}(\vec{k},\omega)$ is given in Baldwin et al. [1969] and Lee and Wu [1980]. In the following we ignore the thermal effect of the higher-energy electrons on the function $\Lambda(\vec{k},\omega)$ so that it can be written as:

$$\Lambda = \begin{vmatrix} 1 - \frac{c^2 k_\parallel^2}{\omega^2} - \frac{\omega_{pc}^2}{\omega^2 - \omega_g^2} + i\phi & \frac{i\,\omega_{pc}^2\,\omega_g}{\omega(\omega^2 - \omega_g^2)} + \phi & \frac{c^2 k_\parallel k_\perp}{\omega^2} - i\psi \\ -i\,\frac{\omega_{pc}^2\,\omega_g}{\omega(\omega^2 - \omega_g^2)} - \phi & 1 - \frac{c^2 k^2}{\omega^2} - \frac{\omega_{pc}^2}{\omega^2 - \omega_g^2} + i\phi & \psi \\ \frac{c^2 k_\parallel k_\perp}{\omega^2} - i\psi & -\psi & 1 - \frac{c^2 k_\perp^2}{\omega^2} - \frac{\omega_{pc}^2}{\omega^2} \end{vmatrix} = 0 \tag{A3}$$

where the imaginary part of Q_{zz} has been set equal to zero; $k_\parallel$ and $k_\perp$ are the components of $\vec{k}$ parallel and perpendicular to the magnetic field, respectively, and

$$\phi = -2\pi^2 \frac{\omega_{PH}^2}{\omega} \int_{-\infty}^{\infty} du_\parallel \int_0^{\infty} du_\perp \left[\frac{\partial}{\partial u_\perp} + \frac{k_\parallel}{\gamma\omega}\left(u_\perp \frac{\partial}{\partial u_\parallel} - u_\parallel \frac{\partial}{\partial u_\perp}\right)\right] F_e \frac{u_\perp^2}{4} \delta(\gamma\omega - \omega_g - k_\parallel u_\parallel)$$

$$\psi = +2\pi^2 \frac{\omega_{PH}^2}{\omega} \int_{-\infty}^{\infty} du_\parallel \int_0^{\infty} du_\perp \left[\frac{\partial}{\partial u_\perp} + \frac{k_\parallel}{\gamma\omega}\left(u_\perp \frac{\partial}{\partial u_\parallel} - u_\parallel \frac{\partial}{\partial u_\perp}\right)\right] F_e \frac{k_\perp u_\perp^2 u_\parallel}{4\omega_g} \delta(\gamma\omega - \omega_g - k_\parallel u_\parallel) \tag{A4}$$

with F_e being the unperturbed distribution of electrons normalized to unity; ω_{pc} and ω_{PH} being the angular plasma frequency of the cold and warm electrons, respectively; $u_\parallel$ and $u_\perp$ being electron momentum per unit mass parallel and perpendicular to the magnetic field; and $\gamma \equiv (1 + u^2/c^2)^{1/2}$.

Equation (A3) consists of a real part and an imaginary part. The real part of Equation (A3) will give the relation between ω (real part of frequency) and $\vec{k}$ and since thermal effects were ignored in obtaining

$\mathrm{Re}\{\Lambda(\vec{k},\omega)\}$, the resulting index of refraction is the same as that in a cold plasma discussed by Stix [1962]. The expression for the growth rate ω_i is then given by

$$\frac{\omega_i}{\omega} = -\frac{\mathrm{Im}(\Lambda)}{\omega \frac{\partial}{\partial\omega} \mathrm{Re}(\Lambda)} \tag{A5}$$

where the imaginary part of Λ is

$$\mathrm{Im}(\Lambda) = \eta\phi + \rho\psi \tag{A6}$$

with η and ρ defined as

$$\eta \equiv [2 - \frac{c^2}{\omega^2}(k^2 + k_\parallel^2) - \frac{2\omega_{pc}^2}{\omega(\omega + \omega_g)}](1 - \frac{c^2 k_\perp^2}{\omega^2} - \frac{\omega_{pc}^2}{\omega^2}) - c^4 \frac{k_\parallel^2 k_\perp^2}{\omega^4}$$

$$\rho \equiv 2\frac{c^2 k_\parallel k_\perp}{\omega^2}(1 - \frac{c^2 k^2}{\omega^2} - \frac{\omega_{pc}^2}{\omega(\omega + \omega_g)}) \quad . \tag{A7}$$

The term in the denominator of Equation (A5) can be expressed as

$$\begin{aligned}\omega \frac{\partial}{\partial\omega} \mathrm{Re}(\Lambda) = {} & 2N^4[\frac{\omega^2\omega_{pc}^2 \mathrm{Sin}^2\theta}{(\omega^2 - \omega_g^2)^2} + \frac{\omega_{pc}^2 \mathrm{Cos}^2\theta}{\omega^2}] + 4N^2[\frac{\omega_{pc}^2(\omega_{pc}^2 - \omega_g^2)}{(\omega^2 - \omega_g^2)^2} \\ & - 1 - \frac{\omega_{pc}^2\omega_g^2 \mathrm{Sin}^2\theta}{2(\omega^2 - \omega_g^2)^2}] + 2[(2 - \frac{\omega_{pc}^2}{\omega^2})(1 - \frac{\omega_{pc}^2}{\omega^2 - \omega_g^2})^2 \\ & - \frac{\omega_{pc}^4\omega_g^2}{\omega^2(\omega^2 - \omega_g^2)^2} + 2(1 - \frac{\omega_{pc}^2}{\omega^2})^2 \frac{\omega^2\omega_{pc}^2}{(\omega^2 - \omega_g^2)^2}] \quad .\end{aligned} \tag{A8}$$

Although it was numerically shown by Lee and Wu [1980] that in comparison with the results of Wu and Lee [1979], smaller growth rates are obtained when the effects of cold electrons are included in the dispersion relation, it is instructive to see how Equation (A5) can be reduced to the expression for ω_i given in Wu and Lee [1979]. In order to do this, it is necessary to transform ϕ and ψ from momentum space into velocity space. Upon this transformation ϕ and ψ are given by

$$\phi = -\frac{\pi^2}{2}\frac{\omega_{PH}^2}{\omega^2}\int_{-\infty}^{\infty} dv_\parallel \int_0^\infty dv_\perp v_\perp^2 [\omega_g \frac{\partial F_e}{\partial v_\perp} + k_\parallel v_\perp \frac{\partial F_e}{\partial v_\parallel}]\,\delta(\omega - \frac{\omega_g}{\gamma_v} - k_\parallel v_\parallel)$$

$$\psi = \frac{\pi^2}{2}\frac{\omega_{PH}^2}{\omega^2}\int_{-\infty}^{\infty} dv_\parallel \int_0^\infty dv_\perp \frac{k_\perp v_\parallel v_\perp^2}{\omega_g}[\omega_g \frac{\partial F_e}{\partial v_\perp} + k_\parallel v_\perp \frac{\partial F_e}{\partial v_\parallel}]\,\delta(\omega - \frac{\omega_g}{\gamma_v} - k_\parallel v_\parallel) \tag{A9}$$

where $\gamma_v \equiv (1 - v^2/c^2)^{-1/2}$ has been set equal to one everywhere except in the delta function; and terms like $v_\parallel v_\perp/c^2$ and $v_\perp^2/c^2$ have been dropped. From Equation (A9) one can see that the integrand of ψ is that of ϕ times the factor $(k_\perp v_\parallel/\omega_g)$. Since in the case of R-X mode for $\omega \sim \omega_g \gg \omega_p$, η is greater than ρ, for small $v_\parallel/c$ the second term in Equation (A6) can be dropped and Equation (A5) can be rewritten as

$$\omega_i = (2\eta)[\frac{\pi^2\omega_{PH}^2}{4\omega}\int_{-\infty}^{\infty} dv_\parallel \int_0^\infty dv_\perp v_\perp^2 (\omega_g \frac{\partial F_e}{\partial v_\perp} + k_\parallel v_\perp \frac{\partial F_e}{\partial v_\parallel})\,\delta(\omega - \frac{\omega_g}{\gamma_v} - k_\parallel v_\parallel)]/(\omega\frac{\partial}{\partial\omega}\mathrm{Re}(\Lambda)) \tag{A10}$$

The expression in the bracket in the numerator is the growth rate formula given by Wu and Lee [1979]. Since η and $\omega\frac{\partial}{\partial\omega}\,\mathrm{Re}(\Lambda)$ vary from 1.1 and 150, respectively at $f \sim f_{R=0}$ to 0.16 and 1 at f much above $f_{R=0}$, it is clear that ignoring the factor $\Gamma \equiv (2\eta)/(\omega\frac{\partial}{\partial\omega}\mathrm{Re}(\Lambda))$ can result in overestimation of the growth and damping rates.

REFERENCES

Baldwin, D. E., I. B. Bernstein, and M. P. H. Weenink, Advances in Plasma Physics, Vol. 3, Wiley, New York, 1969.

Banks, P. M., C. R. Chappell, and A. F. Nagy, A new model for the interaction of auroral electrons with the atmosphere: Spectral degradation, backscatter, optical emission and ionization, J. Geophys. Res., 79, 1459-1470, 1974.

Benson, R., and W. Calvert, ISIS 1 observations at the source of auroral kilometric radiation, Geophys. Res. Lett., 6, 479, 1979.

Brown, L. W., The galactic ratio spectrum between 130 kHz and 2600 kHz, Astrophys. J., 180, 359, 1973.

Calvert, W., The Auroral plasma cavity, Geophys. Res. Lett., 8, 919, 1981.

Calvert, W., A feedback model for the source of auroral kilometric radiation, J. Geophys. Res., 87, 8199, 1982.

Chiu, Y. T., and M. Schulz, Self-consistent particle and parallel electrostatic field distributions in the magnetospheric-ionospheric auroral region, J. Geophys. Res., 83, 629, 1978.

Croley, D. R., P. F. Mizera, and J. F. Fennel, Signature of a parallel electric field in ion and electron distributions in velocity space, J. Geophys. Res., 83, 2701-2705, 1978.

Dusenbery, P. B., and L. R. Lyons, General concepts on the generation of auroral kilometric radiation, J. Geophys. Res., 87, 7467, 1982.

Gallagher, D. L., and D. A. Gurnett, Auroral kilometric radiation: Time-averaged source location, J. Geophys. Res., 84, 6501, 1979.

Green, J. L., D. A. Gurnett, and R. A. Hoffman, A correlation between auroral kilometric radiation and inverted-V electron precipitation, J. Geophys. Res., 84, 5216, 1979.

Gurnett, D. A., The earth as a radio source: Terrestrial kilometric radiation, J. Geophys. Res., 83, 689-696, 1978.

Gurnett, D. A., and J. L. Green, On the polarization and origin of auroral kilometric radiation, J. Geophys. Res., 83, 689, 1978.

Gurnett, D. A., S. D. Shawhan, and R. R. Shaw, Auroral hiss, Z-mode radiation and auroral kilometric radiation in the polar magnetosphere: DE-1 observations, J. Geophys. Res., 88, 329, 1983.

Hewitt, R. G., D. B. Melrose, and K. G. Ronnmark, The loss-cone driven electron-cyclotron maser, Aust. J. Phys., 35, 447, 1982.

Hewitt, R. G., and D. B. Melrose, Electron cyclotron maser emission near the cutoff frequencies, Aust. J. Phys., 36, 725, 1983.

Hewitt, R. G., D. B. Melrose, and G. A. Dulk, Cyclotron maser emission of auroral Z-mode radiation, J. Geophys. Res., in press, 1983.

Kaiser, M. L., and R. G. Stone, Earth as an intense planetary radio source: Similarities to Jupiter and Saturn, Science, 189, 285, 1975.

Kaiser, M. L., J. K. Alexander, A. C. Riddle, J. B. Pearce, and J. W. Warwick, Direct measurements of the polarization of terrestrial kilometric radiation from Voyagers 1 and 2, Geophys. Res. Lett., 5, 857, 1978.

Kaufman, R. L., P. B. Dusenbery, and B. J. Thomas, Stability of the auroral plasma: Parallel and perpendicular propagation of electrostatic waves, J. Geophys. Res., 83, 5663, 1978.

Kurth, W. S., M. M. Baumback, and D. A. Gurnett, Direction-finding measurements of auroral kilometric radiation, J. Geophys. Res., 80, 2764, 1975.

Lee, L. C., and C. S. Wu, Amplification of radiation near cyclotron frequency due to electron population inversion, Phys. Fluids, 23, 1348, 1980.

LeQueau, D., R. Pellat, and A. Roux, Direct generation of the auroral kilometric radiation by the maser synchrotron instability. An analytic approach, Phys. Fluids, in press, 1983.

Maggs, J. E., and W. Lotko, Amplification of electrostatic noise in cyclotron resonance with an adiabatic auroral beam, J. Geophys. Res., 86, 3449, 1981.

Melrose, D. B., K. G. Rönnmark, and R. G. Hewitt, Terrestrial kilometric radiation: The cyclotron theory, J. Geophys. Res., 87, 5140, 1982.

Melrose, D. B., R. G. Hewitt, and G. A. Dulk, Electron-cyclotron maser emission: Relative growth and damping rates for different modes and harmonics, J. Geophys. Res., submitted, 1983.

Mizera, P. F., and J. F. Fennell, Signatures of electric fields from high and low altitude particle distributions, Geophys. Res. Lett., 4, 311, 1977.

Omidi, N., and D. A. Gurnett, Growth rate calculations of auroral kilometric radiation using the relativistic resonance condition, J. Geophys. Res., 87, 2377, 1982.

Omidi, N. and D. A. Gurnett, Path integrated growth of auroral kilometric radiation, J. Geophys. Res., submitted, 1984.

Omidi, N., C. S. Wu, and D. A. Gurnett, Generation of auroral kilometric and Z-mode radiation by the cyclotron maser mechanism, J. Geophys. Res., 89, 883, 1984.

Ratcliffe, J. A., The Magneto-ionic Theory and Its Applications to the Ionosphere, Cambridge Univ. Press, Cambridge, 1959.

Shawhan, S. D., and D. A. Gurnett, The polarization of auroral kilometric radiation, Geophys. Res. Lett., 9, 913, 1982.

Stix, T. H., The Theory of Plasma Waves, McGraw-Hill, New York, 1962.

Taylor, W. W. L., and S. D. Shawhan, A test of incoherent Cerenkov radiation for VLF hiss and other magnetospheric emissions, J. Geophys. Res., 79, 105, 1974.

Wu, C. S., and L. C. Lee, A theory of the terrestrial kilometric radiation, Astrophys. J., 230, 621-626, 1979.

Wu, C. S., H. K. Wong, D. J. Gorney, and L. C. Lee, Generation of the auroral kilometric radiation, J. Geophys. Res., 87, 4476, 1982.